Universiteit
Leiden
The Netherlands

Flow : a study of electron transport through networks of interconnected nanoparticles

Blok, S.

Citation
Blok, S. (2018, July 4). *Flow : a study of electron transport through networks of interconnected nanoparticles*. *Casimir PhD Series*. Retrieved from https://hdl.handle.net/1887/63527

Version:	Not Applicable (or Unknown)
License:	Licence agreement concerning inclusion of doctoral thesis in the Institutional Repository of the University of Leiden
Downloaded from:	https://hdl.handle.net/1887/63527

Note: To cite this publication please use the final published version (if applicable).

Cover Page

Universiteit Leiden

The handle http://hdl.handle.net/1887/63527 holds various files of this Leiden University dissertation.

Author: Blok, S.
Title: Flow : a study of electron transport through networks of interconnected nanoparticles
Issue Date: 2018-07-04

Flow:
A study of electron transport through networks of interconnected nanoparticles

Proefschrift

ter verkrijging van
de graad van Doctor aan de Universiteit Leiden,
op gezag van Rector Magnificus prof.mr. C.J.J.M. Stolker,
volgens besluit van het College voor Promoties
te verdedigen op woensdag 4 juli
klokke 15:00 uur

door

Sander Blok

geboren te Groningen
in 1988

Promotores:	Prof.dr.ir. S.J. van der Molen Prof.dr. J.M. van Ruitenbeek
Promotiecommissie:	Dr. M. Blaauboer (Technische Universiteit Delft) Prof.dr. E.R. Eliel Prof.dr. K. Leifer (Uppsala Universitet, Zweden) Prof.dr.ir. S.J.T. van Noort Prof.dr.ir. T.H. Oosterkamp

Casimir PhD series, Delft-Leiden 2018-22
ISBN 978.90.8593.351.9
An electronic version of this thesis can be found at
`https://openaccess.leidenuniv.nl`.

The research done for this thesis was conducted at the Leiden Institute of Physics, Leiden University. This work was supported by the Netherlands Organisation for Scientific Research (NWO/OCW), as part of the Frontiers of Nanoscience program.

Typesetting was done by the author using XeLaTeX.

The cover shows an artist's impression of a network of nanoparticles (white) connected by molecular linkers (red). The teal line represents an electron travelling from left to right along the easiest percolating path.

Contents

1 Molecular electronics 1
- 1.1 A brief history of molecular electronics . . . 3
- 1.2 Charge transport at the nanoscale . . . 4
- 1.3 Contacting the molecules . . . 6
  - 1.3.1 Electron transmission through a molecule . . . 7
  - 1.3.2 Experimental methods . . . 10
  - 1.3.3 Gold nanoparticle networks . . . 12

2 Gold nanoparticle networks interconnected by molecular linkers 17
- 2.1 Molecular electronics as a basis for studying nanoparticle networks . . . 21
- 2.2 Optical properties . . . 22
- 2.3 High sensitivity quantum strain gauges . . . 25
  - 2.3.1 Mechanical properties . . . 25
  - 2.3.2 Strain sensors . . . 26
- 2.4 Electronic transport . . . 28
  - 2.4.1 Resistance after molecular exchange . . . 29
- 2.5 Coulomb blockade . . . 30
- 2.6 Beyond the blockade: Cotunneling . . . 31

3 Cotunneling with energy dependent contact transmission 41
- 3.1 Introduction . . . 45
- 3.2 Theory of cotunneling mechanisms . . . 46
- 3.3 Approach 1: Lorentzian transmission . . . 47
- 3.4 Approach 2: Multiple cotunneling . . . 53
- 3.5 Conclusion . . . 57

4 Experimental set-up and sample fabrication 61
- 4.1 Cryostat . . . 62
  - 4.1.1 Remote operation and automation . . . 64

4.1.2 Insert . . . 64
4.1.3 Chip carrier . . . 66
4.2 Measurement electronics . . . 67
4.2.1 Improving noise floor . . . 67
4.3 Sample fabrication . . . 71
4.3.1 Device fabrication . . . 71
4.3.2 Nanoparticle synthesis . . . 72

5 Studying electron transport through nanoparticle arrays 79
5.1 Introduction . . . 80
5.2 Theory of multiple cotunneling . . . 80
5.2.1 The Arrhenius model . . . 80
5.3 The alternative model . . . 82
5.3.1 Determining $\mathcal{N}$ . . . 82
5.3.2 Determining $\mathcal{P}$ . . . 84
5.3.3 The Full Equation . . . 85
5.4 Consequences of the new model . . . 86
5.5 Comparison to experimental data . . . 88
5.5.1 Disorder . . . 93
5.6 Cotunneling length . . . 100
5.6.1 Is there higher-order transport? . . . 101
5.7 Conclusion . . . 102

6 Nanoparticle network devices interlinked by molecular switches 107
6.1 Introduction . . . 108
6.1.1 Prediction of enhanced switching . . . 108
6.2 Molecular switches . . . 109
6.3 Device fabrication . . . 110
6.4 Optical measurements . . . 111
6.5 Initial results in dark environment . . . 115
6.6 Effect of light at constant temperature . . . 116
6.7 Conclusion . . . 120

7 LEEM-potentiometry on gold nanoparticle networks 123
7.1 Introduction . . . 124
7.2 Low-Energy Electron Microscopy . . . 124
7.2.1 Potentiometry . . . 127
7.3 Experimental methods . . . 128
7.3.1 Sample preparation . . . 128
7.3.2 Measurement technique . . . 129

7.4 Results and discussion . . . 130
7.5 Conclusion . . . 137

Appendices 141
A Theoretical background of approach 1 . . . 141
B Equivalence of multiple cotunneling model to second-order cotunneling . 143
C Pulse tube operation . . . 145
D Exploring the parameter space of the alternative model . . . 149
E Additional data for chapter 6 . . . 153
E.1 Additional fitting on 10 nm nanoparticle networks . . . 153
E.2 Full data set on slope versus voltage . . . 155
F Fits to the data after exchange with molecular switches . . . 157

English summary 159

Nederlandstalige samenvatting 163

Dankwoord 169

Curriculum Vitae 171

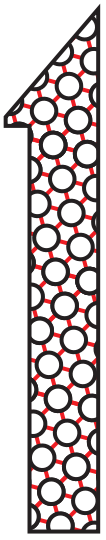

Molecular electronics

1.1 A BRIEF HISTORY OF MOLECULAR ELECTRONICS

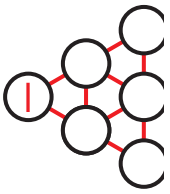

The field of molecular electronics is derived from the concept of using nature's smallest possible object as an electronic component. The first experimental paper in this field is usually credited to Kuhn *et al.*, who measured the current through fatty acid monolayers[1]. The field itself however, was heralded three years later in 1974 by Aviram and Ratner[2], who discussed transport through a single molecule. Their article suggested that a molecule could act as a rectifier, supported by *ad hoc* calculations. Although stating that solutions to predicted problems, such as contacting the molecule, were underway, it would take until the 1980s for the first tool to probe individual molecules to be developed.

With the creation of the scanning tunneling microscope (STM), it became feasible to experimentally investigate electronic properties of single molecules. In 1995, the first conductance measurement of a single molecule was done by Joachim *et al.*[3], who used a STM to measure the electrical current through a single Buckminsterfullerene molecule. Interestingly, they found that deforming the molecule by pressing it with the STM tip changed the conductance properties. This was followed up shortly afterwards by Reed *et al.*[4], who measured the conductance of benzene dithiol in between the electrodes of a mechanically controlled break junction (MCBJ), as developed by van Ruitenbeek *et al.*[5] (see below). These two initial articles generated a large hype in the field and together with articles such as the reviews published in 2000[6] or the Science Breakthrough of 2001[7] marked the true beginning of the field.

The original dream of molecular electronics was to replace silicon-based technology, as even now, state of the art transistors have a gate width of 50 nm, almost two orders of magnitude larger than single molecules*. However, with single molecule junctions being notoriously unstable and the current technology heavily invested in the top-down approach of silicon, it is unlikely to be replaced any time soon. Molecules, on the other hand, can also do much more than just boolean logic and can therefore be an extension to silicon-based technology, rather than a complete replacement.

With the extensive library of molecules that organic chemistry provides, the amount of different molecules that can be built is virtually endless. Additionally, even small changes to a molecule, such as changing the bond geometry of a central phenyl ring from para to meta can lead to large changes in its properties[8]. In the para configuration, the two electron paths travelling through either side of the phenyl ring have the same path length and interfere constructively. In the meta configuration, these two paths have a different length, and interfere destructively. This quantum interference effect can result in a conductance in that is almost two orders of magnitude lower[9].

Interestingly, the destructive interferences lead to sharp variations in the so-called transmission function, which in turn, can lead to large thermoelectric effects[10,11]. This means that molecules can be used to transform a temperature difference into electrical power, as

*To paraphrase Richard Feynman: There indeed still is plenty of room at the bottom!

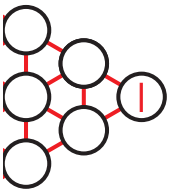

shown by Reddy *et al.*[12]. Inspired by earlier experiments by van Ruitenbeek *et al.*[13], they measured the thermopower of oligophenyl chains, showing an increase in thermopower with increasing molecule length.

As small changes to a molecule can radically change its electrical properties, molecules that can switch between two states by external stimulus can act as sensors for these external stimuli. Recently, Atesci *et al.*[14] demonstrated that self-assembled monolayers or SAMs of ruthenium-based molecules showed very large rectification ratios of over 8000 under ambient conditions. Under dry nitrogen, however the rectification disappeared almost completely, to reappear again when water vapor was introduced into the nitrogen atmosphere, indicating a large sensitivity to water.

Other sensitive molecules include diarylethylenes, molecules that switch from a conjugated closed state to a non-conjugated open state upon illumination with light. This switching was first attempted by Dulíc *et al.*[15] using a MCBJ. A sharp conductance decreased was observed upon optical illumination, indicating switching of the molecule. Switching back, however, proved to not be possible. This illustrates the high sensitivity of molecules to their surroundings. Molecules may behave ideally in solution, but lose their functionality once chemically bound to the contacts of a break junction. It would take five years before back-conversion was possible, using molecules with slightly different anchoring groups to decouple the functional backbone from the contacts[16]. In contrast to previous experiments, these new experiments were not done using a MCBJ, but a network of gold nanoparticles, allowing optical probing in addition to the electrical measurements. The observed change in resistance upon switching, however, was much lower (20%) than using a MCBJ, giving rise to the question of how to increase this ON-OFF ratio.

Molecular electronics is an interesting field, not only due to the applications, but also because it gives a platform to study small-scale physics in a semi-tabletop environment. After its conception in 1974, and the initial hype that followed the first experiments in 2000, the field has now reached maturity, and applications are already commercially available[17]. The inherent quantum nature of molecules due to the small scales involved are interesting in itself, but also provide insight into the relation between form and function on the nanoscale. The next sections will discuss the theory of charge transport on these small scales and the experimental techniques used to probe them.

1.2 CHARGE TRANSPORT AT THE NANOSCALE

At the macroscopic scale, charge transport behaves as follows: a current I flows through a resistor with conductance G due to an applied voltage V (this is described by Ohm's law: $I = GV$). Energy is dissipated in the resistor due to inelastic scatting of the electrons with the atoms in the resistor. At the nanoscale, this is no longer the case. For example: electrons flowing through a single gold atom do not necessarily dissipate energy into the atom itself. In this case, it is more accurate to describe the situation as a wave passing through a potential

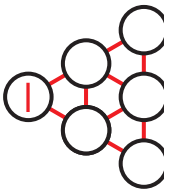

landscape instead.

To see how electrons flow through such a system, consider a thin conducting wire. If the wire is sufficiently thin, the electron wavelength becomes comparable to the thickness of the wire causing it to be confined in the x and y dimensions, but not in the z dimension, defined as along the wire. The electron density of states is then given by[18]:

$$\rho(E) = \frac{1}{\pi\hbar}\sqrt{\frac{m_\mathrm{e}}{2E}}, \tag{1.1}$$

where m_e is the electron mass, E is its energy and $\hbar$ is the reduced Plank's constant. To obtain the electron current, we have to multiply the number of flowing electrons by their velocity v, given by $v(E) = \sqrt{2E/m_\mathrm{e}}$, and integrate over all energies. The net number of flowing electrons is given by the number of electrons flowing from left to right $f_\mathrm{L}(E)$ minus the ones flowing from right to left $f_\mathrm{R}(E)$[†] times the density of states. Here $f_{\mathrm{L,R}}(E)$ is the Fermi-Dirac distribution[19,20] given by:

$$f_{\mathrm{L,R}}(E) \equiv \frac{1}{1+\exp\left(\frac{E-\mu_{\mathrm{L,R}}}{k_\mathrm{B}T}\right)}. \tag{1.2}$$

The electrochemical potentials of the left and the right lead are $\mu_{\mathrm{L,R}}$ respectively. If a bias of V is applied over the wire, the electrochemical potentials shift such that $\mu_\mathrm{L} - \mu_\mathrm{R} = eV$. The net current can then be written as:

$$I = e\int_{-\infty}^{\infty} v(E)\rho(E)\left[f_\mathrm{L}(E) - f_\mathrm{R}(E)\right]\mathrm{d}E = \frac{2e^2}{h}V. \tag{1.3}$$

The factor two comes from summing over the two degenerate spin channels. The constant $2e^2/h$ is usually called the conductance quantum G_0, the conductance of one fully transparent transport channel. Interestingly, the conductance does not depend on the length of the wire, in contrast to at the macroscopic scale, where the conductance scales inversely proportional to length. When two of such nanowires are put in series, the conductance remains the same. Furthermore, no energy is dissipated in the wire itself, but rather in the leads connecting to the wire.

If the width of the wire is increased slowly so that additional lateral modes fit inside of it, the conductance increases incrementally with steps of G_0. This has been first observed experimentally by Bart van Wees *et al.* in 1988[21] in a two-dimensional electron gas at cryogenic temperatures using electrostatic gates to pinch off the conductance channel. The

[†] This describes all electrons in the left lead attempting to flow to the right, and vice versa, without taking into account the availability of electron states on the other side. A more correct way is actually taking into account the probability of finding an unoccupied state on the other side, resulting in: $f_\mathrm{L}(1-f_\mathrm{R}) - f_\mathrm{R}(1-f_\mathrm{L})$. Usually, these expressions are identical, but there are times where they are not, as discussed in Chapter 5.

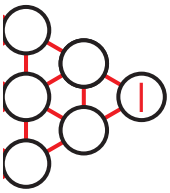

same effect can also be observed at room temperature in metal wires being pulled apart to create atomic point-contacts[13].

The situation from Eq. 1.3 is valid for perfectly transparent systems, and can be generalized for conductors with non-unitary transmission probabilities $\mathcal{T}$. This is called the Landauer[22] formula:

$$G = G_0 \sum_i \mathcal{T}_i. \tag{1.4}$$

This means that the apparent conductance is given by the sum over the transmission probabilities of all channels. In practice, the sum is usually omitted, and all separate transmission channels are combined in one transmission function ($\mathcal{T} \equiv \sum_i \mathcal{T}_i$). Usually, the transmission probability of the electron is not constant but depends on its energy. In this case, Eq. 1.4 is expanded to encompass this dependence:

$$I = G_0 \int_{-\infty}^{\infty} \mathcal{T}(E)(f_{\mathrm{L}}(E) - f_{\mathrm{R}}(E))\mathrm{d}E. \tag{1.5}$$

It can be seen that if the transmission function is not a constant, the current versus voltage characteristics are nonlinear. This can result in interesting behavior for molecules in electronics, as discussed in the following sections. At low temperatures where $k_{\mathrm{B}}T$ is much smaller than the variation in $\mathcal{T}$ and the electrostatic energy eV, the Fermi functions inside the integral approach step-functions. In this case the current can be approximated by omitting the Fermi functions and integrating the transmission function from 0 to eV. When $\mathcal{T}$ does not change significantly on the scale of eV, it can be approximated by a constant, and Eq. 1.5 reduces to Ohm's law.

Although this lays the foundation for electron transport at the nanoscale, we haven't yet discussed transport through molecules themselves, or the shape of their transmission function. This subject will be explained in the next section.

1.3 CONTACTING THE MOLECULES

In order to study micro- (or nano-) scopic single molecules, they need to be connected electrically to our macroscopic multimeter. Not only is this a challenging experimental problem, connecting the molecule often changes its properties. Molecular switches for example can lose their ability to switch, as discussed in Chapter 6. Furthermore, the electrical connection can shift the energy levels present in the molecule and seemingly broadens them. This apparent broadening can be explained in an intuitive way, analogous to the apparent broadening of a mode in a Fabry-Pérot interferometer.

1.3.1 ELECTRON TRANSMISSION THROUGH A MOLECULE

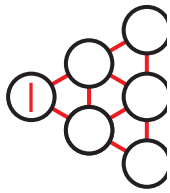

A Fabry-Pérot interferometer consists of two semi-transparent mirrors with a certain distance x between them, forming a cavity. When a monochromatic light ray with wavelength λ is incident on this interferometer, it has a certain chance to be transmitted through the first mirror into the cavity. Once inside, it hits the second mirror, having a certain chance to be transmitted by the second mirror out of the cavity (let's call these left and right transmission probabilities $\mathcal{T}_\mathrm{L}$ and $\mathcal{T}_\mathrm{R}$ respectively). Inside the cavity, the light bounces back and forth, interfering with itself, upon each reflection losing amplitude by transmission through the barrier. This self-interference causes the transmission through the cavity to depend on its length. The lower the transmission probabilities of the mirror, the longer the lifetime of the light inside the cavity, allowing it to interfere with itself more. The probability to transmit through the interferometer is given by:

$$\mathcal{T}_\text{Fabry-Pérot} = \frac{\mathcal{T}_\mathrm{L}\mathcal{T}_\mathrm{R}}{1 + \mathcal{R}_\mathrm{L}\mathcal{R}_\mathrm{R} - 2\sqrt{\mathcal{R}_\mathrm{L}\mathcal{R}_\mathrm{R}}\cos\left(\frac{4\pi x}{\lambda}\right)}, \tag{1.6}$$

where $\mathcal{R}_\mathrm{L,R} = 1 - \mathcal{T}_\mathrm{L,R}$. This is a function periodic in λ, which makes sense as not only the case where $2\lambda = x$ interferes constructively, also higher resonance modes where $2n\lambda = x$ do so. This function is called a wrapped Cauchy distribution; a sum over Lorentzians, each individual Lorentzian corresponding to one resonance mode.

Now consider a single molecule connected electrically to electrodes on both sides. These connections act as barriers to the environment with a certain transmission probability, much like the mirrors in the Fabry-Pérot interferometer. For a molecule with only one energy level at $E = \epsilon_0$, all other levels in Eq. 1.6 can be ignored, allowing the cosine to be Taylor-expanded around zero. Moreover, the electron energy can be written as a function of the De Broglie wavelength. Using this, Eq. 1.6 can be rewritten to yield:

$$\mathcal{T}_\mathrm{M}(E) = \frac{4\Gamma_\mathrm{L}\Gamma_\mathrm{R}}{(E - \epsilon_0)^2 + (\Gamma_\mathrm{R} + \Gamma_\mathrm{L})^2}. \tag{1.7}$$

The transmission probabilities are substituted by the molecule/contact coupling Γ, where $\Gamma_\mathrm{L,R} = \frac{\mathrm{d}E}{\mathrm{d}\theta}\mathcal{T}_\mathrm{L,R}$ and $\theta = 4\pi x\lambda^{-1}$. Using a more rigorous approach using non-equilibrium Green's function theory yields the same result. This means that although the molecular level is a delta-function at a well defined energy, the coupling to the environment causes the level to appear broadened. The total transmission through a molecule with multiple levels is then a sum over all individual levels, each with their own coupling and resonance energy[‡].

[‡] This is very similar to a Fabry-Pérot interferometer with a cavity filled by a medium with an index of refraction dependent on wavelength $n(\lambda)$ and mirror reflections that also depend on the wavelength ($\mathcal{T}(\lambda)$). Or in other words, any real interferometer.

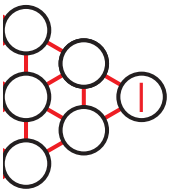

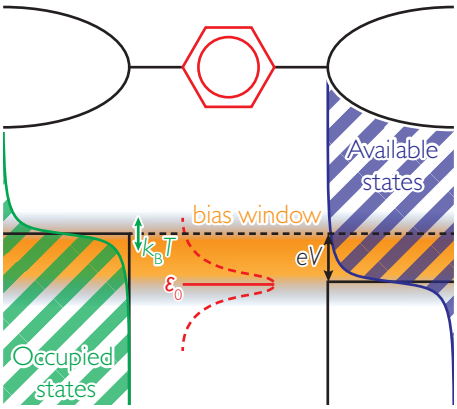

Fig. 1.1: A schematic of a molecule connected by two leads above the energy diagram. Applying a bias across the electrodes opens up a bias window shown in orange, broadened by temperature. Electrons can flow from the occupied states on the left through the molecule into unoccupied states on the right. The molecular level has a resonance energy of ϵ_0, and the transmission is broadened due to coupling to the leads. It can be intuitively understood from this figure why the current saturates at high applied bias. Applying an even larger bias to the left lead does not significantly increase the current, as the transmission at these energies is low.

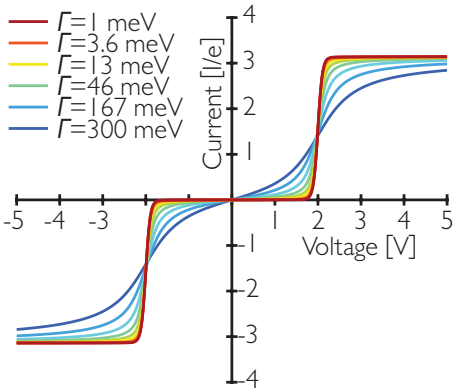

Fig. 1.2: Calculated normalized current versus voltage curve for a Lorentzian transmission function with varying Γ, the temperature is 300 K and $\epsilon_0 = 1$ eV. The current is calculated by computationally solving Eq. 1.5 using the transmission function from Eq. 1.7, assuming that $\Gamma_R = \Gamma_L = \Gamma$. Gamma is varied logarithmically from 1 meV to 300 meV, represented by the different line colors, some of which are shown in the legend. The currents are normalized by dividing each individual curve by Γ. It can be seen that increasing Γ broadens the transmission function and hence smoothens out the IV-curve. The current at large voltages is equal for each curve, as the transmission function is fully saturated.

Using this transmission function, we can now solve Eq. 1.5 for a molecule connected by two leads, as shown in Fig. 1.1. This figure shows a benzene molecule modelled as a single level connected by leads, causing a broadened transmission function. Applying a bias across the leads opens up a bias window, which is broadened by temperature. Assuming that the temperature is low, the function can be approximated by integrating Eq. 1.7 from $-1/2V$ to $+1/2V$ (assuming the voltage drops symmetrically across the molecule). If $\Gamma_L = \Gamma_R$, the

result is given by:

$$I = \frac{G_0 \Gamma}{e}\left[\arctan\left(\frac{+1/2eV - \epsilon_0}{\Gamma}\right) - \arctan\left(\frac{-1/2eV - \epsilon_0}{\Gamma}\right)\right]. \qquad (1.8)$$

This means that at high positive or negative voltage $eV \gg \epsilon_0$ or $eV \ll -\epsilon_0$, the current saturates at a value $G_0\Gamma/e$. This happens because the entire channel is saturated, and any other available electrons have energies so far from the resonance that they do not contribute to the current. For nonzero temperatures, the current can be calculated computationally. This is done in Fig. 1.2, where the current is calculated between two leads interconnected by a single level for several molecule/contact couplings.

From the figure it can be seen that there is almost no current at low voltages, until the voltage reaches a threshold of $2\epsilon_0$ where it sharply increases to a saturation value. As Γ increases, the current transitions more smoothly. The currents in the graph are normalized by dividing each current by Γ, since the saturation current increases with increasing coupling.

Although the single level model is a good approximation, real molecules have more complex transmission functions that also depend on the contacting method. They are usually calculated using self consistent computational models such as Density Functional Theory (DFT) or Hartree-Fock (HF). An example of such a transmission function can be seen in Fig 1.3.

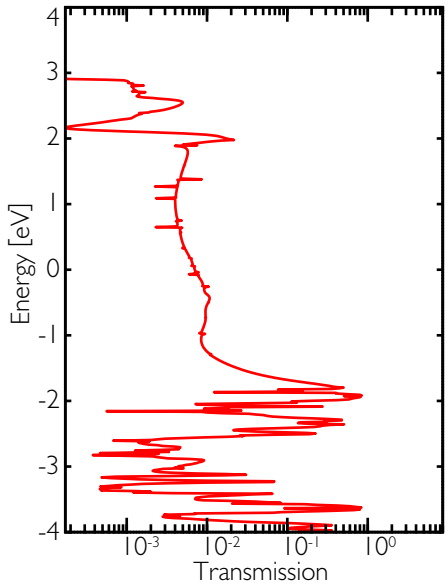

Fig. 1.3: Calculated transmission function of a molecular junction using density functional theory and non-equilibrium Green's functions. Contrary to a single level approximation, a fully calculated transmission function has many maxima and minima, due to constructive and destructive electron interference within the molecule. This particular transmission function is calculated for a benzenediamine molecule chemically connected to two metal contacts. Adapted from Celis Gil *et al.*[23]

Summarizing: molecules as electronic components are interesting not only because of their possible applications, but also due to their fundamentally fascinating properties. Due

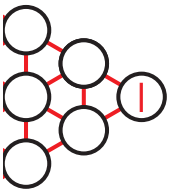

to their small size, molecules show pronounced quantum behavior at room temperature and also allow tuning of their properties, made possible by the large library of organic chemistry. This leaves one problem, however: how can molecules be contacted to our measurement equipment?

1.3.2 Experimental methods

Molecules are small, and therefore do not allow easy access to their properties. Even the recent advances in lithography only allow a resolution down to 7 nm, insufficient for molecules almost an order of magnitude smaller. Contacting the molecules has been a major problem for the field of molecular electronics since its conception. Nowadays, however, a wide range of experimental methods exist to study individual molecules or ensembles of them.

The proverbial work-horse of contacting methods is the mechanically controlled break-junction or MCBJ[24]. A MCBJ (see Fig. 1.4) uses a bendable substrate to pull apart a notched metallic wire or lithographically confined constriction, controllably breaking it. Since the strain is induced by a push rod on the bottom, the actual strain on the wire is only a fraction of the pushed distance of the rod. This allows control of the electrode separation with sub-namometer precision.

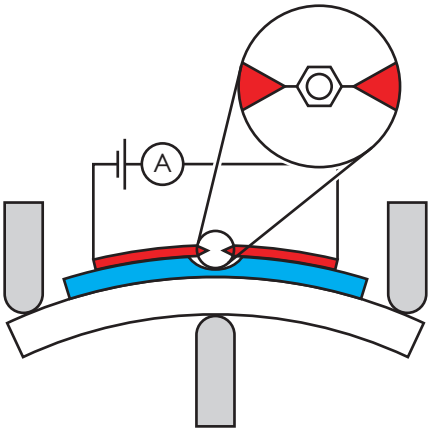

Fig. 1.4: Schematic depiction of a mechanically controlled break junction. Two contacts (red) are lithographically fabricated on a bendable substrate, protected by a spacer layer (blue). By pushing against the middle of the substrate while holding the edges, the substrate is bent, separating the red contacts with sub-nanometer precision. When the separation is just right, a molecule exactly fits in between the contacts and IV-traces can be measured.

The MCBJ is commonly used to measure conductance-versus-distance curves. A fixed voltage is set on the electrodes, and the conductance is measured as a function of inter-electrode separation. The junction is then repeatedly formed and broken. When molecules are introduced into the system (either in solution or evaporated in a vacuum), each cycle creates a new junction, as the molecule can bind to the contacts in different orientation. This is repeated in the order of 1000 to 10 000 times, creating a large dataset. When this dataset is represented as a histogram (seen in Fig. 1.5), the signature of the molecule shows up as a peak in the histogram around the conductance of the molecule. Moreover, the current as a function of voltage can be measured at each distance, allowing for the probing of the single

molecule IV-characteristics[24,25]. This is a tedious task, however, as there are many different junction orientations, all having slightly different transmission functions (if a molecule is present at all!).

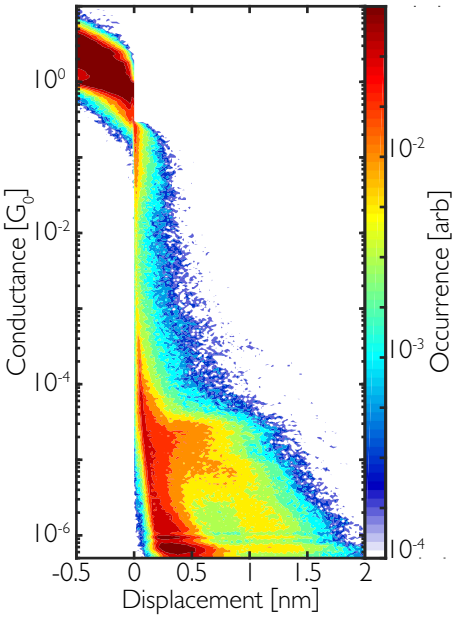

Fig. 1.5: Histogram displaying conductance traces (conductance versus junction separation) measured of diazofluorene functionalized buckminsterfullerene, color shows frequency of occurrence. The measurements are done using a MCBJ in air. From the figure it can be seen that a sharp drop in conductance is observed when the junction is broken. However, peaks in the conductance are observed around 2×10^{-5} G_0, 7×10^{-6} G_0 and 2×10^{-6} G_0, indicating the presence of the molecule. If the molecule was not present, only a sharp drop in conductance would be observed. Adapted from Stefani *et al.*[26].

A similar approach uses a STM to create a break junction (STM-BJ). The STM-BJ is different from the MCBJ, as the STM-BJ starts separated in contrast to the MCBJ, which starts connected. Pushing the STM tip into the substrate creates a junction that can be broken and reformed at will[27].

Whereas break junction experiments allow for single-molecule measurements, other approaches use many junctions in parallel. One of these approaches is contact-probe atomic force microscopy (CP-AFM) on SAMs[14]. In this technique, an ordered self assembled monolayer is created on top of a substrate, and characterized using a conducting AFM tip. Data from single molecules cannot be obtained in this way, as the AFM tip contacts many molecules simultaneously and hence measures a statistical average. Furthermore, SAMs are very stable and can be measured in ambient conditions for days. CP-AFM on SAMs is ideal for measuring functional molecules, such as switchable rectifiers[14], as the stability allows repeated measurement, even in high humidity and elevated temperatures.

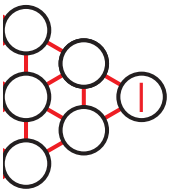

1.3.3 GOLD NANOPARTICLE NETWORKS

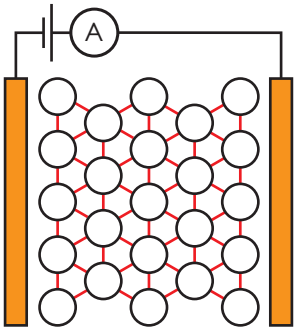

Fig. 1.6: Schematic depiction of a nanoparticle network. The nanoparticles are linked by the molecules shown as the red lines and are connected by the electrodes shown in orange.

In the same vein as CP-AFM on SAMs, statistical averages of molecules can also be investigated by using networks of nanoparticles interconnected by molecular linkers[28] (see Fig. 1.6). Networks of gold nanoparticles are easy to create using self assembly, and are stable under ambient conditions. Once interlinked by molecules, their conductance at room temperature are an average of the conductance of the interlinking molecules. Interestingly, these electrical measurements can be expanded by optical techniques, as the absorption spectra of the network strongly depends on the interlinking molecule, as we shall see in chapter 6. In this way, molecular functionality such as optical switching can be observed not only by electrical measurements, but also by optical investigation[16]. Moreover, at cryogenic temperatures, the network exhibits Coulomb blockade and electron transport is mediated by (multiple) cotunneling.

Cotunneling is a form of electron transport that is mediated by quantum fluctuations of charge, involving intermediate virtual electron states, yielding a distinct IV-characteristics. In the Coulomb blockade regime, transport through a network linked by molecules is non-trivial, and cotunneling through nanoparticles connected by molecules on both sides will be discussed in chapter 3. Moreover, cotunneling enhances the signature of the interlinking molecule[29], an intriguing property we tried to utilize to enhance the ON-OFF ratio of molecular switches, discussed in chapter 6. The current theory of multiple cotunneling by Tran *et al.*[30] predicts that Coulomb blockaded nanoparticle networks show varying cotunneling length, depending on the temperature and applied bias. In chapter 5 we provide an alternative approach, predicting that the electrical properties are different than previously thought.

The electrical properties of the nanoparticle network do not only depend on the interlinking molecules, but also on the structure of the network itself. The networks are ordered on the scale of a few nanoparticles, but can have cracks and holes in them on the larger scales. We investigate how these imperfections affect the electrical properties in chapter 7.

Networks of nanoparticles provide a viable platform for functional molecular electronics, and inversely, functional molecules provide a method for studying the properties of the networks themselves. Nanoparticle networks interconnected by molecules not only have potential applications, but also show very interesting fundamental properties. This thesis focuses on the transport properties of nanoparticle networks, especially at cryogenic temperatures. The next chapter provides an introduction to this field.

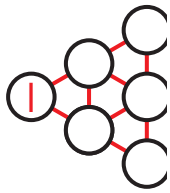

References

[1] Bernhard Mann and Hans Kuhn. Tunneling through Fatty Acid Salt Monolayers. *Journal of Applied Physics*, 42(11):4398–4405, 1971.

[2] Arieh Aviram and Mark A. Ratner. Molecular rectifiers. *Chemical Physics Letters*, 29 (2):277–283, 1974.

[3] Christian Joachim, James K. Gimzewski, Reto R. Schlittler, and Corinne Chavy. Electronic transparence of a single C 60 molecule. *Physical Review Letters*, 74(11):2102, 1995.

[4] Mark A. Reed, C. Zhou, C. J. Muller, T. P. Burgin, and J. M. Tour. Conductance of a molecular junction. *Science*, 278(5336):252–254, 1997.

[5] C.J. Muller, J.M. van Ruitenbeek, and L.J. de Jongh. Experimental observation of the transition from weak link to tunnel junction. *Physica C: Superconductivity*, 191(3): 485 – 504, 1992.

[6] Christian Joachim, J. K. Gimzewski, and A. Aviram. Electronics using hybrid-molecular and mono-molecular devices. *Nature*, 408(6812):541–548, 2000.

[7] Robert F. Service. Molecules Get Wired. *Science*, 2001.

[8] Gemma C. Solomon, Carmen Herrmann, Thorsten Hansen, Vladimiro Mujica, and Mark A. Ratner. Exploring local currents in molecular junctions. *Nature Chemistry*, 2(3):223–228, 2010.

[9] Carlos R. Arroyo, Simge Tarkuc, Riccardo Frisenda, Johannes S. Seldenthuis, Charlotte H. M. Woerde, Rienk Eelkema, Ferdinand C. Grozema, and Herre S. J. van der Zant. Signatures of Quantum Interference Effects on Charge Transport Through a Single Benzene Ring. *Angewandte Chemie International Edition*, 52(11):3152–3155, 2013.

[10] Neil B. Ashcroft and N. David Mermin. *Solid State Physics*. Holt, Rinehart and Winston, 1976.

[11] Yonatan Dubi and Massimiliano Di Ventra. Colloquium : Heat flow and thermoelectricity in atomic and molecular junctions. *Reviews of Modern Physics*, 83(1):131–155, 2011.

[12] Pramod Reddy, Sung-Yeon Jang, Rachel A. Segalman, and Arun Majumdar. Thermoelectricity in Molecular Junctions. *Science*, 315, 2007.

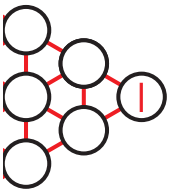

[13] B. Ludoph and J. M. Van Ruitenbeek. Thermopower of atomic-size metallic contacts. *Physical Review B*, 59(19):12290, 1999.

[14] Hüseyin Atesci, Veerabhadrarao Kaliginedi, Jose A. Celis Gil, Hiroaki Ozawa, Joseph M. Thijssen, Peter Broekmann, Masa-aki Haga, and Sense Jan van der Molen. Humidity-controlled rectification switching in ruthenium-complex molecular junctions. *Nature Nanotechnology*, 13(2):117–121, 2018.

[15] Diana Dulić, S. J. van der Molen, T. Kudernac, H. T. Jonkman, J. J. D. de Jong, T. N. Bowden, J. van Esch, B. L. Feringa, and B. J. van Wees. One-Way Optoelectronic Switching of Photochromic Molecules on Gold. *Physical Review Letters*, 91(20), 2003.

[16] Sense Jan van der Molen, Jianhui Liao, Tibor Kudernac, Jon S. Agustsson, Laetitia Bernard, Michel Calame, Bart J. van Wees, Ben L. Feringa, and Christian Schönenberger. Light-Controlled Conductance Switching of Ordered Metal−Molecule−Metal Devices. *Nano Letters*, 9(1):76–80, 2009.

[17] Dr. Scientist. The heisenberg molecular overdrive, 2014. drscientist.ca.

[18] Charles Kittel. *Introduction to Solid State Physics, 8th Edition*. Wiley, 2005.

[19] Enrico Fermi. Sulla quantizzazione del gas perfetto monoatomico. *Rendiconti Lincei*, 3, 1926.

[20] Paul A.M. Dirac. On the theory of quantum mechanics. *Proceedings of the Royal Society A*, 1926.

[21] B. J. Van Wees, H. Van Houten, C. W. J. Beenakker, J. Gr Williamson, L. P. Kouwenhoven, D. Van der Marel, and C. T. Foxon. Quantized conductance of point contacts in a two-dimensional electron gas. *Physical Review Letters*, 60(9):848, 1988.

[22] Rolf Landauer. Spatial variation of currents and fields due to localized scatterers in metallic conduction. *IBM Journal of Research and Development*, 1(3):223–231, 1957.

[23] J. A. Celis Gil and J. M. Thijssen. Transport gap renormalization at a metal-molecule interface using dft-negf and spin unrestricted calculations. *The Journal of Chemical Physics*, 147(8):084102, 2017.

[24] N. Agraït, A.L. Yeyati, and J.M. van Ruitenbeek. Quantum properties of atomic-sized conductors. *Physics Reports*, 377(2-3):81–279, 2003.

[25] Christian A Martin, Dapeng Ding, Herre S.J. van der Zant, and Jan M. van Ruitenbeek. Lithographic mechanical break junctions for single-molecule measurements in vacuum: possibilities and limitations. *New Journal of Physics*, 10, 2008.

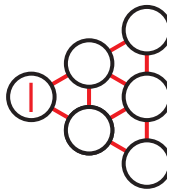

[26] Davide Stefani, Cristian A. Gutiérrez-Cerón, Daniel Aravena, Jacqueline Labra-Muñoz, Catalina Suarez, Shuming Liu, Monica Soler, Luis Echegoyen, Herre S.J. van der Zant, and Diana Dulić. Charge transport through a single molecule of trans-1-bis-diazofluorene [60]fullerene. *Chemistry of Materials*, 29(17):7305–7312, 2017.

[27] Xiao, Xu, and Nongjian J. Tao. Measurement of Single Molecule Conductance: Benzenedithiol and Benzenedimethanethiol. *Nano Letters*, 4(2):267–271, 2004.

[28] Jianhui Liao, Sander Blok, Sense Jan van der Molen, Sandra Diefenbach, Alexander W. Holleitner, Christian Schönenberger, Anton Vladyka, and Michel Calame. Ordered nanoparticle arrays interconnected by molecular linkers: electronic and optoelectronic properties. *Chemical Society Reviews*, 44:999–1014, 2015.

[29] Jean-Francois Dayen, Edwin Devid, Mutta Venkata Kamalakar, Dmitry Golubev, Constant Guédon, Vina Faramarzi, Bernard Doudin, and Sense Jan van der Molen. Enhancing the Molecular Signature in Molecule-Nanoparticle Networks Via Inelastic Cotunneling. *Advanced Materials*, 25(3):400–404, 2013.

[30] T. Tran, I. Beloborodov, X. Lin, T. Bigioni, V. Vinokur, and H. Jaeger. Multiple cotunneling in large quantum dot arrays. *Physical Review Letters*, 95(7), 2005.

GOLD NANOPARTICLE NETWORKS INTERCONNECTED BY MOLECULAR LINKERS

Parts of this chapter are based on the review:*

Ordered nanoparticle arrays interconnected by molecular linkers: electronic and optoelectronic properties

J. Liao, S. Blok, S.J. van der Molen, S. Diefenback, A.W. Holleitner, C. Schönenberger, A. Vladyka, M. Calame

Chemical Society Reviews 2015

* Only my own contributions to the review are used for this thesis, unless otherwise stated.

2.1 Molecular electronics as a basis for studying nanoparticle networks

Ordered arrays of nanoparticles interconnected by molecular linkers were introduced in the last chapter as a platform for molecular electronics. At room temperature, the nanoparticles act as electrodes, contacting many molecules simultaneously in parallel. As we saw in the last chapter, the presence of macroscopic amounts of interconnecting molecules allows for optical probing methods in addition to electrical measurements[1]. Enhancing the sensitivity of the network to the interlinking molecules found by Dayen *et al.*[2] suggested that nanoparticle networks are interesting by themselves. This means that molecular electronics can also be a basis for studying the properties of nanoparticle networks, rather than the other way around.

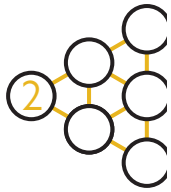

This means that the interconnected network can have two roles, a platform for studying the interconnecting molecules, or for studying the network itself. The external conditions such as temperature and applied bias determine which component is more important for the properties of the ensemble. This thesis will focus on the study of electron transport through the network, using the interconnecting molecules as a variable parameter. Additionally, nanoparticle arrays can also be used as highly sensitive strain sensors[3,4] or chemiresistors[5]. In this chapter, we will briefly review the general properties of nanoparticle networks and show the state-of-the-art research being done in this field.

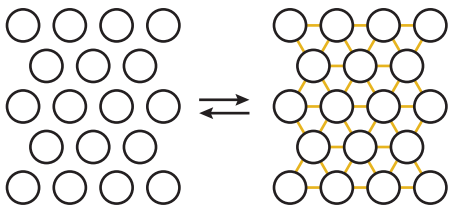

Fig. 2.1: Schematic depiction of molecular place exchange. The nanoparticle array is put in a solution of the molecule of interest (yellow lines) which inserts itself into the array. This process is reversible.

Nanoparticle arrays have a simple bottom-up fabrication process. The nanoparticles that make up the network can be synthesized by chemical reduction of chlorauric acid, yielding precise control over the size of the nanoparticles[6]. The nanoparticles are then capped by alkanethiols in order to prepare them for self-assembly, the latter of which is done either on a convex water-air interface[7], or by evaporation of a nanoparticle solution on a substrate[8]. After the array is transferred to the substrate, it can be interconnected by molecular linkers using molecular place-exchange as depicted schematically in Fig. 2.1. The full process is discussed in more detail in chapter 4.

Once interconnected, the nanoparticles act as individual electrodes, and the resistance of the network depends linearly on the resistance of the bridging molecule. To see why, consider the situation depicted in Fig. 2.2. A network of nanoparticles with particle to particle distance d is interconnected by molecules modeled as resistors with resistance R. When a potential V is applied across the dashed box from left to right, the current flows in

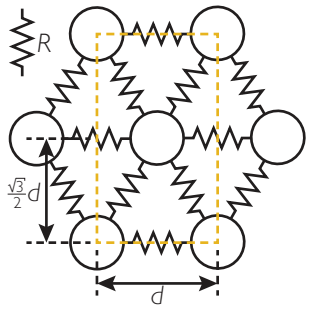

Fig. 2.2: Schematic depiction of a nanoparticle network interconnected by molecular bridges modeled as resistances with resistance R. The center to center distance of the nanoparticles is d. The repeating unit is indicated by the dashed red box. The four paths contributing to the current are through the top resistor, through the bottom resistor, through the center resistors from the leftmost nanoparticle via the center particle to the rightmost one and two identical paths from the top left through the center to the top right and from the bottom left through the center to the bottom right nanoparticle.

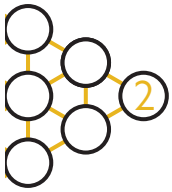

five parallel paths: through the top resistor, through the bottom resistor from the leftmost nanoparticle through the center nanoparticle to the rightmost one, and two paths via the center nanoparticle crossing two resistors in series. The current can then be written as: $I = {}^{4V}/_{R}$. However, as a repeating unit, the top and bottom currents are counted twice, adding an additional factor of ${}^{V}/_{R}$. Correcting for the geometry of the network and subtracting this additional factor gives a sheet resistance of:

$$R_{\square} = \sqrt{3}\frac{1}{4-1}R = \frac{1}{\sqrt{3}}R \approx 0.58R. \tag{2.1}$$

This means that in a perfectly ordered network, the sheet resistance can be directly related to the conductance of the connecting molecule, which is the prime reason that nanoparticle networks can be used to study molecular electronics. Interestingly, changing the molecular bridges through exchange does not only change the electrical resistance, it also changes the optical properties of the network. This allows for an independent optical measurement to see if the exchanged molecule is present. To see how exchange changes the optical properties, we first consider what determines the optical properties in the first place.

2.2 Optical properties

Since individual nanoparticles are small, their optical properties differ from those of the bulk material. A solution of 10 nm gold nanoparticles for example is ruby red (depending on the size) due to their surface plasmon resonance. A surface plasmon is a collective electron oscillation at the surface of a material. Fig. 2.3 shows schematic depiction of the surface plasmon resonance in nanoparticles interacting with an electromagnetic wave. Since the oscillation extends beyond the nanoparticles themselves, it is sensitive to its surroundings. For 10 nm gold nanoparticles in water, the resonance of this oscillation lies around an optical frequency corresponding to a wavelength of 513 nm[9]. However, in an array of these nanoparticles, the individual surface plasmons couple to their surroundings, changing their frequency and thereby the absorption wavelength.

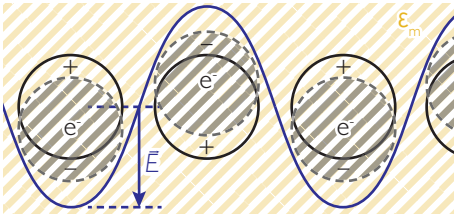

Fig. 2.3: Schematic depiction of nanoparticles in an oscillating electric field with amplitude $\vec{E}$ surrounded by an effective medium with permittivity ϵ_m. The electrons oscillate collectively as a response to the field. In reality, the nanoparticles are much smaller than the wavelength of the electric field.

A quantitative analysis of this behavior can be done using Mie theory[10], which describes the Maxwell equations for electromagnetic waves interacting with small metallic particles. Importantly, the particles are much smaller than the wavelength of the light, which means that the electric field does not change significantly across one nanoparticle. In this case, an absorption maximum occurs when the resonance condition is met:

$$\epsilon_1(\lambda_\mathrm{res}) = -2\epsilon_\mathrm{m}. \tag{2.2}$$

This condition states that a resonance occurs at the wavelength λ_res where the real part of the dielectric constant of the nanoparticle (ϵ_1) equals minus twice that of the medium (ϵ_m). When nanoparticles are in a network however, each individual nanoparticle is surrounded by other nanoparticles which are some distance away, with a different medium in between. In this case, the nanoparticles feel an effective permittivity, described by the Maxwell Garnett effective medium theory[11,12]†. This theory expresses the effective permittivity as a function of the packing density of the nanoparticles and their permittivity. Within this effective medium theory, the resonance condition becomes:

$$\epsilon_\mathrm{eff}(\lambda_\mathrm{res}) = -\epsilon_\mathrm{m}\frac{2+f}{1-f}. \tag{2.3}$$

Here f is the filling factor, describing the packing density as volume occupied by the nanoparticles divided by the total volume. When the nanoparticles are in solution, $f = 0$, and Eq. 2.3 reduces to Eq. 2.2.

The implication of Eq. 2.3 is that changing the spacing between the nanoparticles changes the resonance wavelength. As the dielectric constant of gold decreases almost linearly around the resonance frequency[13], decreasing f by increasing the interparticle spacing hence decreases λ_res. This can be seen clearly in Fig. 2.4, which shows the absorption spectra of nanoparticle arrays with different interparticle spacing.

To obtain this data, nanoparticle arrays were stamped on a glass substrate and illuminated from the top by a halogen light source. The absorption was determined by measuring the optical transmission though the arrays and substrate. Since the array quality varies

†Named after James Clerk Maxwell by his father; physicist William Garnett, James Clerk Maxwell Garnett was unrelated to the founder of classical electrodynamics.

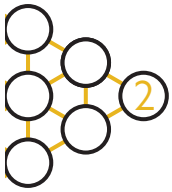

across the substrate, the absorption was determined on multiple locations and averaged. The measurement was done for four different spacers: octanethiol, decanethiol, dodecanethiol and tetradecanethiol, and the maximum was determined by fitting a Lorentzian distribution offset by a line to the data. The resonance frequencies clearly decrease when increasing the distance between the nanoparticles.

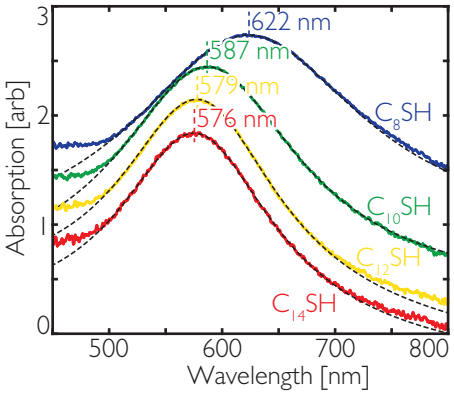

Fig. 2.4: Absorption spectra of nanoparticle networks with different interparticle spacing. The change in spacing is achieved by using different capping ligands: octanethiol, decanethiol, dodecanethiol and tetradecanethiol (C_8SH, $C_{10}SH$, $C_{12}SH$, $C_{14}SH$, respectively). Each curve is offset for visual clarity. The absorption maxima are obtained by fitting a Lorentzian offset by a line to the data points close to the maximum (best fit is shown as the dashed black curves). As expected, increasing the interparticle spacing decreases λ_{res}. Results obtained together with Yuri Bonanno[14].

Changing the interparticle spacing not only changes the plasmon frequency, it also affects the resistance of the network. As electron transport between non-connected particles can (to first order) be described by tunneling through the spacer molecules, increasing this length exponentially increases the resistance. The next section will discuss a possible application of this effect and review current research.

2.3 HIGH SENSITIVITY QUANTUM STRAIN GAUGES

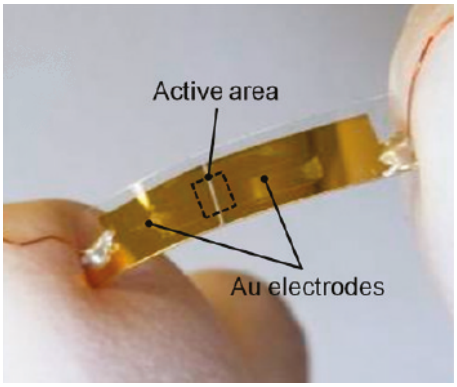

Fig. 2.5: A strain sensor device based on nanoparticle wires. Image by Farcau *et al.*[15].

A potential application of nanoparticle networks is high sensitivity strain sensors. Usually, strain measurements are done by metallic strain gauges. In these particular devices, a piece of metal is strained, leading to an increase in length and usually accompanied by a decrease in width. As the resistance of a material with resistivity ρ and dimensions l, w and h (for length, width and height respectively) is given by:

$$R = \rho \frac{L}{wh}, \tag{2.4}$$

the resistance increases as the length increases, and as the width and height decrease. Generally, this effect is small and therefore these devices are not very sensitive. Strain sensors are usually characterized by their gauge factor, which describes the change in resistance as a function of change in length:

$$GF \equiv \frac{\Delta R/R}{\epsilon}, \tag{2.5}$$

where R is the resistance, ΔR is the change in resistance and $\epsilon = \Delta L/L$ is the strain. For metallic strain devices, it is usually around 2. However, using nanoparticle networks as strain devices, seen in Fig. 2.5, can increase this factor by more than an order of magnitude[3,4]. Transport from nanoparticle to nanoparticle goes via electron tunnelling. Increasing the interparticle distance increases the tunnel barrier length, and therefore the resistance exponentially[16]. This should lead to large gauge factors in nanoparticle based strain sensors. Since strain in nanoparticle assemblies is related to the mechanical properties, let us first take a look at these properties before going into sensing.

2.3.1 MECHANICAL PROPERTIES

The use of capping ligands on nanoparticles allows one to create networks of nanoparticles on a liquid-air interface. This method can now be used to create freestanding membranes[17–22] of highly ordered networks. These membranes are held together strongly by the interactions between the capping molecules and can be suspended on the edges of micrometer sized holes[23] without further support. The strong interaction of the capping ligands, even when there is no crosslinking gives the membrane a stiffness of several GPa[23].

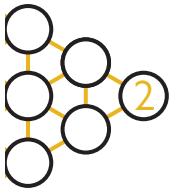

Because of the low mass and large Young's modulus, the oscillation frequencies of the membrane are located in the MHz range, as studied by Kanjanaboos *et al.* [23]. They used suspended membranes as microsized drumhead resonators and the resonance modes of these resonators were studied. The different resonant modes and drum diameters showed that the bending stiffness is negligible and that the drum tension is almost equal for drums created in the same process. Furthermore, the low mass and high Young's modulus enhance the sensitivity of the membrane to external influences.

In order for the nanoparticle strain gauges to work properly, a uniform strain is required. This is because if the network breaks at one position and remains unstrained at others, strain cannot be measured accurately -if at all. If the nanoparticles are more strongly coupled to the substrate than to each other, it might be expected that the strain is divided equally over the network. Siffalovic *et al.* [24] showed, using small angle x-ray scattering, that the strain in Fe_2O_3 nanoparticle networks on mylar is spead homogeneously over the substrate. Furthermore, it is also shown that the Poisson effect is negligible, as the interparticle distance along the direction perpendicular to the strain does not change. The maximum strain tested was 11% and the network showed no signs of tearing at this strain value. In comparison: metallic strain sensors acquire cracks at strains of 10% [25].

2.3.2 Strain sensors

Nanoparticle films as strain gauges were first studied experimentally by Herrmann *et al.* in 2007 [26]. They used disordered 200-nm films of gold nanoparticles capped by 4-nitrothiolphenol as spacers. For such networks, an exponential dependence of the resistance on strain was found, resulting in a gauge factor of 99. Similar experiments were done by Vossmeyer *et al.* [27] who found a gauge factor of ten to twenty.

The first experiments on ordered nanoparticle monolayers were done by Guedon *et al.* in 2011 [3]. Using the evaporation of a nanoparticle solution in chloroform on a convex water surface, an ordered membrane of nanoparticles was formed. This membrane was transferred to an insulated phosphor bronze substrate by a PDMS stamp. Strain was applied by a mechanically controlled bending array. A slight deviation from linear behavior of resistance on strain was found (see Fig. 2.6). It is useful to note that the actual strain cannot be accurately determined, since the strain on the substrate may not be ideally transferred to the network [28]. From the literature value of the tunnel barrier [29], a weakening of the strain transfer by a factor of five is derived. This results in a gauge factor of 25. Creating a network by inserting linker molecules leads to a decrease of the gauge factor by an order of magnitude. This is explained by the linker molecules changing positions on the nanoparticles, rather than stretching. The resulting change in resistance should therefore not be large.

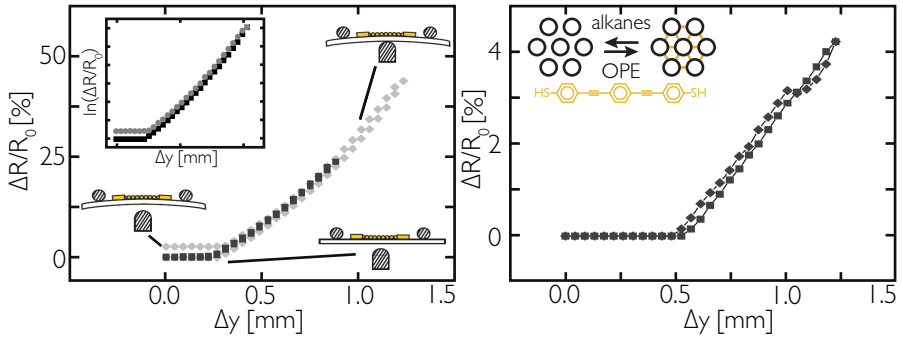

Fig. 2.6: Change in resistance as a function of push rod extension. Every millimeter of extension corresponds to roughly 1% of strain. Left shows a non-connected array whereas right shows a nanoparticle network connected by a conjugated molecular wire (shown in inset). Adapted from Guedon *et al.*[3].

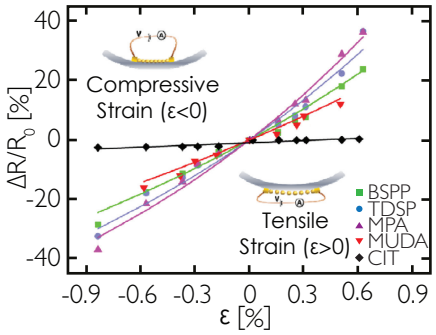

Fig. 2.7: Change in resistance as a function of applied strain. The different curves represent different ligands (from top to bottom: Bis(p-Sulfonatophenyl)PhenylPhosphine dihadrate dipotassium, Tris(4,6-Dimethyl-3-Sulfonatophenyl)Phosphine trisodium salt hydrate, MercaptoPropionic Acid, 11-MercaptoUnDecanoic Acid and citrate). The citrate capped nanoparticle array forms a metallic sheet and has a significantly lower gauge factor. Adapted from Moreira *et al.*[4].

Further studies were done by Moreira *et al.*[4] on gold nanoparticle multilayers. They studied the dependence of gauge factor on capping layer and used temperature dependent measurements to characterize their devices. As can be seen in Fig. 2.7, gauge factors of 20 to 40 are found. This figure also shows that the gauge factor can be tuned by changing the ligand molecules. A metallic nanoparticle array can even be fabricated by using citrate spacer molecules, dramatically decreasing the gauge factor. It should be noted that to obtain these gauge factors, ideal strain transfer of the substrate to the networks is assumed.

The gauge factors found by different groups agree up to an order of magnitude with each other. The found gauge factors are more than an order of magnitude larger than for metallic strain gauges. These found values are comparable to state of the art semiconductor strain gauges[26]. Furthermore, the strain factor might be increased even more by using multiple cotunnelling, a subject discussed in the next section. In the cotunnelling regime, the

increased interparticle spacing creates an even larger effect, since more junctions are probed at once. By changing the temperature or the charging energy, the average amount of hops is changed, which in turn tunes the gauge factor.

2.4 Electronic transport

As we saw in the last section, changing the interparticle spacing exponentially increases the resistance of the network. As a preliminary characterization, we checked this dependence by measuring the resistance of six samples with each 60 separate devices with a nanoparticle array stamped on top, each sample having nanoparticles with different spacers. Fig. 2.8 shows the resistances in a histogram for different alkanethiol spacers (C_8SH, $C_{10}SH$, $C_{12}SH$, $C_{14}SH$, $C_{16}SH$). Each individual bar graph shows the resistance versus the frequency of occurrence, the colors represent different spacers.

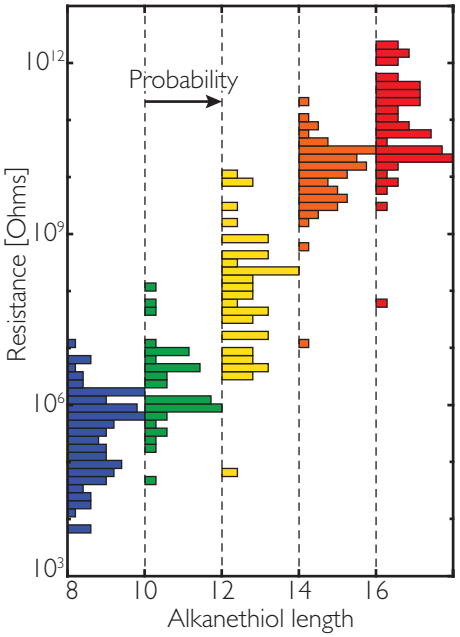

Fig. 2.8: Resistance of nanoparticle networks with different spacers, versus occurrence. Since 60 devices were measured for each spacer, the data is plotted as a histogram. The different colors represent different spacers (alkanethiol length indicating the number of carbon atoms in the thiol), shown on the x-axis, and the height of the bar shows the probability of the corresponding resistance value to occur. As can be seen, the average resistance increases approximately exponentially with increasing interparticle spacing. Additionally, there is a very large spread of over two orders of magnitude in the resistance values. This is most likely because the array quality is not very consistent across the sample.

The figure shows that the average resistance of the array increases exponentially with the interparticle spacing. Each addition of two carbon atoms increases the resistance roughly by an order of magnitude, agreeing with earlier experiments [30]. Additionally, it shows that the resistance varies greatly from device to device, as it has a spread of almost two orders of magnitude. We attribute this to the quality of the array varying across the sample and therefore from device to device. Furthermore, we have seen that the resistance of the network can decrease by one to two orders of magnitude over time in ambient atmosphere [31,32]. Since the

different devices are measured at room temperature in ambient atmosphere over the course of several hours, this can attribute to a significant part of the spread.

2.4.1 Resistance after molecular exchange

As a platform for molecular electronics, gold nanoparticle arrays are suitable because of molecular exchange. By interconnecting the network with the molecule of interest, its properties can be probed directly. However, in order to interconnect the array, the molecule needs to fit in between the particles. Intuitively, it can be expected that there is a certain optimal interparticle spacing for which the bridging molecule fits best, resulting in the lowest resistance. Together with Remco Overdevest, we investigated this prediction by measuring the resistance of arrays with different interparticle spacings before and after exchange with OPE3[‡]. The results of these measurements can be seen in Fig. 2.9.

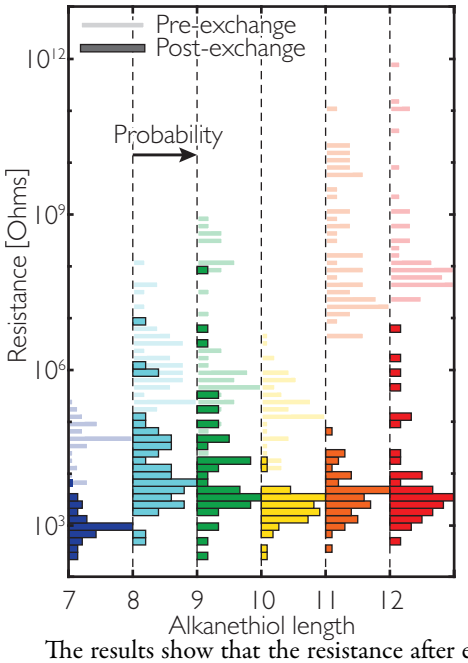

Fig. 2.9: Resistance of nanoparticle networks with different spacers, versus occurrence before and after molecular exchange. Resistance before molecular exchange is shown as the lighter colored bars with the white outline, after exchange is shown in darker colors with the black outline. It is clear that resistance post-exchange is orders of magnitude lower than before exchange, indicating successful interlinking. Interestingly, the post-exchange resistance seemingly does not depend strongly on the interparticle distance. Furthermore, with the exception of the heptanethiol-spaced network increasing the interparticle spacing decreases the resistance. If significant, this could be due to a higher network quality, as we generally found that longer thiols create higher quality networks. These results were obtained together with Remco Overdevest[31].

The results show that the resistance after exchange is drastically lowered compared to before exchange. Moreover, although the spread in pre-exchange resistance between the different spacers, this has almost no effect on the resistance post-exchange.

[‡]Although, the official chemical name of this molecule is S,S'-[1,4-Phenylenebis(2,1-ethynediyl-4,1-phenylene)]bis(thiol), it is almost never mentioned by this designation. OPE3 comes from Oligo-Phenylene-Ethynylene with 'two-and-a-half' repeating units. Since there are three phenyl rings, it is designated by the number three. Interestingly, OPE1 has only one phenyl ring and can therefore hardly be called an oligomer!

As we have seen in this section, electron transport through nanoparticle networks at room temperature already shows intriguing results. It is however at low temperatures where things become very interesting.

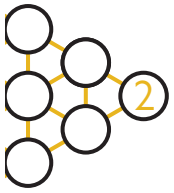

2.5 COULOMB BLOCKADE

§ Gold nanoparticles are small. Therefore, they have a very small capacitance: an isolated nanoparticle of 10 nm has a capacitance of 0.56 aF. This is important, as the energy needed to add an electron to the nanoparticle E_C scales inversely with its capacitance. In order to put an additional electron on the aforementioned particle, an energy of 140 meV is required:

$$E_C = \frac{Q^2}{2C} = \frac{1}{2}\frac{e^2}{4\pi\epsilon_0 r} = \frac{e}{2}\frac{1.6\cdot 10^{-9}\,\mathrm{C}}{5.6\cdot 10^{-18}\,\mathrm{F}} = 140\,\mathrm{meV}. \tag{2.6}$$

This is an energy six times higher than the thermal energy $k_B T$ at room temperature.

In a network, the nanoparticles couple to their surroundings, resulting in a higher capacitance and lower charging energy. However, upon cooling down, transport through the array will become non-Ohmic at some temperature. At room-temperature, electron transport through the array is mediated by sequential electron hopping from particle to particle. At low temperature and applied bias however, not every electron in the leads or the array has enough energy to charge a nanoparticle and contribute to transport. The current sharply decreases because transport is no longer possible. This phenomenon is called Coulomb blockade.

Coulomb blockade occurs when an electron cannot pass through a junction due to the large charging energy of the junction. The simplest device where Coulomb blockade can be observed is a single-electron transistor. Here, a metallic island is connected by tunnel junctions to a source and a drain electrode, and capacitively to a gate. Here, electron transport from the source to the drain involves an intermediate state where the electron is localized on the island. As the charging island has a characteristic capacitance, charging it requires an energy E_C, as we saw above. The effect of this capacitance comes into play when the system is cooled down to a temperature where the thermal energy is of the same magnitude as the charging energy ($k_B T \approx E_C$). Below this temperature, and as long as the source-drain voltage is lower than E_C/e, transport through the island is forbidden. Applying a positive voltage to the gate electrode lowers the energy levels of the island (the exact shift dependent on the island-gate coupling). When the gate voltage V_G is large enough so that the first charging state lies within the source-drain bias window, transport can occur through this, and only this state. The conductance as a function of gate voltage shows a periodic pattern, having a maximum each time a charging level crosses the bias window, which occurs when $\gamma e V_G = n E_C$, where n is an integer and $\gamma \equiv \Delta E/eV_G$ is the gate coupling.

§ This section is based on a part of the review article originally not written by me.

A network of nanoparticles can be seen as a system consisting of many of these metallic charging islands, each one coupled capacitively to the substrate and the neighbouring particles. Here, the electronic behavior is more complex, but it can be understood intuitively that the Coulomb charging energy of the nanoparticles play an integral role in electron transport. Determining this energy therefore gives a lot of information about the array. This implies that there exists a voltage threshold below which the current deviates from Ohmic behavior[33–35]. As there are many nanoparticles between the source and drain, the bias is divided over all nanoparticles between these electrodes. Therefore, this threshold voltage is given by $V_{\text{th}} = \alpha N E_{\text{C}}$, where N is the number of nanoparticles between the electrodes and $0 < \alpha < 0.5$ is a prefactor determined by the lattice structure of the array[36,37]. However, it was found by Moreira *et al.*[38] that changing the scale of the IV curve, actually changes V_{th}, which means that it cannot be a relevant parameter.

Alternatively, the Coulomb charging energy can be determined by measuring the zero-bias conductance at high temperatures ($E_{\text{C}} < k_{\text{B}}T$). Here, Duan *et al.*[39] have shown that this conductance follows Arrhenius behavior given by: $G(V{=}0) \propto \exp(-E_{\text{C}}/k_{\text{B}}T)$, as they found that the the logarithm of the zero-bias conductance scales inversely with temperature. Interestingly, E_{C} decreases after interconnecting the nanoparticles with OPE3. This makes intuitive sense, as the highly conducting molecules increase the dielectric constant of the surrounding medium[40], increasing the capacitance and hence decreasing the charging energy. As we saw in section 2.2, this change in the dielectric constant can be confirmed by measuring the shift in plasmon frequency after exchange.

2.6 BEYOND THE BLOCKADE: COTUNNELING

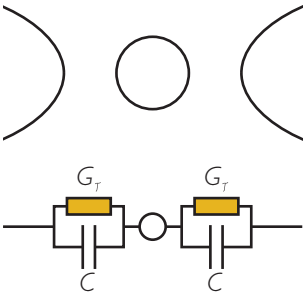

Fig. 2.10: Schematic depiction of a nanoparticle coupled to two leads through tunnel barriers with conductance G_T and capacitance C.

As seen in the previous section, when the electrostatic and thermal energy of the electrons is lower than the Coulomb charging energy (E_{C}) of the nanoparticles, electrons can no longer classically travel across the array. However, experimentally, transport is still found to occur[41,42]. This can be explained in terms of quantum fluctuations of the charge on the nanoparticle.[43] To illustrate this behavior, the device in Fig. 2.10. Two leads connect to a charging island (e.g. nanoparticle) from either sides. The island is connected to both leads by tunnel barriers (modeled by a resistor with conductance G_T in parallel to a capacitor). Due to the Heisenberg uncertainty relation of time and energy, an electron from the left lead can hop on and reside on the nanoparticle temporarily. In the same way, an electron on the nanoparticle can hop onto the right lead. If these two processes occur simultaneously, there is transport to

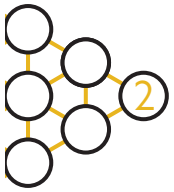

the right. One could imagine the same effect in the opposite direction, leading to transport to the left. Clearly, this takes place as well and the two processes cancel out when no bias is applied. When a bias is applied, however, symmetry is broken and one transport direction dominates the other. This type of transport is called cotunneling. There are two different kinds of cotunneling: elastic and inelastic. In elastic cotunneling, the energy of the electron is conserved, and it can be said that only one electron is involved in transport. The probability of elastic cotunneling is linearly dependent on applied bias and can only be observed at low bias and at low temperature [41]. Inelastic cotunneling does not conserve the phase of the electrons and two electrons take part in the transport process. The inelastic cotunneling current through a single nanoparticle junction can be written as:

$$I = \frac{1}{6\pi^2}\frac{G_{\mathcal{T}}^2}{G_0}\frac{(eV)^2 + (2\pi k_{\mathrm{B}}T)^2}{E_{\mathrm{C}}^2}V, \tag{2.7}$$

where $G_{\mathcal{T}}$ is the conductance of one of the tunnel barriers, $G_0 = {}^{2e^2}/_h$ is the conductance quantum and V is the voltage across the junction. The conductance $G_{\mathcal{T}}$ divided by G_0 is the transmission probability $\mathcal{T}$ of the tunnel barrier. The conductance is raised to the power two because of two uncorrelated tunneling events through the two tunnel barriers on either side of the nanoparticle. These both need to occur for transport to take place.

In networks of nanoparticles, transport is facilitated through multiple cotunneling. Several individual cotunneling events combine into one transport process involving multiple intermediate virtual states. Similar to regular cotunneling, the probability of a multiple cotunneling event over j nanoparticles scales with $G_{\mathcal{T}}^j$, as j intermediate states are involved in the process. Moreover, the current depends on the voltage to a higher power, with the exponent predicted to be dependent on the number of cotunneling hops [2], as discussed below.

The model for cotunneling was expanded by Tran *et al.* [44,45] for multiple junctions by adding an Arrhenius exponent to Eq. 2.7, comparing the voltage drop over a single junction and the charging energy of the junction to the temperature. This results in the following equation:

$$I \propto V_{\mathrm{jct}}G_0\sum_j\left(\frac{G}{G_0}\right)^j\left[\frac{(eV)^2 + (2\pi k_{\mathrm{B}}T)^2}{E_{\mathrm{C}}^2}\right]^{j-1} exp\left(\frac{jeV_{\mathrm{jct}} - {}^{E_{\mathrm{C}}}/_j}{k_{\mathrm{B}}T}\right), \tag{2.8}$$

where V_{jct} is the voltage drop across a single nanoparticle and j is the number of cotunneling hops. When $j = 2$, the amount of cotunneling hops is the same as in Eq. 2.7 and the equation takes the same form¶. An important characteristic of Eq. 2.8 is that the transmission

¶The 2π in the numerator of the center term is absent in the article by Tran *et al.* [45]. It is added in this equation out of consistency with Eq. 2.7.

probability of the tunnel barrier enters to the j^{th} power. This enhances the sensitivity of the system to the transmission of the barrier. Because events with various amounts of hops can contribute to the current simultaneously, the sum over j is taken.

It was observed experimentally that different I-V behavior appears at different temperatures [2,38,44,45]. The current follows a power law in voltage, where the exponent should be determined by the number of cotunneling events, as can be seen in Fig. 2.11. This behavior suggests that the number of cotunneling hops changes with temperature. At higher temperatures, the number of hops decreases to one, where cotunneling behavior makes way for activated sequential transport.

Cotunneling in large nanoparticle arrays was first reported by Tran *et al.* [44]. They studied the temperature dependence of electronic transport through ordered multilayers of varying thickness. It was found that at temperatures ranging from 30 K to 90 K, the conductance behavior can be explained by an Efros-Shklovskii (ES) variable range hopping model (where the zero bias conductance is: $G(V{=}0) \propto \exp\left(-\sqrt{T_0/T}\right)$, where T_0 is an activation temperature) [46]. The number of hops was found to depend on temperature. At higher temperatures, the transport follows Arrhenius behavior ($g_0 \propto \exp\left(-E_a/k_{\text{B}}T\right)$, where E_a is an activation energy).

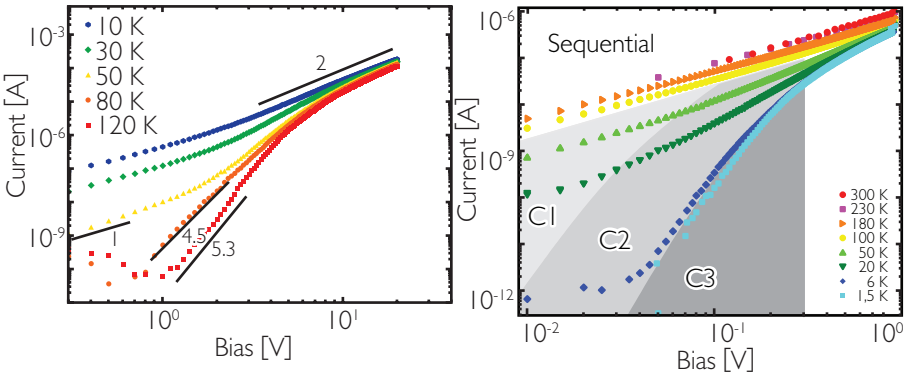

Fig. 2.11: Cotunneling current as a function of voltage measured by Tran *et al.* [45] (left) and Dayen *et al.* [2] (right). It can be clearly seen that the measurements done by Tran *et al.* are confirmed by Dayen *et al.*.

Later, Moreira *et al.* [38] reported different results (see Fig. 2.12). The I-V curves taken at low temperature showed Efros-Shklovskii behavior, dependent on voltage (here, the current scales as: $I \propto \exp\left(-\sqrt{V_{\text{ES}}/V}\right)$, where V_{ES} is an activation voltage), instead of the power law observed by Tran *et al.* [45]. At high temperatures, the Efros-Shklovskii behavior changes to an activated Arrhenius behavior also observed in the paper by Tran *et al.* [45].

These two different results were later connected by Dayen *et al.* [2] by inspecting Eq. 2.8

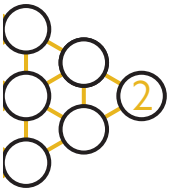

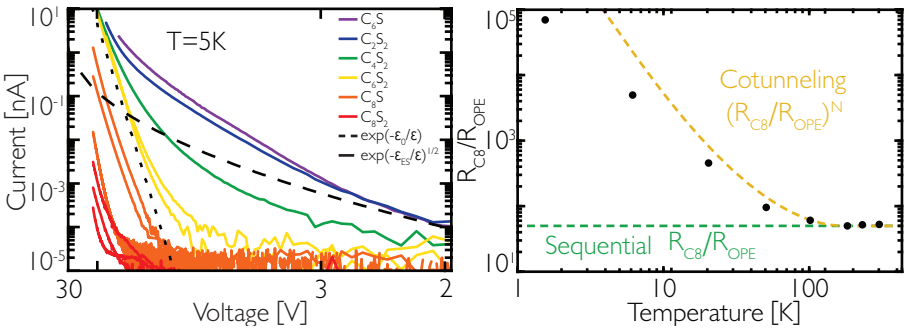

Fig. 2.12: Left: cotunneling current versus voltage for different ligands measured by Moreira *et al.*[38]. By changing the ligand, the behavior appears to change from Arrhenius to Efros-Shklovskii. Right: the enhancement of sensitivity to the used tunnel barrier[2]. The resistance ratio of alkanethiol to OPE is plotted as a function of temperature. It can be clearly seen that as the temperature decreases, the resistance ratio is enhanced due to the increase of the amount of cotunneling hops.

in more detail. Using the same Arrhenius exponent, the optimum number of cotunneling hops was deduced. It was found that the electronic behavior during cotunneling can be split in three regimes, dependent on temperature:

$$
\begin{aligned}
&C1: I \propto V && \text{when} \quad eV_{\text{jct}} \ll k_{\text{B}}T, \\
&C2: I \propto V^{2j_{\text{mean}}-1} && \text{when} \quad k_{\text{B}}T < eV_{\text{jct}} < k_{\text{B}}T \ln\left(\frac{e^2 R_{\mathcal{T}}}{h}\right), \\
&C3: I \propto e^{-\sqrt{V^*/V}} && \text{when} \quad k_{\text{B}}T \ln\left(\frac{e^2 R_{\mathcal{T}}}{h}\right) < eV_{\text{jct}},
\end{aligned}
\tag{2.9}
$$

where j_{mean} is the average number of cotunneling hops. It can therefore be concluded that the observed behavior in previous papers comes from the same process, though in different regimes.

An interesting consequence of Eq. 2.9 is that in the C2-regime, the conductance of the arrays no longer scales linearly with the conductance of the average nanoparticle-molecule-nanoparticle junction $G_{\mathcal{T}}$. Instead, the device resistance scales with the $G_{\mathcal{T}}$ to some power N. This may actually open the road for artificial enhancements of on-off ratios of switchable devices. If a single molecular switch has an on-off ratio $Q > 1$, the on-off ratio of the device in the cotunneling regime can be as much as Q^N, with N the number of cotunneling hops involved.

To test the principle idea, Dayen *et al.*[2] have compared the low-bias resistances of oc-

tanethiol and exchange OPE-dithiol devices. As can be seen in Fig. 2.12 (right figure), the resistance ratio is around 50 at 300 K (where transport is sequential), but increases dramatically at lower temperatures. This enhancement is explained in terms of cotunneling. One of the goals of the research discussed in this thesis is to investigate this prediction. The results of this study can be found in chapter 6.

Before continuing however, it is worthwhile to note that Eq. 2.8 diverges at large applied bias where $eV_{\text{jct}} > E_{\text{C}}$. Additionally, one might wonder if the *ad hoc* addition of the exponential Arrhenius term is adequate to accurately describe the behavior. Because of this, we will propose an alternative model, discussed in chapter 5.

Morover, cotunneling behavior is only explored for junctions connected by tunnel barriers where an energy independent transmission probability is assumed. Using this ohmic conductance simplifies the expression. Since this is not true for molecules and most other junctions, it should be interesting to see how this behavior changes when energy-dependent tunneling is taken into account, an issue that will be discussed in the next chapter.

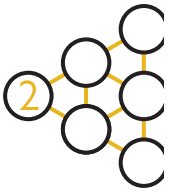

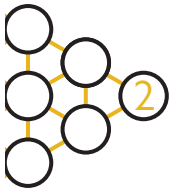

References

[1] Sense Jan van der Molen, Jianhui Liao, Tibor Kudernac, Jon S. Agustsson, Laetitia Bernard, Michel Calame, Bart J. van Wees, Ben L. Feringa, and Christian Schönenberger. Light-controlled conductance switching of ordered metal molecule metal devices. *Nano Letters*, 9(1):76–80, 2009.

[2] Jean-Francois Dayen, Edwin Devid, Mutta Venkata Kamalakar, Dmitry Golubev, Constant Guédon, Vina Faramarzi, Bernard Doudin, and Sense Jan van der Molen. Enhancing the molecular signature in molecule-nanoparticle networks via inelastic cotunneling. *Advanced Materials*, 25(3):400–404, 2013.

[3] C M Guédon, J Zonneveld, H Valkenier, J C Hummelen, and S J van der Molen. Controlling the interparticle distance in a 2d molecule nanoparticle network. *Nanotechnology*, 22(12):125205, 2011.

[4] Helena Moreira, Jérémie Grisolia, Neralagatta M Sangeetha, Nicolas Decorde, Cosmin Farcau, Benoit Viallet, Ke Chen, Guillaume Viau, and Laurence Ressier. Electron transport in gold colloidal nanoparticle-based strain gauges. *Nanotechnology*, 24(9): 095701, 2013.

[5] James S. Cooper, Mathew Myers, Edith Chow, Lee J. Hubble, Julie M. Cairney, Bobby Pejcic, Karl-H. Müller, Lech Wieczorek, and Burkhard Raguse. Performance of graphene, carbon nanotube, and gold nanoparticle chemiresistor sensors for the detection of petroleum hydrocarbons in water. *Journal of Nanoparticle Research*, 16(1), 2014.

[6] Jan W . Slot and Hans J . Geuze. A new method of preparing gold probes for multiple-labeling cytochemistry. *European journal of cell biology*, 38 1:87–93, 1985.

[7] Jianhui Liao, Xinxing Li, Ying Wang, Chaoying Zhang, Jinling Sun, Chao Duan, Qing Chen, and Lianmao Peng. Patterned Close-Packed Nanoparticle Arrays with Controllable Dimensions and Precise Locations. *Small*, 8(7):991–996, 2012.

[8] X. M. Lin, H. M. Jaeger, C. M. Sorensen, and K. J. Klabunde. Formation of Long-Range-Ordered Nanocrystal Superlattices on Silicon Nitride Substrates. *The Journal of Physical Chemistry B*, 105(17):3353–3357, 2001.

[9] Laetitia Bernard. *Expanding the horizon of molecular electronics via nanoparticle assemblies*. PhD thesis, University of Basel, 2006.

[10] Gustav Mie. Beiträge zur optik trüber medien, speziell kolloidaler metallösungen. *Annalen der physik*, 330(3):377–445, 1908.

[11] J.C. Maxwell Garnett. Colours in Metal Glasses and in Metallic Films. *Philosophical Transactions of the Royal Society of London*, 203(377), 1904.

[12] R. W. Cohen, G. D. Cody, M. D. Coutts, and B. Abeles. Optical properties of granular silver and gold films. *Physical Review B*, 8(8):3689, 1973.

[13] David R. Lide. *CRC Handbook of Chemistry and Physics*. CRC Press, 2007.

[14] Yuri Bonanno. Investigating the presence of molecular switches on a 2d gold nanoparticle network after molecular place-exchange. Master's thesis, Universiteit Leiden, 2017.

[15] Cosmin Farcau, Helena Moreira, Benoit Viallet, Jeremie Grisolia, Diana Ciuculescu-Pradines, Catherine Amiens, and Laurence Ressier. Monolayered wires of gold colloidal nanoparticles for high-sensitivity strain sensing. *The Journal of Physical Chemistry C*, 115(30):14494–14499, 2011.

[16] K.-H. Müller, J. Herrmann, B. Raguse, G. Baxter, and T. Reda. Percolation model for electron conduction in films of metal nanoparticles linked by organic molecules. *Physical Review B*, 66(7), 2002.

[17] Klara E. Mueggenburg, Xiao-Min Lin, Rodney H. Goldsmith, and Heinrich M. Jaeger. Elastic membranes of close-packed nanoparticle arrays. *Nature Materials*, 6 (9):656–660, 2007.

[18] Jinbo He, Xiao-Min Lin, Henry Chan, Lela Vuković, Petr Král, and Heinrich M. Jaeger. Diffusion and filtration properties of self-assembled gold nanocrystal membranes. *Nano Letters*, 11(6):2430–2435, 2011.

[19] Jinbo He, Pongsakorn Kanjanaboos, N. Laszlo Frazer, Adam Weis, Xiao-Min Lin, and Heinrich M. Jaeger. Fabrication and mechanical properties of large-scale freestanding nanoparticle membranes. *Small*, 6(13):1449–1456, 2010.

[20] Angang Dong, Xingchen Ye, Jun Chen, and Christopher B. Murray. Two-dimensional binary and ternary nanocrystal superlattices: The case of monolayers and bilayers. *Nano Letters*, 11(4):1804–1809, 2011.

[21] Angang Dong, Jun Chen, Patrick M. Vora, James M. Kikkawa, and Christopher B. Murray. Binary nanocrystal superlattice membranes self-assembled at the liquid-air interface. *Nature*, 466(7305):474–477, 2010.

[22] Wenlong Cheng, Michael J. Campolongo, Judy J. Cha, Shawn J. Tan, Christopher C. Umbach, David A. Muller, and Dan Luo. Free-standing nanoparticle superlattice sheets controlled by DNA. *Nature Materials*, 8(6):519–525, 2009.

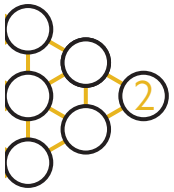

[23] Pongsakorn Kanjanaboos, Xiao-Min Lin, John E. Sader, Sara M. Rupich, Heinrich M. Jaeger, and Jeffrey R. Guest. Self-assembled nanoparticle drumhead resonators. *Nano Letters*, 13(5):2158–2162, 2013.

[24] P. Siffalovic, L. Chitu, K. Vegso, E. Majkova, M. Jergel, M. Weis, S. Luby, I. Capek, J. Keckes, G. A. Maier, A. Satka, J. Perlich, and S. V. Roth. Towards strain gauges based on a self-assembled nanoparticle monolayer-SAXS study. *Nanotechnology*, 21 (38):385702, 2010.

[25] J.R. Bautista, F. Avilés, A.I. Oliva, O. Ceh, and J.E. Corona. Correlations between mechanical stress, electrical conductivity and nanostructure in al films on a polymer substrate. *Materials Characterization*, 61(3):325–329, 2010.

[26] J. Herrmann, K.-H. Müller, T. Reda, G. R. Baxter, B. Raguse, G. J. J. B. de Groot, R. Chai, M. Roberts, and L. Wieczorek. Nanoparticle films as sensitive strain gauges. *Applied Physics Letters*, 91(18):183105, 2007.

[27] Tobias Vossmeyer, Carsten Stolte, Michael Ijeh, Andreas Kornowski, and Horst Weller. Networked gold-nanoparticle coatings on polyethylene: Charge transport and strain sensitivity. *Advanced Functional Materials*, 18(11):1611–1616, 2008.

[28] S. Vrouwe, E. van der Giessen, S. van der Molen, D. Dulic, M. Trouwborst, and B. van Wees. Mechanics of lithographically defined break junctions. *Physical Review B*, 71 (3), 2005.

[29] Hylke B Akkerman and Bert de Boer. Electrical conduction through single molecules and self-assembled monolayers. *Journal of Physics: Condensed Matter*, 20(1):013001, 2008.

[30] Vincent B. Engelkes, Jeremy M. Beebe, and C. Daniel Frisbie. Length-dependent transport in molecular junctions based on sams of alkanethiols and alkanedithiols: Effect of metal work function and applied bias on tunneling efficiency and contact resistance. *Journal of the American Chemical Society*, 126(43):14287–14296, 2004.

[31] Remco Overdevest. Characterizing exchange in nanoparticle arrays. Master's thesis, Universiteit Leiden, 2016.

[32] Constant M. Guedon. *Charge: Relating orbital structures to the conductance properties*. PhD thesis, Universiteit Leiden, 2012.

[33] Amir Zabet-Khosousi and Al-Amin Dhirani. Charge Transport in Nanoparticle Assemblies. *Chemical Reviews*, 108(10):4072–4124, 2008.

[34] A. Alan Middleton and Ned S. Wingreen. Collective transport in arrays of small metallic dots. *Physical review letters*, 71(19):3198, 1993.

[35] Milovan Šuvakov and Bosiljka Tadić. Modeling collective charge transport in nanoparticle assemblies. *Journal of Physics: Condensed Matter*, 22(16):163201, 2010.

[36] Raghuveer Parthasarathy, Xiao-Min Lin, Klara Elteto, T. F. Rosenbaum, and Heinrich M. Jaeger. Percolating through Networks of Random Thresholds: Finite Temperature Electron Tunneling in Metal Nanocrystal Arrays. *Physical Review Letters*, 92 (7), 2004.

[37] Klara Elteto, Eduard G. Antonyan, T. T. Nguyen, and Heinrich M. Jaeger. Model for the onset of transport in systems with distributed thresholds for conduction. *Physical Review B*, 71(6), 2005.

[38] H. Moreira, Q. Yu, B. Nadal, B. Bresson, M. Rosticher, N. Lequeux, A. Zimmers, and H. Aubin. Electron cotunneling transport in gold nanocrystal arrays. *Physical Review Letters*, 107(17), 2011.

[39] Chao Duan, Ying Wang, Jinling Sun, Changrong Guan, Sergio Grunder, Marcel Mayor, Lianmao Peng, and Jianhui Liao. Controllability of the Coulomb charging energy in close-packed nanoparticle arrays. *Nanoscale*, 5(21):10258, 2013.

[40] Laetitia Bernard, Yavor Kamdzhilov, Michel Calame, Sense Jan van der Molen, Jianhui Liao, and Christian Schönenberger. Spectroscopy of molecular junction networks obtained by place exchange in 2D nanoparticle arrays. *The Journal of Physical Chemistry C*, 111(50):18445–18450, 2007.

[41] A. E. Hanna, M. T. Tuominen, and M. Tinkham. Observation of elastic macroscopic quantum tunneling of the charge variable. *Physics Review Letters*, 68(21):3328, 1992.

[42] L. J. Geerligs, D. V. Averin, and J. E. Mooij. Observation of macroscopic quantum tunneling through the coulomb energy barrier. *Physical review letters*, 65(24):3037, 1990.

[43] D. V. Averin and Yu V. Nazarov. Virtual electron diffusion during quantum tunneling of the electric charge. *Physics Review Letters*, 65(16):2446–2449, 1990.

[44] T. Tran, I. Beloborodov, X. Lin, T. Bigioni, V. Vinokur, and H. Jaeger. Multiple cotunneling in large quantum dot arrays. *Physical Review Letters*, 95(7), 2005.

[45] T. Tran, I. Beloborodov, Jingshi Hu, X. Lin, T. Rosenbaum, and H. Jaeger. Sequential tunneling and inelastic cotunneling in nanoparticle arrays. *Physical Review B*, 78(7), 2008.

[46] A. L. Efros and B. I. Shklovskii. Coulomb gap and low temperature conductivity of disordered systems. *Journal of Physics C: Solid State Physics*, 8(4):L49, 1975.

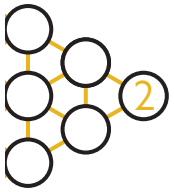

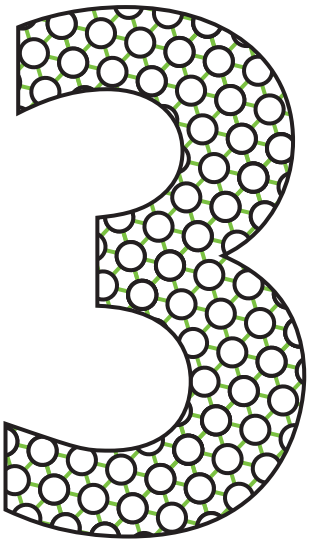

Cotunneling with energy dependent contact transmission

This chapter has been published as:
Inelastic cotunneling with energy-dependent contact transmission
S. Blok, R.R. Agundez Mojarro, L.A. Maduro, M. Blaauboer, S.J. van der Molen
Journal of Chemical Physics, 2016

3.1 Introduction

As discussed in chapter 2, at sufficiently low temperature and applied bias, electron transport through a gold nanoparticle array is expected to be dominated by higher order processes, specifically: multiple inelastic cotunneling. Multiple inelastic cotunneling involves two or more electrons that all contribute to the transport process. Since the intermediate states are energetically forbidden, this form of transport binds the fates of two or more electrons together in one transport event. In cotunneling, electrons are the ultimate party poopers; if one electron does not contribute to the event, none of the electrons will and transport does not occur. Since each single electron contribution is independent of the other, it can be easily seen that the resulting current scales with the single electron transmission probability to the N$^{\text{th}}$ power $I \propto \mathcal{T}^N$, where $N \geqslant 2$ is related to the amount of electrons involved[1,2]. This can also be seen in the previous chapter; in Eq. 2.7 the current scales with the conductance to the second power. Here, there are two electrons involved, and the conductance is proportional to the single electron transmission probability.

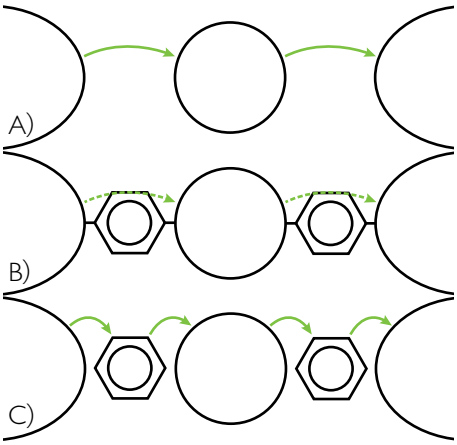

Fig. 3.1: Three approaches to the cotunneling problem. **A**: the original method developed by Nazarov *et al.*[3]. Here, the electrons tunnel through tunnel barriers with energy independent transmission probability in a single cotunneling process. **B**: electrons go from left to right via a single cotunneling process, but the transmission probability of the electrons depends on their incoming energy. **C**: an adaptation of the multiple cotunneling model[4]. Electrons go from the left lead to the right lead via a multiple cotunneling process through various virtual states. Since the molecules are modeled as single levels as opposed to the leads and nanoparticle, cotunneling through the molecules is elastic, whereas tunneling through the nanoparticle is inelastic.

Thus far, the resulting cotunneling current has only been calculated for systems in which the transmission probability is independent of energy. This assumption does not generally apply to molecules bridging between neighboring nanoparticles however, as molecular transmission functions can be strongly energy-dependent. Understanding the influence of the latter is not only of fundamental interest; it is also relevant for practical devices, since cotunneling can be utilized to enhance the signature of the molecules bridging[5] the nanoparticles in an array. If, for example, the bridges are formed by molecular switches, the ratio between the conductance in the 'on' and the 'off' state can be artificially increased. In this

chapter, we study the effect of an energy-dependent transmission function on transport between nanoparticles in the Coulomb blockade regime. We propose two methods (outlined in Fig. 3.1B,C) to tackle this problem.

3.2 THEORY OF COTUNNELING MECHANISMS

In this section we briefly review the mechanisms of inelastic cotunneling. Classically, when a system is Coulomb blockaded, no current is expected to flow. However, it was predicted [3] and found experimentally [6,7] that due to quantum corrections, this is not completely the case. The current flowing in the Coulomb blockade regime is due to the process of cotunneling [3]. Cotunneling is the simultaneous transfer of multiple electrons through energetically forbidden virtual states. The basic mechanism is as follows. Consider the device illustrated in Fig. 3.1A. Two leads connect to a charging island from either side through a tunnel barrier. An electron can temporarily hop from the left lead onto the charging island. The resulting virtual charge state is energetically forbidden, but temporarily allowed by the Heisenberg uncertainty relation. In this time window, an electron already residing on the island may hop onto the right lead. If these two processes occur within this time window, an electron has effectively been transferred from the left to the right lead. The reverse process (i.e. to the right lead) is also possible, but the symmetry between these processes is broken by applying a voltage bias. The final charge state of the island is equal to the initial charge state, complying with total energy conservation.

There are two different types of cotunneling; elastic and inelastic. Elastic cotunneling can only be observed at sufficiently low bias and temperature [6], compared to the quantum level spacing of the charging island. In an elastic cotunneling process, the electron hopping onto the charging island and the electron hopping off have the same energy. In inelastic cotunneling, this is not the case. This results in the charging island being left in an excited state after the process. The inelastic cotunneling current through a single junction as depicted in Fig. 3.1A can be written as [3]:

$$I = \frac{1}{6\pi^2} G_0 \mathcal{T}^2 \frac{(eV)^2 + (2\pi k_B T)^2}{E_C^2} V, \tag{3.1}$$

where $\mathcal{T}$ is the transmission probability of the tunnel barrier, $G_0 = {}^{2e^2}/_h$ is the conductance quantum, E_C is the charging energy of the island, T is the temperature, k_B is the Boltzmann constant, e is the elementary charge and V is the voltage across the junction. Since two barrier transmissions are needed for transport to occur, it makes intuitive sense that $I \propto \mathcal{T}^2$. However, in the derivation of Eq. 3.1, it has been assumed that the transmission probability of the tunnel barriers is independent of energy. While this is normally a reasonable assumption, it is not always the case. In this chapter, we will explore the possibility of an energy-dependent transmission function. In the next section we consider the case where the two leads are connected to the nanoparticle through molecules, as seen in Fig. 3.1B. The

contact transmission is then expected to become dependent on electron energy, assuming a Lorentzian lineshape.

3.3 Approach 1: Lorentzian transmission

In this section, we will assume that each of the two molecules involved in the cotunneling problem can be represented by a single level, symmetrically connected to a lead and the central nanoparticle (see Fig. 3.1B). Furthermore, we will suppose that transport through each molecule is coherent, such that the transmission function becomes Lorentzian with a width determined by the lead-molecule coupling[8]. Still, inelastic cotunneling behavior in the full molecule-nanoparticle-molecule system is to be derived by allowing for virtual excitations. More specifically, an electron in the lead, with an energy E_{L}, will temporarily take up a different energy, E_{S2}, within the nanoparticle. As a result, the exact energy of electron transmission through the molecule is somewhat ill-defined. To circumvent this problem, we will assume that any change of energy, related to the formation of a virtual state, happens inside the nanoparticle. In that case, the molecular transmission function depends only on the energy of the incoming electron. Summarizing, we assume that all virtual processes take place within the charging island, while transmission through the molecules can still be described by the Lorentzian functions in Eq. 3.2:

$$\begin{aligned}\mathcal{T}_{\mathrm{M1}}(E_{\mathrm{L}}) &= \frac{\Gamma^2}{\left(E_{\mathrm{L}} - \epsilon_{\mathrm{L}} - \eta_{\mathrm{L}} eV\right)^2 + \Gamma^2},\\ \mathcal{T}_{\mathrm{M2}}(E_{\mathrm{S1}}) &= \frac{\Gamma^2}{\left(E_{\mathrm{S1}} - \epsilon_{\mathrm{R}} - \eta_{\mathrm{R}} eV\right)^2 + \Gamma^2}.\end{aligned} \tag{3.2}$$

Here Γ is the half width half maximum of the Lorentzian which takes into account lead-molecule and molecule-nanoparticle coupling, ϵ_{R} and ϵ_{L} are the resonance energies of the molecular levels (we take $\epsilon_{\mathrm{R}} = \epsilon_{\mathrm{L}}$ in our calculations), $E_{\mathrm{L}}, E_{\mathrm{S1}}$ are the incoming electron energies and ηeV determines the shift of the level as an effect of the applied voltage. We take $\eta_{\mathrm{L(R)}} = (-)1/4$ in every calculation, implying an equal coupling to both the lead and the nanoparticle. Note that the maximum of the transmission function is taken to be unity.

To calculate the transition rate $\mathcal{R}$ from the initial state $|i\rangle$ to the final state $|f\rangle$, the Fermi Golden Rule[9] can be expanded in order to sum over all virtual states $|v\rangle$. Within this perturbative approach, the small parameter is the coupling between the nanoparticle and the two leads. The rate is given by:

$$\mathcal{R} = \frac{2\pi}{\hbar} \sum_{v} \left| \frac{\langle i|\hat{H}|v\rangle \ \langle v|\hat{H}|f\rangle}{E_v - E_{\mathrm{i}}} \right|^2 \delta(E_{\mathrm{i}} - E_{\mathrm{f}}), \tag{3.3}$$

where the delta function ensures total energy conservation. $\hat{H}$ is the same Hamiltonian as

used by Averin *et al.*, Eq. 1 [3], pragmatically extended to include energy-dependent transmission through the molecules. The initial, virtual and final states are the unperturbed eigenstates of the molecule-nanoparticle-molecule system. The process amplitude should scale with the lifetime of the virtual state which is inversely proportional to the energy difference between the initial and virtual states: $E_\mathrm{i} - E_v$. There are two different virtual states as can be seen in Fig. 3.2. Either an electron on the left lead tunnels through the molecule to the nanoparticle, or an electron first goes from the nanoparticle through the molecule to the right lead. These processes are complementary; if the former process causes the virtual state, the latter leads to the final state and vice versa. For a system depicted in Fig. 3.2 the expression for the rate $\mathcal{R}$ is given in Eq. 3.4.

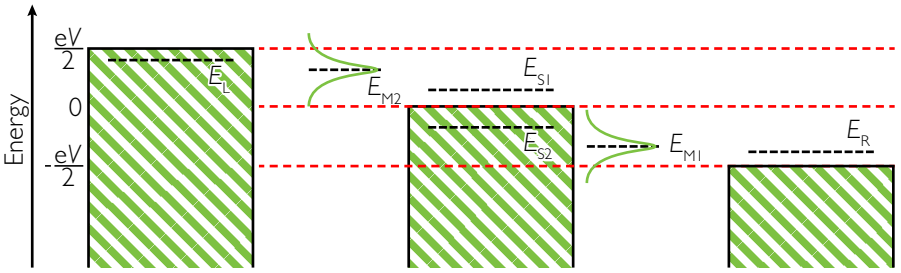

Fig. 3.2: Energy diagram of a charging island coupled to two leads with an applied bias voltage V. E_L and E_R are the electron energies of the left lead and the right lead, respectively. $E_{\mathrm{S}1}$ and $E_{\mathrm{S}1}$ are electron energies on the charging island.

$$\mathcal{R} = \frac{2\pi}{\hbar}\int_{\boldsymbol{E}} \mathcal{T}_{\mathrm{M}1}(E_\mathrm{L})\mathcal{T}_{\mathrm{M}2}(E_{\mathrm{S}1})\left[\frac{1}{\Delta E_{\mathrm{v}1}}+\frac{1}{\Delta E_{\mathrm{v}2}}\right]^2 \times F_\mathrm{FD}\delta(E_\mathrm{i}-E_\mathrm{f})\,\mathrm{d}E_\mathrm{L}\mathrm{d}E_\mathrm{R}\mathrm{d}E_{\mathrm{S}1}\mathrm{d}E_{\mathrm{S}2}, \quad (3.4)$$

$$F_\mathrm{FD} = f(E_\mathrm{L})\big[1-f(E_{\mathrm{S}2})\big]f(E_{\mathrm{S}1})\big[1-f(E_\mathrm{R})\big].$$

Here, the sum over virtual states has been replaced by an integral over all relevant energies. In Eq. 3.4, the matrix elements from Eq. 3.3 have been replaced by transmission probabilities $\mathcal{T}_{\mathrm{M}1}(E_\mathrm{L})$ and $\mathcal{T}_{\mathrm{M}2}(E_{\mathrm{S}1})$ analogously to Averin *et al.* [3], depending on the incoming electron energies E_l and $E_{\mathrm{S}1}$. It should be noted that these transmission functions are chosen for their general applicability and ease of understanding. The model presented here is not limited to these Lorentzian-shaped transmission functions, however and would work with other transmission functions as well. The energies E_L, $E_{\mathrm{S}2}$, E_R, $E_{\mathrm{S}1}$ are depicted

in Fig. 3.2. The energies ΔE_{v1} and ΔE_{v2} are defined as the energy differences between the initial and the first and second virtual state respectively. The occupation of states on the leads and nanoparticle are taken into account by their Fermi-Dirac distributions $f(E)$ (a derivation can be found in Appendix A).

Using Matlab we now calculate the cotunneling current $I(V)$ and differential conductance $^{dI}/_{dV}$ by solving Eq. 3.4 numerically for the system in Fig. 3.2. To test the validity of our approach, current versus voltage ($^{dI}/_{dV}$) was calculated for increasing coupling Γ for resonant transport ($\epsilon = \epsilon_L = \epsilon_R = 0$). As the coupling increases, the width of the transmission function (as seen in Eq. 3.2) increases. The consequence of this is that as Γ becomes larger, the cotunneling current should approach the constant transmission case. This can indeed be seen in Fig. 3.3. Here, Γ was varied from 3 meV to 1 eV and compared to the situation with constant transmission $\mathcal{T} = 1$, as derived by Averin *et al.*[3]. In Fig. 3.4 it can also be seen that as the coupling increases, the voltage at which the current starts to deviate from the constant-transmission case increases as well, as expected.

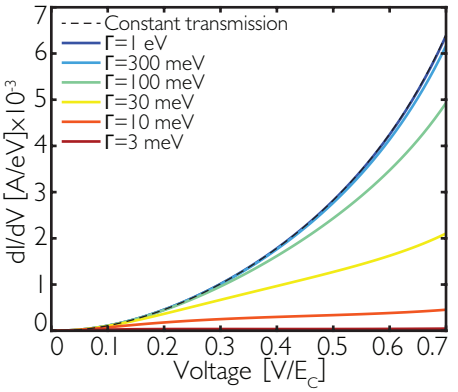

Fig. 3.3: Differential conductance ($^{dI}/_{dV}$) versus voltage curves for the system in Fig. 3.2 with varying Γ. It can be seen that as the coupling increases, the current approaches the constant transmission case, as is expected. The temperature is 116 K (10 $^{meV}/_{k_B}$), the charging energy E_C is 100 meV and we take $\epsilon_L = \epsilon_R = 0$ to ensure resonant transport through the molecules. The maximum value of the transmission function is unity in every case.

Next, we study the effects of molecular gating on the cotunneling current. Gating shifts the resonance position (ϵ_L and ϵ_R in Eq. 3.2) of the level. As a benchmark, let us first consider coherent transport through a single level connected to two leads, i.e. without Coulomb blockade. In that case, the maximal possible current can be calculated from the Landauer formula at 0 K.[10] (Eq. 3.5).

$$I = \frac{G_0}{e} \int_{-eV/2}^{eV/2} \mathcal{T}(E) \mathrm{d}E. \tag{3.5}$$

Clearly, the maximum possible current is the integral over the transmission function as $V \to \infty$. This (finite) number does not change if the peak of the Lorentzian is shifted and/or if the

temperature is changed to finite values.* In the cotunneling regime, the situation is different, as can be seen in Fig. 3.4. At low bias (for example at 0.2 $^{eV}/_{E_C}$), increasing $\epsilon = \epsilon_L = \epsilon_R$ away from zero, results in a decrease of the current indeed. However, at larger bias (for example at 0.45 $^{eV}/_{E_C}$), the current calculated for $\epsilon = 0$ meV is equal to the current found for $\epsilon = 5$ meV. In the $^{dI}/_{dV}$ (see Fig. 3.4B) at large bias (for example 0.7 $^{eV}/_{E_C}$), it can be seen that the differential conductance is larger for larger ϵ. This is never the case for systems without cotunneling, as the total current is only determined by the area of the transmission curve that is in the bias window. This suggests that cotunneling is selective for higher energy electrons, as long as the transmission function allows them to pass.

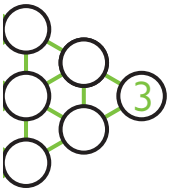

*As we saw in chapter 1, the maximum current is given by: $G_0\Gamma/e$

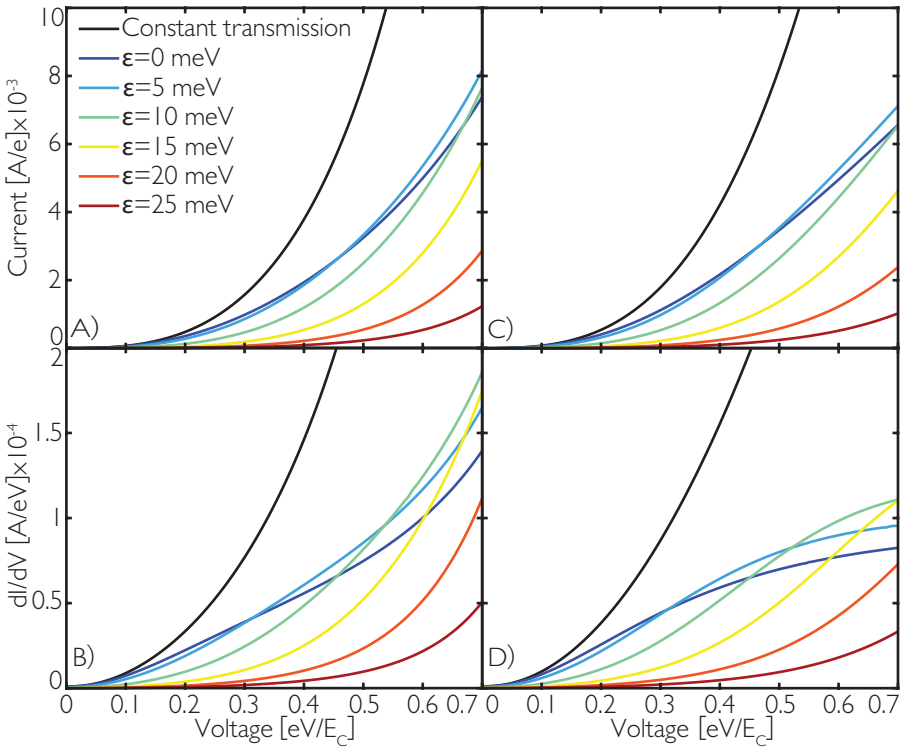

Fig. 3.4: Plots of current and differential conductance versus voltage for the system in Fig. 3.2, with ϵ varying from 0 to 25 meV (corresponding colors for all plots are denoted in A). The temperature is 12 K (1 $^{\text{meV}}/_{k_B}$), $\Gamma = 10$ meV and the charging energy $E_C = 100$ meV. The maximum transmission is unity in every case. The constant transmission curve (black) is added for reference. **A**: IV-plots. At low bias, the current decreases with increasing ϵ. However, as the bias gets larger, the difference decreases. At 0.45 $^{\text{eV}}/_{E_C}$, the curve for ϵ =0 meV crosses the curve for $\epsilon = 5$ meV; it even crosses the curve for ϵ =10 meV at 0.75 $^{\text{eV}}/_{E_C}$. **B**: dI/dV-curves derived from A, magnifying the trends observed in A. It can be seen that at 0.7 $^{\text{eV}}/_{E_C}$, the current increases most rapidly for $\epsilon = 10$ meV. **C**: IV-curves calculated upon approximating the denominator of eq. 3.4 by E_C. The crossings are still present, although somewhat shifted compared to A. **D**: dI/dV-curves derived from C. Again, crossings are found, but the shape of the individual curves differs from B. This can be expected, since the denominator of Eq. 3.4 as used in A and B diverges, in contrast to the case of C and D.

To explore possible explanations for this effect, we first note that the cotunneling current is inversely proportional to $(E_v - E_i)^2$ (or ΔE^2), as can be seen in Eq. 3.3. Hence,

electrons with a higher energy are energetically closer to the island charging energy. Thus they have a lower ΔE, increasing their transmission probability (see Eq. 3.4). To test if this phenomenon could lead to the crossing of curves as found in Fig. 3.4A and B, we have done a similar calculation but have replaced the $1/\Delta E^2$ by $1/E_C^2$. The results can be seen in Fig. 3.4C. We find that even though the crossings from Fig. 3.4C, D have changed their position, they have not disappeared. We conclude that the ΔE^2 in the denominator cannot be the principal source of the crossings.

A second explanation for the crossings can be seen in Eq. 3.4. Here, the electron energy not only appears due to the Heisenberg uncertainty relation, but also in the overall conservation of energy. The delta function relating the initial to the final energy in Eq. 3.4 can be written as $\delta(E_{S1} + E_R - E_L - E_{S1} - eV)$. This means that as the voltage increases, more cotunneling pathways are opened to allow transport. If the peak of the transmission function is at this higher energy, these pathways can also tunnel through the molecule, increasing the total current. If the peak of the transmission function lies at a lower energy, the high energy pathways are blocked by the molecule and can therefore not contribute to the current.

To experimentally test the predictions made here, a device that can gate molecules selectively is required, as a back-gate would also gate the nanoparticle. This is non-trivial, however. Fortunately, it may also be possible to test our model using molecular switches[11]. Diarylethylene based switches, for example, do not only change their total transmission, but also the position of the resonances[12]. Our predictions could be examined on nanoparticle arrays interlinked by molecular bridges, but this would also require our model to include percolation effects[11]. A more direct evaluation can be done on nanogap devices with a single nanoparticle placed in between the electrodes using dielectrophoresis[13,14]. The current within the Coulomb blockade regime should then be compared to the current outside of it for both states of the switch. This allows for a direct test of the validity of the model proposed above.

In this section, we have assumed that the molecular coupling to the leads and nanoparticle is strong. However, if this coupling is weak, the charging energy of the molecule itself could start to play a role too[15]. In that case, elastic transmission through the molecule is no longer possible and the only allowed pathway from the left lead to the right is through multiple cotunneling. The next section discusses this problem.

3.4 Approach 2: Multiple cotunneling

In this section, we study the system depicted in Fig. 3.1C and introduce a charging energy to each (weakly coupled) molecule in order to shift transport across them to the Coulomb blockade regime. To study transport in this regime, we propose a second model based on higher order cotunneling. In the previous section our model consisted of a second-order cotunneling event with coherent transport through the molecule. However, if the molecular energy levels are Coulomb blockaded, direct tunneling through the molecule is no longer allowed. Therefore transport across the molecules will only occur through cotunneling. In the system depicted in Fig. 3.1C, an electron can be transferred from the left lead to the right lead by a fourth-order cotunneling event, consisting of a collective hopping through four junctions: left lead-molecule, molecule-nanoparticle, nanoparticle-molecule and molecule-right lead.

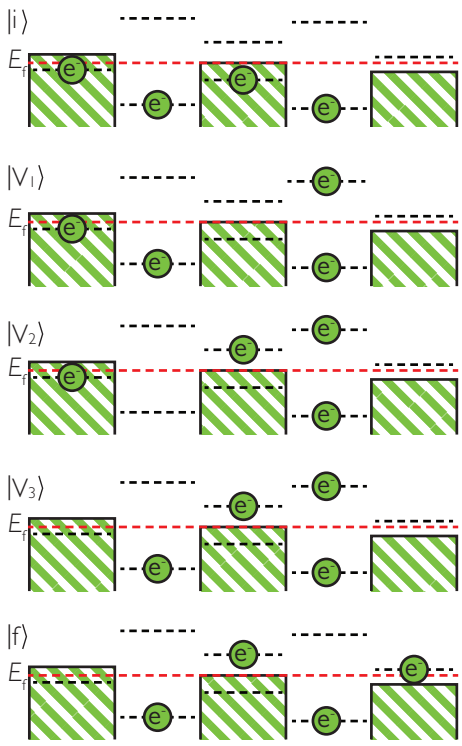

Fig. 3.5: The permutation $\{3, 2, 1, 4\}$ that contributes to the cotunneling current. Here, the process starts with an electron hopping from the nanoparticle to the right molecule, then from the left molecule to the nanoparticle, followed by an electron from the left lead to the left molecule and is completed by transfer from the right molecule to the right lead.

Transport across the nanoparticle is due to inelastic cotunneling. Since the molecules are modeled by a single level, transport across the molecule occurs through elastic cotunneling. Therefore, cotunneling transport in our system is of the fourth-order and consists of a collective combination of two elastic and one inelastic cotunneling events. In a second-order cotunneling event there are two possible hop permutations with distinct virtual states, as stated in the previous section. However, we now have four junctions, which means that there are $4!$ hop permutations, each with three virtual states. To calculate the total current in a four junction system, the contribution from each permutation needs to be taken into account. This can be done by considering the matrix

elements from Eq. 3.3 as:

$$M = \sum_{\{j_1,j_2,j_3,j_4\}} \prod_{k=1}^{3} \frac{\langle V_{k+1}| \hat{H} |V_k\rangle}{E_{\mathrm{V}_k} - E_{\mathrm{i}}} \langle V_1| H |i\rangle , \tag{3.6}$$

which sums over all possible permutations of the electron hops that yield the transport of an electron from the left lead to the right lead, e.g. $\{3, 2, 1, 4\}$ (see Fig. 3.5). The states $|V_k\rangle$ are the corresponding virtual states analogously to those defined in approach 1, used during the cotunneling process of each permutation, of which there are three per permutation. The Hamiltonian in Eq. 3.6 is the same as the one in Eq. 1 of Ref.[3], with two additional terms describing the two molecules (see below). The unperturbed eigenstates of the central molecule-nanoparticle-molecule region are represented, analogously to Ref.[3], as $|n_i\rangle$, with n_i ($i = \mathrm{M1}, \mathrm{NP}, \mathrm{M2}$) the number of electrons on molecule 1, the nanoparticle and molecule 2. The tunnel couplings between the left lead and left molecule, left molecule and nanoparticle, nanoparticle and right molecule and finally right molecule and right lead are the small parameters in this perturbative approach.

We model each molecule as a singly occupied energy level at the initial state as depicted in Fig. 3.5. This approximation is valid for a small bias if the energy level is in the Coulomb blockade regime, namely $\epsilon = -\frac{1}{2}E_{\mathrm{C,M}}$, where $E_{\mathrm{C,M}}$ is the Coulomb charging energy of the molecules. For the situation in Fig. 3.5, the initial energy for every permutation is $E_{\mathrm{i}} = E_{\mathrm{L}} + {}^{V}/_{2} + 2\epsilon + E_{\mathrm{S2}}$, and the final energy for every permutation is $E_{\mathrm{f}} = 2\epsilon + E_{\mathrm{S1}} + E_{\mathrm{R}} - {}^{V}/_{2}$. We can then write the total rate as a contribution of all possible initial and final energies, the sum of Eq. (3.3) for every set of energies, E_{L}, E_{R}, E_{S1} and E_{S2}. By converting the sum into an integral and the matrix elements $\langle V_{k+1}| \hat{H} |V_k\rangle$ in Eq. (3.6) into tunneling rates we write an explicit equation to calculate the cotunneling rate in our system[3,16] (see Appendix for details):

$$\begin{aligned}\mathcal{R} = &\frac{\hbar^3}{8\pi^3}\mathcal{T}_{\mathrm{M}}^4 \int_{\boldsymbol{E}} \left| \sum_{\{j_1,j_2,j_3,j_4\}} \prod_{k=1}^{3} \frac{1}{E_{\mathrm{V}_k} - E_{\mathrm{i}}} \right|^2 \\ &\times f_{\mathrm{FD}}\delta(E_{\mathrm{i}} - E_{\mathrm{f}})\mathrm{d}E_{\mathrm{L}}\mathrm{d}E_{\mathrm{R}}\mathrm{d}E_{\mathrm{S1}}dE_{\mathrm{S2}}.\end{aligned} \tag{3.7}$$

The Fermi distribution functions have been added to Eq. (3.7) to account for the probability of a state being empty or occupied, accordingly. The conservation of energy is taken into account by $\delta(E_{\mathrm{f}} - E_{\mathrm{i}})$. $\mathcal{T}_{\mathrm{M}}$ is the transmission probability for an electron going out of or into the molecule, $\mathcal{T}_{\mathrm{M}}$ takes the same role as $\mathcal{T}_{\mathrm{M1}}$ and $\mathcal{T}_{\mathrm{M2}}$ in Eq. 3.2, except that it is now assumed to be a constant (set to 1) independent of electron energy.

Moreover, the matrix element from Eq. 3.6 can be further simplified if we assume that the charging energy of the molecule and of the nanoparticle are larger than all other energies in the system. Interestingly, the energy independence of the matrix element results in the

multiple cotunneling behavior of the system reducing to singular cotunneling. This matrix element then becomes:

$$M = \frac{T_1^\dagger T_2^\dagger}{E_S}, \tag{3.8}$$

with $T_1^\dagger, T_2^\dagger$ taking into account the transmission probability to and from the molecules and E_S is a function of the charging energies of the molecules and nanoparticle. A complete derivation can be found in the appendix.

Using Matlab, we now calculate the cotunneling current ($I(V)$) by solving Eq. 3.7 numerically (see Fig. 3.6). We take the charging energy of the molecule to be ten times larger than the charging energy of the nanoparticle, $E_{C,M} = 10E_C$, together with a small bias voltage and $\epsilon = -\frac{1}{2}E_{C,M}$ ensures Coulomb blockade in the molecule and single occupancy. Analogously to our calculations in the previous section, we first calculate the current for varying molecular charging energies ($E_{C,M}$). From Eq. 3.7, we expect the current to decrease as the molecular charging energy increases. This can be seen in Fig. 3.6A.

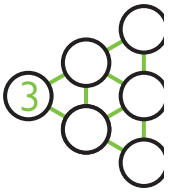

Since the amplitude of each pathway scales inversely with the product of all three energy differences ΔE_i, it can be expected that the total current should decrease with increasing molecular charging energy $E_{C,M}$. Furthermore, if the charging energies of the molecules and nanoparticle are much larger than both the electrostatic and thermal energies (eV and k_BT respectively) in the system, the shape of the I-V curves should not change when changing the charging energy. In Fig. 3.6B we have normalized each curve by the current at 70 meV. It can be seen that this moves the curves very close together, confirming our expectations. However, the rescaled curves are still not precisely identical.

If we now remove any thermal and electrostatic energy from the energy differences in the virtual pathways, we expect the IV-curves to fully overlap. Removing all energies except the charging energies in our calculation of the energy differences, we get the results shown in Fig. 3.6C. After normalization, these curves, displayed in Fig. 3.6D, lie fully on top of each other, as expected.

Interestingly, the calculations in this section predict that when a charging island is coupled to leads through Coulomb blockaded single levels, it is not possible to distinguish between multiple cotunneling and inelastic cotunneling with a constant transmission function (as derived by Averin *et al.* [3]). This holds for any system where transport across the system is through two instances of elastic cotunneling and one instance of inelastic cotunneling.

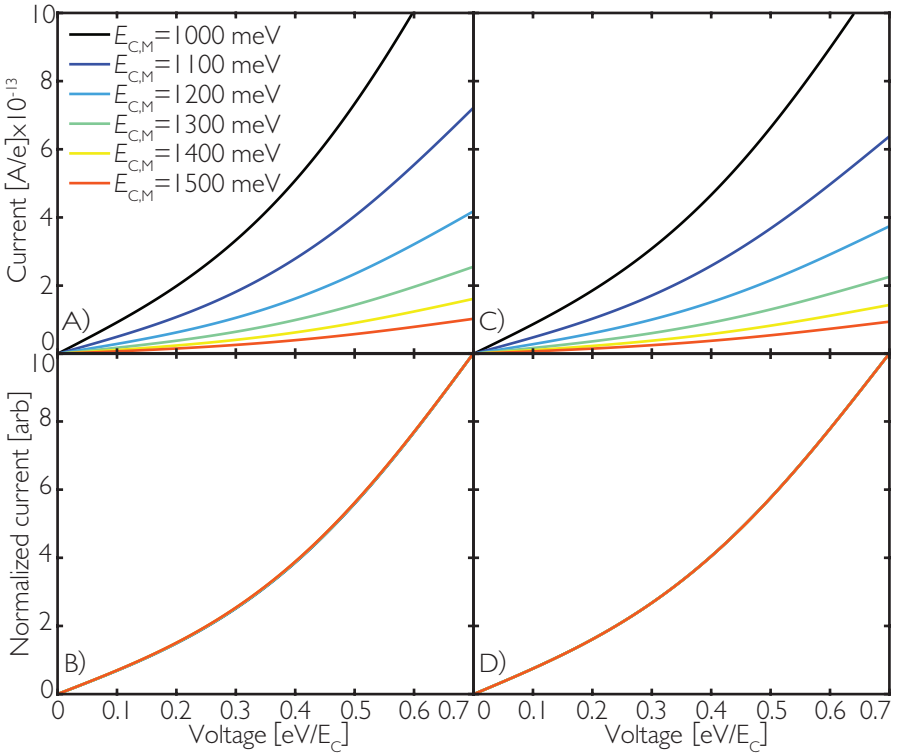

Fig. 3.6: IV curves for varying $E_{\mathrm{C,M}}$, calculated using Eq. 3.7. The temperature is set to 11.6 K, we take $E_{\mathrm{C}} = 100$ meV, and $E_{\mathrm{C,M}}$ is varied between 1 and 1.5 eV (see legend of A for the color coding, holding for all panels) **A**: IV-curves calculated. It can be seen that as $E_{\mathrm{C,M}}$ increases, the current decreases, as expected. **B**: Normalized IV-curves using the same parameters as in A, i.e. the current at $^{\mathrm{eV}}/_{E_{\mathrm{C}}} = 0.7$ has been set to unity for every curve. It can be seen that this normalization corrects for most of the differences due to variations in $E_{\mathrm{C,M}}$. However, it does not fully remove the variation between the curves. **C**: IV-curves calculated for varying $E_{\mathrm{C,M}}$, where all terms in the denominator other than the charging energies have been neglected. The result of this is that the sum over all virtual states is now a constant, independent of voltage. It can be seen that the total current is lower than in A. **D**: Normalized IV-curves using the same parameters as in C (normalization at $^{\mathrm{eV}}/_{E_{\mathrm{C}}} = 0.7$ again). Now the curves, calculated for different $E_{\mathrm{C,M}}$, lie exactly on top of one another.

3.5 Conclusion

We have explored two approaches to calculate inelastic cotunneling through a nanoparticle connected to two leads through molecules with energy-dependent transmission functions. In the first approach, the molecules are modeled as having single-level Lorentzian transmission functions. Interestingly, we find that at large applied bias, the current for systems with the molecular levels slightly off-resonant can be higher than for the case of resonant molecular levels. This remarkable behavior is a direct consequence of transport taking place via cotunneling. To test this prediction, a nanoparticle covered with molecules could be trapped in a nanogap using dielectrophoresis. Cotunneling transport in such a system is expected to deviate from results derived by Averin *et al.* [3]. In the second approach we model the molecules as Coulomb blockaded, so that transport across the molecules takes place through elastic cotunneling. We show that at low temperature and bias, the multiple cotunneling current should approach the expression for regular cotunneling. Our calculations support this by showing that the IV-curves are identical when normalized.

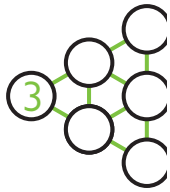

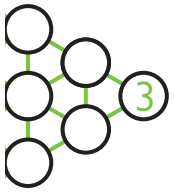

References

[1] T. Tran, I. Beloborodov, Jingshi Hu, X. Lin, T. Rosenbaum, and H. Jaeger. Sequential tunneling and inelastic cotunneling in nanoparticle arrays. *Physical Review B*, 78(7), 2008.

[2] J. F. Dayen, V. Faramarzi, M. Pauly, N. T. Kemp, M. Barbero, B. P. Pichon, H. Majjad, S. Begin-Colin, and B. Doudin. Nanotrench for nano and microparticle electrical interconnects. *Nanotechnology*, 21(33):335303, 2010.

[3] D. V. Averin and Yu V. Nazarov. Virtual electron diffusion during quantum tunneling of the electric charge. *Physics Review Letters*, 65(16):2446–2449, May 1990.

[4] T. Tran, I. Beloborodov, X. Lin, T. Bigioni, V. Vinokur, and H. Jaeger. Multiple cotunneling in large quantum dot arrays. *Physical Review Letters*, 95(7), August 2005.

[5] Jean-Francois Dayen, Edwin Devid, Mutta Venkata Kamalakar, Dmitry Golubev, Constant Guédon, Vina Faramarzi, Bernard Doudin, and Sense Jan van der Molen. Enhancing the Molecular Signature in Molecule-Nanoparticle Networks Via Inelastic Cotunneling. *Advanced Materials*, 25(3):400–404, jan 2013.

[6] A. E. Hanna, M. T. Tuominen, and M. Tinkham. Observation of Elastic Macroscopic Quantum Tunneling of the Charge Variable. *Physics Review Letters*, 68(21):3328, may 1992.

[7] L. J. Geerligs, D. V. Averin, and J. E. Mooij. Observation of macroscopic quantum tunneling through the coulomb energy barrier. *Physical review letters*, 65(24):3037, 1990.

[8] J.C. Cuevas and E. Scheer. *Molecular electronics, an introduction to theory and experiment*, volume 1. World Scientific Publishing Co., 2010. ISBN 981-4282-58-8.

[9] Paul A.M. Dirac. The quantum theory of the emission and absorption of radiation. *Royal Society London, Ser. A*, 114:243–265, 1927.

[10] R. Landauer. Spatial variation of currents and fields due to localized scatterers in metallic conduction. *IBM Journal of Research and Development*, 1(3):223–231, 1957.

[11] Sense Jan van der Molen, Jianhui Liao, Tibor Kudernac, Jon S. Agustsson, Laetitia Bernard, Michel Calame, Bart J. van Wees, Ben L. Feringa, and Christian Schönenberger. Light-controlled conductance switching of ordered Metal-Molecule-Metal devices. *Nano Letters*, 9(1):76–80, 2009.

[12] Colin Van Dyck, Victor Geskin, Auke J. Kronemeijer, Dago M. de Leeuw, and Jérôme Cornil. Impact of derivatization on electron transmission through dithienylethene-based photoswitches in molecular junctions. *Physical Chemistry Chemical Physics*, 15 (12):4392, 2013.

[13] Sanjeev Kumar, Seok-Hwang Yoon, and Gil-Ho Kim. Bridging the nanogap electrodes with gold nanoparticles using dielectrophoresis technique. *Current Applied Physics*, 9 (1):101 – 103, 2009.

[14] L. Bernard, M. Calame, S. J. van der Molen, J. Liao, and C. Schönenberger. Controlled formation of metallic nanowires via Au nanoparticle ac trapping. *Nanotechnology*, 18 (23):235202, June 2007.

[15] Bo Song, Dmitry A. Ryndyk, and Gianaurelio Cuniberti. Molecular junctions in the Coulomb blockade regime: Rectification and nesting. *Physical Review B*, 76(4), 2007.

[16] D. V. Averin and A. A. Odintsov. Macroscopic quantum tunneling of the electric charge in small tunnel junctions. *Physics Letters A*, 140(5), September 1989.

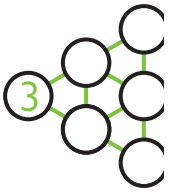

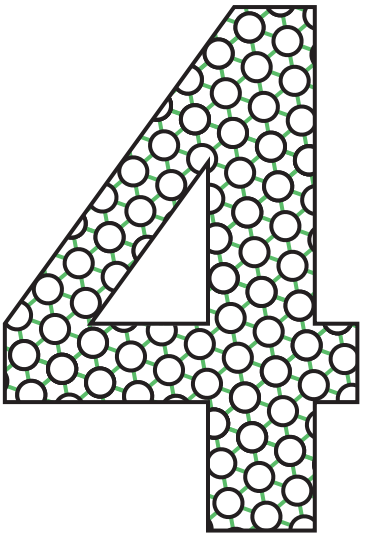

Experimental set-up and sample fabrication

The goal of this research is to study electron transport through nanoparticle networks at low temperatures. As explained in the past few chapters, current through a Coulomb blockaded network is expected to be dominated by (multiple) cotunneling. This type of transport depends strongly on the external conditions, mainly temperature and applied bias. Studying it involves measuring the rate of transport, and therefore electrical current, as a function of applied bias and temperature. This electrical current is small, down to fA and lower, as cotunneling is a higher order process.

In order to study cotunneling in nanoparticle networks, they need to be Coulomb blockaded, and hence cooled down to low temperatures. For a nanoparticle size of 10 nm, this temperature is below 100 K. Moreover, this temperature needs to be stable within a few percent, as the cotunneling current depends strongly on temperature.

This combination of low currents and low but stable temperatures requires specialized equipment. With this in mind, a new cryostat was installed as part of this research. In addition to the cryostat, a new low-current measurement set-up was built partly in-house, integrating with the electromagnetic shielding that the cryostat provides. This chapter describes this set-up and discusses sample fabrication.

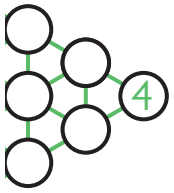

4.1 Cryostat

The cryostat used in this research is an Oxford Instruments Teslatron closed loop cryostat. It was installed as part of the research described in this thesis. The Teslatron enables conductance measurements at variable temperatures from 300 K down to 1.5 K. Furthermore, in contrast to a bath cryostat, its closed loop system requires no refilling of liquid helium and therefore enables continuous operation for months on end. A picture of the cryostat can be seen in Fig. 4.1. The outer casing is pumped to below 10^{-4} mbar to provide thermal insulation from the outside environment. Inside the cryostat are two sets of radiation shields to further separate the cryogenic temperature at the sample from the room temperature in the lab. The outer radiation shield is cooled down to between 40 K and 70 K, while the inside shield is cooled down even further to 4 K. The sample is positioned at the bottom of the cryostat using an insert. The insert provides electrical connections between the sample and the laboratory equipment, while additionally providing a thermocouple and heater element to control the sample temperature with 10 mK accuracy. The heart of the cryostat is a two stage pulse tube, the workings of which are explained in the appendix. It provides the cooling power necessary to investigate (amongst other things) cotunneling in nanoparticle networks. The sample itself is placed in the center of a superconducting magnet, enabling study in magnetic fields of up to 9 Tesla.

Fig. 4.1: Picture of the cryostat as installed. The rotary valve feeding the pulse tube can be seen on the top left, connected to two (one supply, one return) high pressure helium lines. The various lines in the top right are from right: insert vacuum line, helium circulation return (big line), helium circulation supply (small line).

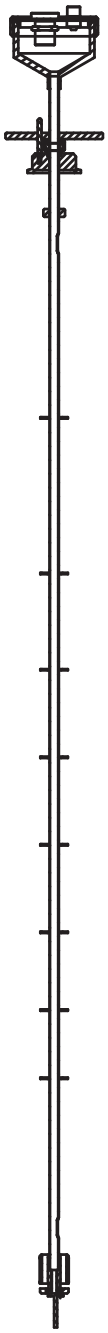

Fig. 4.2: Schematic of the insert as delivered by Oxford Instruments. After delivery, the wiring was replaced to reduce the noise floor. An alternative sample holder was fitted to enable illumination of the sample. Since the temperature sensor was originally fitted in the copper mass at the bottom, it was replaced by a sensor closer to the sample.

4.1.1 Remote operation and automation

The entire cryostat is controlled using a Mercury iTC (intelligent Temperature Controller), which has built-in algorithms to control the pressure at the needle valve, the temperature of the insert chamber, but also the temperature of the insert itself. Furthermore, the remote control capabilities allow full automation of the measurement procedure.

Automation software was written together with Isabelle Janssen[1]. The software was written in Python and can control the pressure and temperature and run a measurement script. As input, the software takes a configuration file, which contains a list of temperatures and measurement parameters. It then programmatically sets the setpoint temperature, waits for thermal stabilization and runs the measurement. Using a six-channel RF-switch*, up to six samples can be measured automatically at each temperature.

In order to increase the temperature settling speed at temperatures above 50 K, the needle valve is fully opened to allow optimal heat dissipation. Between 20 K and 50 K, the needle valve is closed halfway to decrease the heat load on the 4 K stage. Below 20 K, the needle valve is set to use pressure feedback to attain a pressure of 7 mbar, a value which was found to result in lowest sample temperature. A full cooldown to 1.6 K and warmup to room temperature cycle can take under 24 hours.

After temperature stability was reached, the chosen sample was connected automatically, and a LabVIEW script is called to perform the measurement. After the measurement, the program selects the next sample to measure, or set the next setpoint temperature after all samples are measured.

4.1.2 Insert

The cryostat cools down a small space at the bottom of the system. To measure a sample at these low temperatures, it needs to be thermally connected to the cold stage, while still being connected electrically to the measurement equipment. This is done by an insert; a long rod with connectors at the top, which electrically connect to the sample at the bottom, seen in Fig. 4.2.

To eliminate external interference in the current measurement, the insert was wired using low capacitance coaxial cables (85 pF m^{-1}, 170 μm core di-

* Radio Frequency switches are ideal for this application, as the leak resistance during open circuit is very large: >PΩ

ameter) by Bert Crama. At the bottom of the insert, the coaxial shields were soldered to the chassis of the sample holder, electrically connecting them. The wire cores were attached to individual connections on the sample holder, allowing the measurement of 12 devices simultaneously. The leak resistance was measured to be larger than a PΩ, which means that leakage currents have no significant effect on the measured signal, even at low temperatures and applied bias.

The cables added a significant amount of copper to the insert, and hence introduced a heat load on the sample. After wiring the insert, the base temperature increased by 100 mK to 1.6 K. Furthermore, the thermometer fitted by Oxford Instruments was positioned a few centimeters from the sample, introducing uncertainties in sample temperature. To correct this, a Lakeshore DT-670 silicon diode thermometer was fitted under the chip carrier, close to the sample. A picture of the insert can be seen in Fig. 4.3

In order to allow illumination of the sample, a 600 μm core diameter glass fiber was fitted inside the insert. The bottom of the fiber was open ended and fixed 2 cm above the sample, ensuring complete illumination.

Fig. 4.3: Picture of the low noise insert used in this research. The white coaxial cables go down to the sample through the copper mass containing the heater element. At the bottom, the shields are connected to the ground of the sample connector, and the wire cores are connected to individual pins. The optical fiber is the black wire sticking out. For the measurements, it was shortened and fixed above the sample, allowing illumination.

4.1.3 Chip carrier

In order to perform electrical measurements, the sample needs to be connected to the insert. This is done by a chip carrier. The carrier holds the sample and has electrical connecting pins that allow easy connection to the insert. Normally, the sample is connected to the carrier by wire bonds. However, making these bonds on the micrometer scale is tedious work, and can take hours per sample. Moreover, it requires a microscope and clear lighting to be feasible. As we shall see in chapter 6, some samples are sensitive to light, requiring wire bonds to be made in a darkened environment, vastly increasing the difficulty of this process. To ease the fabrication of electrical contacts to the on-chip devices to the carrier, we designed a two-piece carrier. The top piece (Fig. 4.4, right picture) holds eight spring contacts. Once connected to the bottom piece (Fig. 4.4 left picture), holding the sample, the spring contacts make an electrical connection to the contact pads which are lithographically defined on the sample.

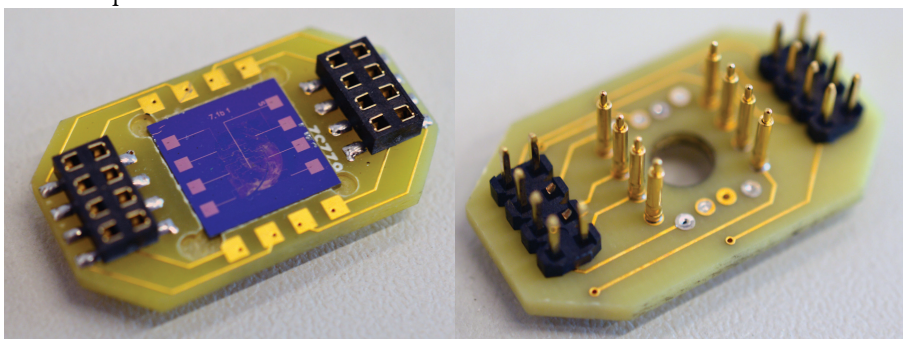

Fig. 4.4: Pictures of both sides of the chip carrier, left shows the bottom piece holding the sample, right shows the top piece with the spring contacts. The top is connected to the bottom part and the spring contacts facilitate the electrical connection between the sample and the carrier. The carrier is then connected to the insert.

4.2 Measurement electronics

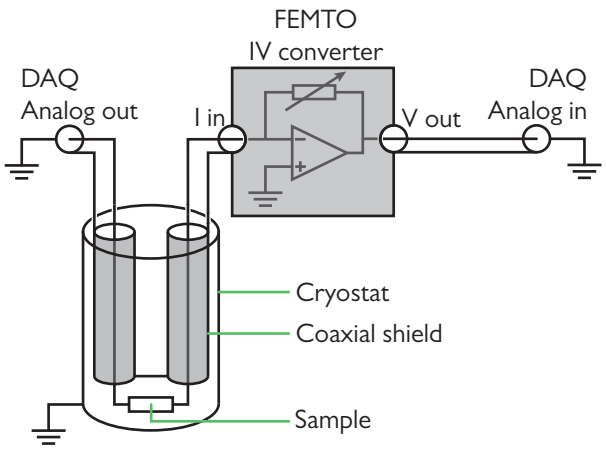

Fig. 4.5: Wiring schematic of a sample in the cryostat, attached to measurement electronics. A data acquisition (DAQ) card supplies a voltage to the sample, resulting in a current flowing through the sample. This current flows into the FEMTO IV converter, where it is converted to a voltage. This voltage is measured using an analog input on the same DAQ. The ground of the DAQ is connected to the shield of the coaxial voltage supply cable on the insert, which is connected to the shield of the current return line at the bottom of the insert. At the top, this shield is connected to the ground of the FEMTO, which is itself connected to the ground of the DAQ. The insert is floating inside the cryostat, and not electrically connected to it. The cryostat itself is separately grounded.

Once a sample is loaded in the cryostat, the insert is connected electrically to the measurement equipment as seen in Fig. 4.5. A NI USB 6341 DAQ (Data Acquisition card) is used to apply a bias on one end of the sample through a shielded cable. The shield of the DAQ analog out is connected to the shield of the cable. At the bottom of the insert, the shields of all cables are connected. The bias causes a current to flow, which is measured at the FEMTO DLCPA-200 IV converter. The FEMTO is connected to the insert by a doubly shielded cable, eliminating electromagnetic pick-up. In order to minimize noise introduced in the measurements, the sample is left electrically floating inside the cryostat, which means that the cryostat itself acts as a shield. The output of the FEMTO is connected to the analog input of the DAQ, which is grounded. In order to reduce high frequency noise, a 50 Hz low-pass filter can be connected between the output of the FEMTO and the input of the DAQ, but it is not depicted in the figure.

4.2.1 Improving noise floor

Inside the Coulomb blockade regime, the electrical current depends strongly on the applied bias. This means that in order to measure far into this regime, a very low noise floor is required. A lot of noise is suppressed by the wiring of the insert, discussed in the previous sections. However, a lower noise floor is gained by tuning the method of the current measure-

ment. The measurement is done in a two-point fashion, meaning that there is one output voltage and consequently a flowing current which is measured. In order to discern capacitive effects from resistive ones, the voltage is varied in a trace-retrace fashion. By varying the output voltage following a triangle wave (as seen in Fig. 4.6, left plot), multiple of these measurements are done in series. Typical frequencies vary between a few Hz and a few mHz. To anticipate the non-linear dependence of the current on voltage, the output voltage is evenly spaced on a log-scale, this means that the triangle wave only has a triangle shape on a logarithmic plot. After half a period, the voltage is inverted and the triangle wave is repeated, resulting in the plot shown.

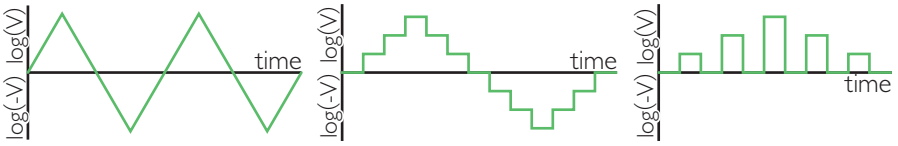

Fig. 4.6: DAQ output voltage versus time. The output voltages are evenly spaced logarithmically. Left: two trace-retrace voltage outputs in series The multiple trace-retrace measurements are averaged. Middle: zoom in on one trace-retrace output. From here, it can be seen that the trace-retrace measurement is actually a series of steps. Each step consists of a large number of individual measurements, depending on the duration of each step. Right: a zoom of the middle graph. A reference measurement at zero output voltage is taken after every measurement, allowing us to correct for drift or non-ideal behavior of the IV-converter.

The individual measurements however, are done in DC. To see why, consider Fig. 4.6, center plot. The output voltage is varied in steps at a fixed time interval. At each step, the DC current is measured at a rate of 500 000 samples per second[†]. The measured data is put through a digital low-pass filter with a cut-off frequency that is ten times larger than the voltage varying rate. This removes high frequency noise, while retaining a quick response necessary for the sharp voltage steps. The data is then averaged and saved. In order to correct for voltage drift (for example due to sample heater currents flowing down the insert next to the measurement wires), the voltage is set to zero after each measurement (see Fig. 4.6, right plot). The drift is subtracted from the signal, yielding the current.

[†] It is interesting to note here that since the noise floor of the system is 10 fA (as explained later), the amount of electrons flowing at these currents is around 50 000 s^{-1}. This means that on average, only one out of ten measurements includes the detection of an electron at these low currents. One might think that an electron multiplier instead of a commercially available DAQ would be more suitable for this research!

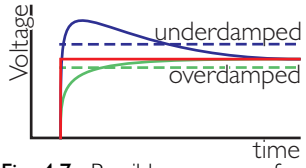

Fig. 4.7: Possible responses for an IV-converter (voltage versus time). Red is the ideal response. Blue is an underdamped response, resulting in a higher average measurement. Green is an overdamped response, giving a lower average measurement. The FEMTO DLCPA-200 gives an underdamped response.

Additional error is introduced by the FEMTO DLCPA-200 IV converter. It has a non-ideal response curve, which means that the output voltage of the FEMTO does not immediately settle to the correct value. This behaviour is schematically depicted in Fig. 4.7. The red line is the ideal response. Green is an overdamped case, which causes a lower average signal, seen as the dashed lines. Blue shows an underdamped case, resulting in a larger average signal. Especially at large amplification factors (10^9 V/A), the FEMTO shows an underdamped response, resulting in larger measured current than is actually flowing. This is corrected for in two ways. The first correction is a delay in the start of the current measurement. After setting a voltage over the sample, the FEMTO is given time to settle. The settling time is always one third of the voltage step duration. The settling of the FEMTO removes most of the overshoot, although it does not remove it completely.

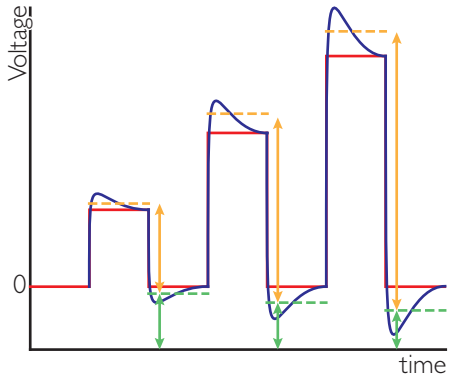

Fig. 4.8: Schematic voltage response of the FEMTO DLCPA-200 versus time time. Red is the ideal response. The FEMTO output has an offset due to a static input current. Blue is the measured voltage response of the FEMTO, which has an overshoot, causing a higher measured average (yellow arrows, average is yellow dashed lines). This overshoot increases with increasing input voltage, resulting from the reference measurement done after each step. However, since the same overshoot happens at the reference, the measured reference current (average in green dashed lines, arrows indicating magnitude) decreases with increasing voltage.

The second method is a correction done after the measurement. Consider the response curve shown in Fig. 4.8, which shows the response of the FEMTO as a function of time. The red curve shows the ideal response, the actual response is shown in blue. As can be seen in the curve, the reference signal is measured after each voltage step, as also seen in Fig. 4.6, right plot. The average of the reference measurement (dashed green line, green arrow) is subtracted from the signal (yellow dashed line) to obtain the recorded current, seen as the yellow arrow. However, due to the overshoot, this recorded current is larger than the true

current entering the FEMTO. More specifically, this overshoot is added twice, once due to the overshoot in the signal, and once due to the subtraction of the reference signal. This is supported by plotting the reference signal as a function of the set voltage before the reference measurement, seen in Fig. 4.9.

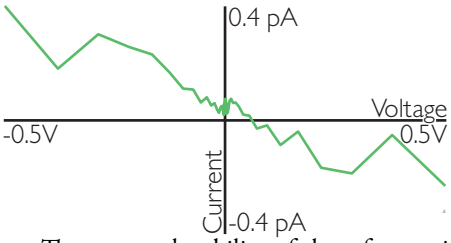

Fig. 4.9: Reference current (at zero volts) as a function of the voltage in the previous measurement. The line is the average taken over ten identical measurements. From the plot, it can be seen that the slope is negative, in agreement with Fig. 4.8, green arrows.

The temporal stability of the reference is important, since it allows us to extract the overshoot of the FEMTO exactly. As seen in Fig. 4.9, the reference signal is simply the sum of the overshoot and an arbitrary zero. This zero is in principle an adjustable parameter in the FEMTO IV-converter. In practice, however, it is easier to correct for this during data analysis, rather than correcting it manually before each measurement. Taking the mean of the drift current gives this zero, and subtracting it from the signal yields the overshoot. This overshoot is added twice[‡], yielding the current flowing through the device. Using these corrections in addition to large measurement times and doing repeated trace-retrace measurements, it is possible to achieve a noisefloor of under 10 fA, using 30 min averaging time per voltage step.

[‡] The overshoot extracted from the reference measurement has opposite sign, compared to the overshoot in the real signal, hence it is added and not subtracted.

4.3 Sample fabrication

Studying electron transport through networks of nanoparticles at low temperatures does not only require measurement apparatus, it also requires proper samples. Furthermore, these networks should somehow be connected to the equipment in order to be studied. This section first describes the fabrication of the devices used to connect the networks to the environment, and subsequently discusses the actual synthesis of the networks themselves.

4.3.1 Device fabrication

As was mentioned in the previous section, the current through Coulomb blockaded nanoparticle networks is very small. With this in mind, a device structure with a very large aspect ratio (length divided by width) was designed. A device like this measures many parts of the nanoparticle network in parallel, ideally increasing the total current, by four orders of magnitude in this case. A device like this would be very long, as with an aspect ratio of 10 000, a device width of 500 nm results in a length of 5 mm! These geometries are difficult to fabricate accurately using lithography (and also give problems with space on the sample), and hence the device was folded up to create the interdigitated structure shown in Fig. 4.10.

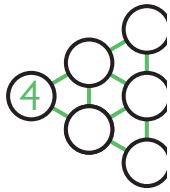

The contacts to the nanoparticle arrays were fabricated using electron beam lithography. First, a silicon wafer (P type doped with boron, 0.001 Ω m, 300 nm oxide) was diced to 1x1 cm chips. The chip is then spin coated with PMMA (polymethyl methacrylate, 950 kDa molecular weight, 4% weight in anisole) for 90 seconds at 4000 RPM to obtain a layer thickness of 250 nm. After spin coating, the chip is baked at 180 °C for 90 seconds. The baking flattens the PMMA layer and allows the anisole to evaporate.

Typically, six of these chips were simultaneously loaded in a Raith 100 EBPG electron beam lithography machine. In order to improve fabrication speed while maintaining high resolution, the patterning was done in two steps. First, small device patterns were written using a small spot size (140 nm), which functioned as the contacts to the nanoparticle networks. This was done for each loaded sample, while measuring the beam current in between samples in order to maintain the correct dose. Finally, large patterns were written using the largest available spot size (700 nm). These large patterns functioned as a connection between the measurement apparatus and the small devices on the chip. Again, the beam current was measured between each pattern, and corrections were done to the dwell time in order to maintain a constant dose. For all patterns, the acceleration voltage was kept at 30 kV. The dose was 270 $\mu C\,cm^{-2}$ for the small patterns and 300 $\mu C\,cm^{-2}$ for the large patterns[§]. Patterning was done programmatically and overnight using self-written scripts.

Development was done by submerging the chips in a 1:3 mixture of methyl isobutyl

[§]The small patterns are sensitive to the proximity effect and are given a smaller dose. This effect doesn't play an important role for the larger patterns, which hence have a larger dose. Since writing these large patterns takes much longer than writing the small patterns, this higher dose allows for fluctuations in the electron beam current.

ketone and isopropyl alcohol for 50 seconds at room temperature. The chip was then immediately transferred to pure isopropyl alcohol to stop development. The chip was removed from the solvent and blow-dried using a nitrogen gun.

After development, the chips were mounted on the sample rod of a resistance evaporator. This machine uses a high current (> 150A) to heat up chromium and gold in order to evaporate it. The chips were positioned upside down above the metals, and a 3.5 nm adhesion layer of chromium was evaporated, followed by 15 nm of gold. Deposition rate was monitored *in situ* using a quartz balance. The total thickness was chosen to be under 20 nm, to allow the network to adhere close to the contacts, as well as to the substrate itself.

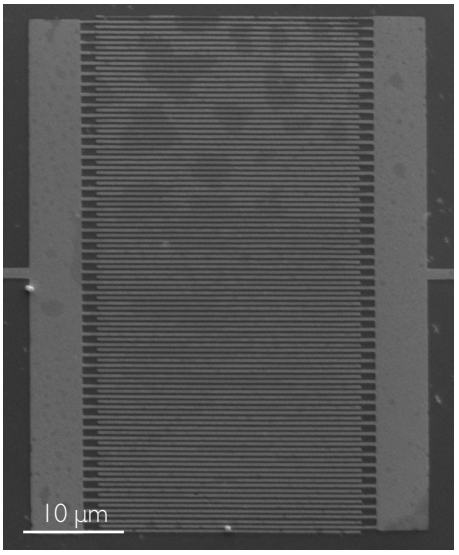

Fig. 4.10: Scanning electron microscopy image of a typical device structure. The device is in gold on Si/SiO_2 with 500 nm inter-electrode distance.

Lift-off was performed by submerging the chips in hot acetone (45 °C). After 30 minutes, the deposited metal around the edges had visibly loosened. A strong flow was created using a Pasteur pipette, which detached most of the metal from the surface. The chips were quickly transferred to a clean acetone solution and sonicated for 30 seconds to one minute. This last step removed the gold between the small gold electrodes. The chips were removed from the acetone while being sprayed with isopropyl alcohol to prevent evaporation of the acetone (evaporation of acetone leaves a visible organic layer) and subsequently blow-dried with nitrogen, yielding clean device structures as shown in Fig. 4.10.

4.3.2 Nanoparticle synthesis

The second step of sample fabrication is of course the synthesis of the nanoparticle networks themselves. The networks as well as the 10 nm nanoparticles (particles smaller than 10 nm were purchased at Sigma Aldrich) were synthesized in-house.

10 nm diameter gold nanoparticles were synthesized using the aqueous chemical reduction of chlorauric acid following a synthesis method pioneered by Turkevich[2] and later refined by Frens *et al.*[3] and Slot *et al.*[4]. Slot *et al.* used two competing reducing agents (trisodium citrate and tannic acid), where the growth is initially seeded by both reducing agents, but the growth itself is controlled exclusively by trisodium citrate[5]. Briefly: 10 mg of $HAuCl_4 \cdot 3H_2O$ (Aldrich) was dissolved in 100 mL demiwater (18 MΩ cm, Millipore)

and heated to 60 °C to which 40 mg of trisodium citrate (Aldrich) and 800 µg of tannic acid (Aldrich) were added under vigorous stirring as reducing agents. After two minutes, the solution had turned dark red and was heated to a boil under reflux while stirring vigorously. After ten minutes, the solution had turned ruby red and was cooled to room temperature. The nanoparticles were separated from the solvent by centrifugation (10 °C, 15000 RPM, 60 min) and the supernate was removed. The nanoparticles were redispersed in absolute ethanol (Aldrich) and 100 µL of the desired alkanethiol was added. The resulting solution was stored in the fridge to precipitate over the course of one to three days. The supernate was removed and the nanoparticles were redispersed in 0.4 ml of chloroform (Aldrich) for every ml of supernate removed. The nanoparticle size was checked under a scanning electron microscope.

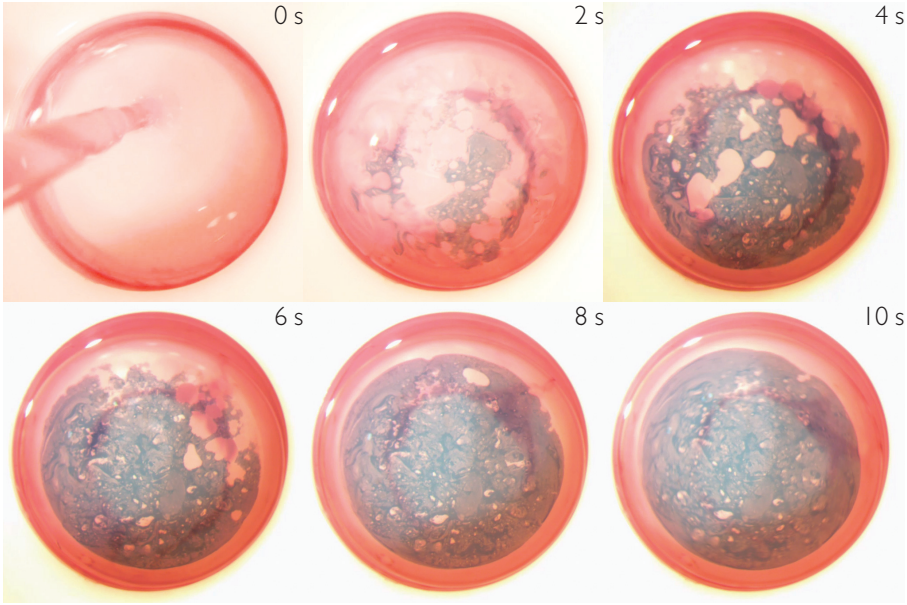

Fig. 4.11: Optical images of a nanoparticle array forming on a water surface in a PTFE cup. Top left is the first image and bottom right is the final image. Top left: a solution of alkanethiol capped gold nanoparticles in chloroform is pipetted onto a convex water surface. Top center: the chloroform starts to evaporate and a array quickly forms. Top right: the array grows quickly from the edges outwards. Bottom left: the array starts filling the PTFE cup, and further growth on the edges compresses the array. Bottom center: holes in the array are closed due to compression. Bottom right: the array finished growing and almost completely covers the water surface.

For nanoparticle array fabrication, a 50 µL of gold nanoparticle solution in chloroform

was added to the convex water surface in a PTFE beaker. After evaporation of the solvent, a gold nanoparticle array can be seen floating on the surface (this process is shown in Fig. 4.11). Transfer to lithographically defined devices (500 nm interelectrode spacing, 5 mm device length, Fig. 4.10, discussed in the previous section) on a diced silicon wafer (300 nm oxide) was done by a PDMS stamp. The stamp was cut to a small size, allowing full coverage of all devices, but not covering much more of the sample, allowing comparison to a bare reference device, which should not allow a current to flow. The stamp was slowly lowered to the surface of the water, allowing it to touch. After a few seconds of contact (this time did not seem to be crucial), the stamp was quickly removed from the water surface, possibly leaving water droplets on the stamp. The stamp was blow-dried with nitrogen, after which the nanoparticle array can be seen on the stamp. It was subsequently lowered onto the substrate using tweezers, and light pressure was applied by hand. The stamp was removed, leaving the array stuck to the substrate. An optical image of such a sample, including a SEM image can be seen in Fig. 4.12.

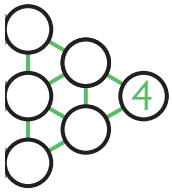

Preliminary characterization of the arrays was done by measuring the room temperature two-probe resistance of all the devices on the sample. This allowed us to eliminate devices where the lift-off was unsuccessful, resulting in a shorted device, or devices where the nanoparticle array did not attach and left an open circuit.

Other methods of nanoparticle synthesis and array fabrication were attempted, such as the method proposed by Martin *et al.* [6], as this would provide easy means to synthesize smaller nanoparticle but also improve array quality. Although the nanoparticle synthesis itself looked successful by eye, SEM inspection could not give clear insights on this, as the resolution of the SEM was not good enough. The array synthesis using these nanoparticles was unsuccessful, as deposition of the solution of nanoparticles in hexane on the toluene droplet simply caused the droplet to disperse, instead of leaving it covered with the nanoparticle solution. An alternative was tried, where instead of nanoparticles in hexane, we used nanoparticles dissolved in chloroform. This however gave the same result as the hexane solution.

An alternative to the array formation on the water surface in a teflon cup, is a droplet-drying method proposed by Lin *et al.* [7], which results in extremely long-range-ordered nanoparticle arrays, with single-crystalline domains of over a few micrometers.

This method was tried with 10 nm nanoparticles on SiO_2 as well as on teflon using both toluene and chloroform as a solvent. However, even tuning the volume fraction of excess thiol in the solution between 10^{-4} and 10^{-2} did not show the formation of ordered arrays, but instead showed a coffee-stain-like effect.

After the arrays have been fabricated, they can be interconnected by the molecule of interest using molecular place-exchange, creating a network. The sample is put into a solution (usually a concentration of roughly 1mM, but can vary by an order of magnitude) of the molecule overnight (the time depends on the concentration and commonly varies between one and 24 hours). During this time, the alkane thiols can de-attach from the nanoparticles,

allowing the molecule to bind to the nanoparticle by a sulfur bond. In the case of dithiols, the other end of the molecule can bind chemically to the other nanoparticle. After place exchange, the resistance of the device has usually dropped by a few orders of magnitude, depending on the alkanethiol and the exchanged molecule, as already seen in Fig. 2.9.

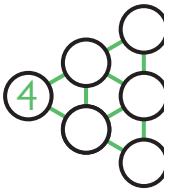

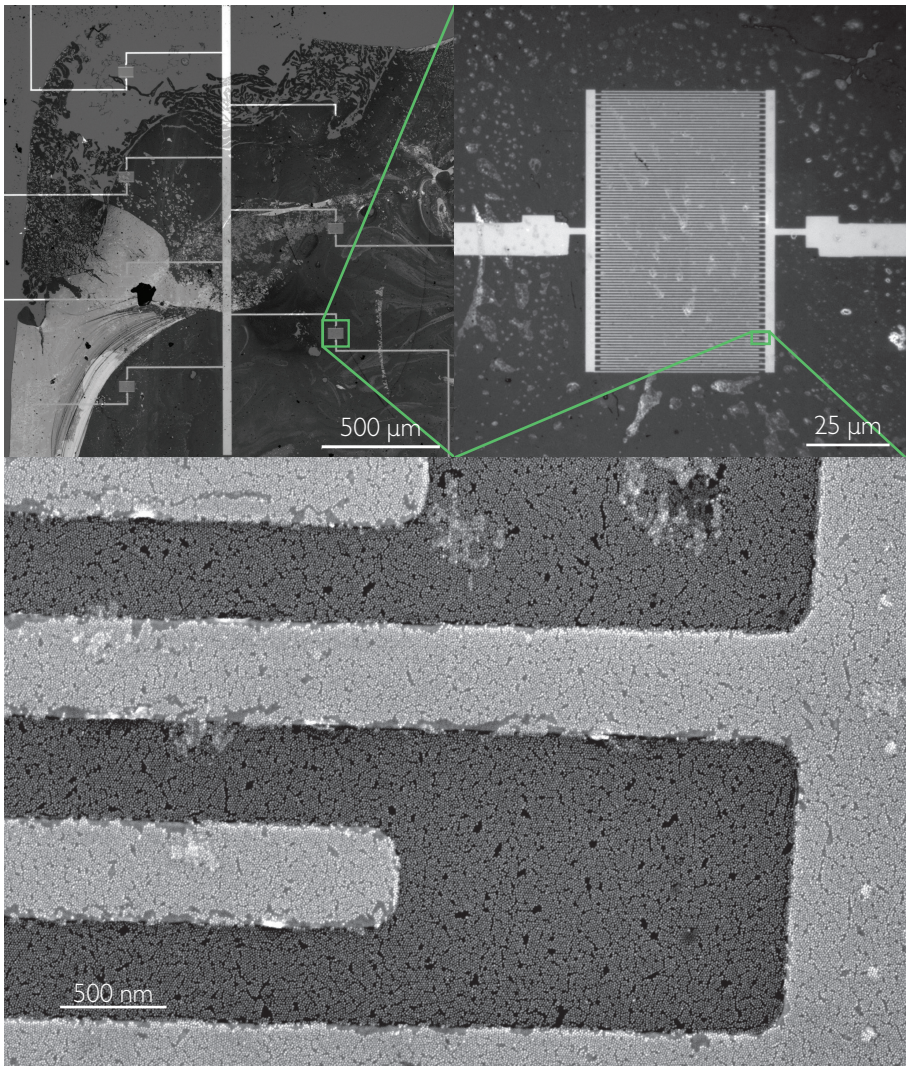

Fig. 4.12: Images of a sample containing devices with a gold nanoparticle array stamped on top. Top two images are obtained using an optical microscope, bottom image is a SEM picture. These images nicely illustrate the different length scales involved; from the large structures on the top left, just visible to the naked eye, to the meandering device structure, just barely resolved by visible light, to the array of tiny nanoparticles between the electrodes. The top left image shows the large device structure of the gold contact lines connecting to the devices seen on the top right. The bottom image shows that multiple crystal domains of the array are present between the gold contacts.

References

[1] Isabelle Heukensfeldt Jansen. Analyzing multiple cotunneling distance for gold nanoparticle arrays at cryogenic temperatures. Master's thesis, Leiden University, 2016.

[2] John Turkevich, Peter Cooper Stevenson, and James Hillier. A study of the nucleation and growth processes in the synthesis of colloidal gold. *Discussions of the Faraday Society*, 11:55–75, 1951.

[3] G. Frens. Controlled nucleation for the regulation of the particle size in monodisperse gold suspensions. *Nature Physical Science*, 241:20, 1973.

[4] J. W. Slot and Hans J. Geuze. A new method of preparing gold probes for multiple-labeling cytochemistry. *European Journal for Cell Biology*, 38(1):87–93, 1985.

[5] Jordi Piella, Neus G. Bastús, and Victor Puntes. Size-Controlled Synthesis of Sub-10-nanometer Citrate-Stabilized Gold Nanoparticles and Related Optical Properties. *Chemistry of Materials*, 28(4):1066–1075, 2016.

[6] Matthew N. Martin, James I. Basham, Paul Chando, and Sang-Kee Eah. Charged Gold Nanoparticles in Non-Polar Solvents: 10-min Synthesis and 2d Self-Assembly. *Langmuir*, 26(10):7410–7417, 2010.

[7] X. M. Lin, H. M. Jaeger, C. M. Sorensen, and K. J. Klabunde. Formation of Long-Range-Ordered Nanocrystal Superlattices on Silicon Nitride Substrates. *The Journal of Physical Chemistry B*, 105(17):3353–3357, 2001.

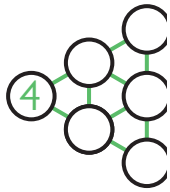

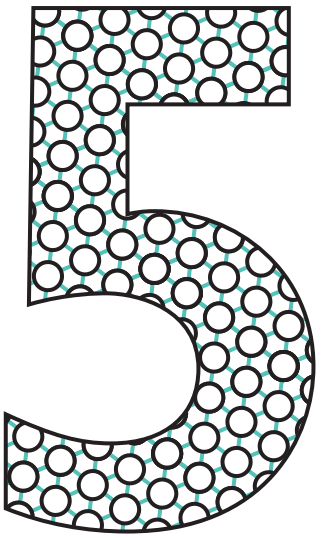

Studying electron transport through nanoparticle arrays

5.1 Introduction

As discussed in the previous chapters, at cryogenic temperatures, electronic transport through gold nanoparticle networks is expected to be facilitated by cotunneling[1–7]. This is interesting because this enhances the network sensitivity to the interlinking molecular bridges[2]. This chapter will experimentally verify this prediction and thereby lay the foundation for further experiments on networks interlinked by molecular switches. Before we can discuss this, it is worthwhile to further discuss multiple cotunneling.

5.2 Theory of multiple cotunneling

5.2.1 The Arrhenius model

Multiple cotunneling was already discussed in chapter 2. However, it is worthwhile to discuss it in more detail here. The model developed by Tran *et al.*[3], describes the cotunneling current as:

$$I \propto V_{\text{jct}} G_0 \sum_j \left(\frac{G_\mathcal{T}}{G_0}\right)^j \left[\frac{(eV)^2 + (2\pi k_\text{B} T)^2}{E_\text{C}^2}\right]^{j-1} \exp\left(\frac{jeV_{\text{jct}} - {}^{E_\text{C}}/_j}{k_\text{B} T}\right), \quad (5.1)$$

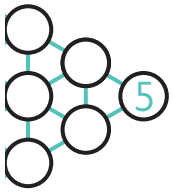

which is Eq. 2.8, and from now on called the Arrhenius Model, referring to the exponential Arrhenius term. This equation consists of two parts. The first one describes the cotunneling probability $\mathcal{P}_j$ (j indicating the cotunneling length) and is given by:

$$\mathcal{P}_j = \left(\frac{G_\mathcal{T}}{G_0}\right)^j \left[\frac{(eV)^2 + (2\pi k_\text{B} T)^2}{E_\text{C}^2}\right]^{j-1}. \quad (5.2)$$

This makes intuitive sense, since the first part containing $G_\mathcal{T}$ is the barrier transmission probability raised to the j^{th} power, taking into account the j barriers that need crossing. The second part comes from the cotunneling through the charging island, and is raised to the $(j-1)^{\text{th}}$ power, since there are $j-1$ charging islands that need to be crossed. This part decreases with increasing j, as both the transmission probability and the cotunneling probability are smaller than one.

The second part of Eq. 5.1 describes the number of electrons available for transport $\mathcal{N}$, and is given by:

$$\mathcal{N}_j = V_{\text{jct}} \exp\left(\frac{jeV_{\text{jct}} - {}^{E_\text{C}}/_j}{k_\text{B} T}\right). \quad (5.3)$$

Here, V_{jct} is the width of the bias window per junction, giving the number of electrons that have sufficient electrostatic energy to contribute to the current. The Arrhenius-like exponent should describe the number of electrons with enough thermal energy to initiate a cotunneling event of order j. This Arrhenius exponent is used in chemistry to describe the

rates of chemical reactions with an activation energy as a function of temperature. In this context, the activation energy is taken to be $^{E_C}/_j - jeV_{jct}$, which is the energy needed to take an electron from one charging island and put it on the j^{th} next charging island, assuming that the charging energy depends inversely proportional on the distance from the first island. This part increases with increasing j, as the energy barrier in the exponent decreases as j increases.

The interesting part of the Arrhenius model is that it predicts that there is an optimal cotunneling distance j_{opt} at which most of the current flows. To obtain this, it is assumed that j is a continuous variable, and the derivative of the current (Eq. 2.8) to j is taken, set to zero and solved for j [2]. This j_{opt} depends on temperature and voltage, increasing with decreasing voltage and temperature. Since the cotunneling current itself depends on $G_{\mathcal{T}}^{j_{opt}}$, changing $G_{\mathcal{T}}$ slightly at large j_{opt}, drastically changes the current. Observing this effect is the original motivation of the research discussed in this thesis.

Furthermore, the model describes three different regimes, as already discussed in chapter 2 [2]. A linear regime at low bias, where the thermal energy is larger than the electrostatic energy ($k_BT > eV_{jct}$), an intermediate nonlinear regime at intermediate bias, where the electrostatic energy is larger than the thermal energy but smaller than the thermal energy times the log of one over the transmission probability ($k_BT < eV_{jct} < k_BT\log(G_0R_{\mathcal{T}})$), and an exponential regime where the electrostatic energy is larger than the thermal energy times the log of one over the transmission probability ($eV_{jct} > k_BT\log(G_0R_{\mathcal{T}})$). This was further discussed in chapter 2. At even larger bias where $eV_{jct} > {}^{E_C}/_j$, the model diverges due to the growing Arrhenius term. This is unphysical, as this term is only valid when the activation energy is larger than zero. At these large biases, the electron transport mechanism transitions from cotunneling to sequential hopping, and the IV curve should be linear again.

In the intermediate nonlinear regime, the current depends on the bias to the power α, where $\alpha = 2j_{opt} - 1$. This interesting property means that the cotunneling distance can be obtained simply by determining the slope of the IV curve on a double log scale. This provides a good method to test this model, as j_{opt} can be extracted both from the slope as from the resistance ratio in a switching experiment where $G_{\mathcal{T}}$ is changed by using a molecular switch.

The model qualitatively describes the linear IV curves observed in experiments at low bias [1–4], and also the power-law curves at higher bias. At very large bias, however, the divergence in the model prevents any fitting, as the system is no longer Coulomb blockaded. Furthermore, the ad-hoc Arrhenius term is questionable, as there is no real energy barrier that needs to be overcome, other than the Coulomb barrier already taken into account by $\mathcal{P}$ in Eq. 5.2. Furthermore, the model assumes that the Coulomb charging energy *decreases* with increasing cotunneling distance, yielding the $^{E_C}/_j$ term. This term is necessary in order to predict a j_{opt} (without the j in the denominator there is no predicted j_{opt}). This is questionable, since in a vacuum, the energy of two opposing charges *increases* with the separation of those charges. In a network, such a distance dependence may be decreased, due

to shielding of the charge, making it constant and independent of j_{opt}. To improve on these issues, we propose an alternative model.

5.3 The alternative model

Solving multiple cotunneling exactly is a problem that greatly increases in difficulty with increasing cotunneling distance. Inelastic cotunneling derived by Nazarov *et al.* [8] involves solving a four-dimensional integral over all four electron energies present in the system (see Chapter 3), in order to predict the cotunneling current with $j = 2$. Every further cotunneling step adds two more electron energies to integrate over, greatly increasing the difficulty of solving it. Moreover, the number of pathways scales with $j!$, which diverges quickly for increasing j. It therefore makes sense to circumvent this method and use an ad-hoc approach as previously in the Arrhenius model. Although that model describes the transmission probability $\mathcal{P}$ intuitively, the number of available electrons $\mathcal{N}$ is approximated in a poorly justified way. Both terms diverge at large bias where $eV_{\text{jct}} > E_{\text{C}}$. In this section we will introduce a different model which tries to more accurately capture the physics.

5.3.1 Determining $\mathcal{N}$

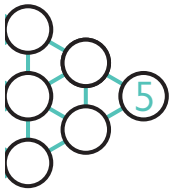

Quantum transport is usually calculated using the Landauer-Buttiker formalism [9]. It describes a system with two electron reservoirs (or leads) bridged by a barrier with a transmission probability which is dependent on electron energy. When a bias is applied to each reservoir (V_{L} for the left and V_{R} for the right one), the current is given by:

$$I = G_0 \int_{-\infty}^{+\infty} \mathcal{T}(E) \Big\{ f(E - eV_{\text{L}}) \left[1 - f(E + eV_{\text{R}})\right] - f(E + eV_{\text{R}}) \left[1 - f(E - eV_{\text{L}})\right] \Big\} \mathrm{d}E, \quad (5.4)$$

where

$$f(E) \equiv \frac{1}{e^{E/k_{\text{B}}T} + 1} \quad (5.5)$$

is the Fermi function, assuming $E_{\text{F}} = 0$. Eq. 5.4 describes that each electron on the left lead tries to find an unoccupied state on the right, and vice versa. At zero bias, these two currents are equal and cancel, but upon applying a bias, more electrons are available on one side, resulting in a net current to the other.

To extend this formula to nanoparticle networks in the Coulomb blockade regime, the Coulomb charging energy needs to be taken into account. Here, not every available electron has enough energy to occupy an available state, as occupying that state would cause the nanoparticle to charge, requiring the Coulomb charging energy E_{C}. This means that in the absence of an applied bias, an electron on the left lead needs to have an energy of E_{C} or larger

in order to facilitate transport to any nanoparticle. When a bias is applied across the leads, a potential drops across the network, lowering the energy required to charge a nanoparticle. Furthermore, this energy decreases with increasing distance, as can be more clearly seen in Fig. 5.1.

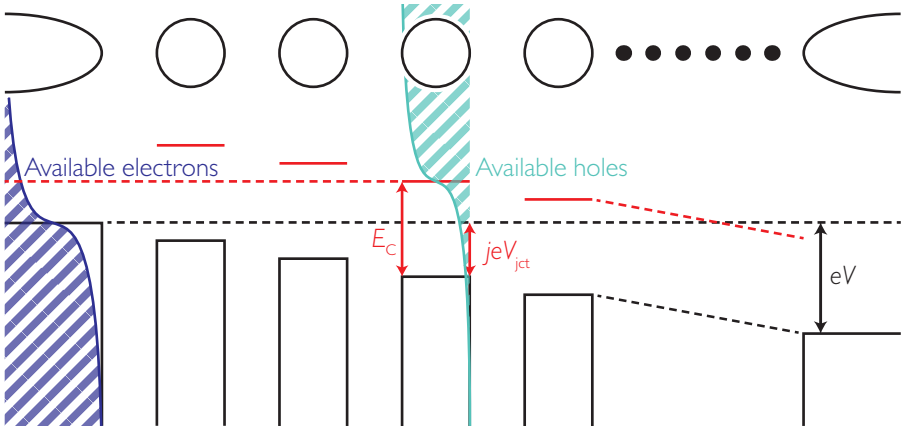

Fig. 5.1: Energy diagram of a chain of nanoparticles coupled to two leads. Due to a finite temperature, the Fermi function broadens and the electrons above the energy $E_C - jeV_{jct}$ have a chance to hop to the available states on the j^{th} nanoparticle. The thermally excited hole states below the Fermi level on the nanoparticle additionally allow electrons below the energy $E_C - jeV_{jct}$ to contribute to transport.

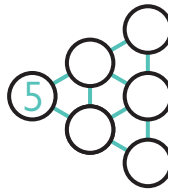

In this diagram, the electrons marked in blue are available and can contribute to the transport process. The area marked in green denotes the available states for the electrons marked in blue. The number of electrons contributing to the forward current is then a multiplication of the available electrons and the available states, integrated over all energies:

$$\mathcal{N}_{j,\rightarrow} = \int_{-\infty}^{+\infty} f(E)\left[1 - f(E - E_C - jeV_{jct})\right] \mathrm{d}E. \tag{5.6}$$

It is assumed here that the left lead is grounded. Analogously, the number of electrons contributing to the reverse current is given by:

$$\mathcal{N}_{j,\leftarrow} = \int_{-\infty}^{+\infty} f(E - E_C + jeV_{jct})\left[1 - f(E)\right] \mathrm{d}E. \tag{5.7}$$

This reverse process involves taking an electron off of the j^{th} nanoparticle and putting it on the left lead, a process requiring an energy of $E_C + jeV_{jct}$. The total number of electrons

contributing to the process is given by the forward current minus the reverse current:

$$\mathcal{N}_j = \mathcal{N}_{j,\rightarrow} - \mathcal{N}_{j,\leftarrow}. \tag{5.8}$$

Solving the integral gives:

$$\mathcal{N}_j = -\frac{E_\mathrm{C} - jeV_\mathrm{jct}}{1 - \exp\left(\left(E_\mathrm{C} - jeV_\mathrm{jct}\right)/k_\mathrm{B}T\right)} + \frac{E_\mathrm{C} + jeV_\mathrm{jct}}{1 - \exp\left(\left(E_\mathrm{C} + jeV_\mathrm{jct}\right)/k_\mathrm{B}T\right)}. \tag{5.9}$$

The first term is the forward current, the second is the reverse. This equation differs from Eq. 5.3 in a few ways. Firstly, at high temperatures ($k_\mathrm{B}T \gg E_\mathrm{C}$), $\mathcal{N}$ scales linearly with jeV_jct. This is different from Eq. 5.3, where it only scales with V_jct. This stems from the fact that the bias window scales with jeV_jct, as the potential drop (and hence the bias window) increases with increasing j. Secondly, it does not diverge at large bias or cotunneling length, in contrast to Eq. 5.3. Note that this term has also been used in other models that mainly deal with disorder in nanoparticle networks[10,11].

5.3.2 Determining $\mathcal{P}$

Although the probability derived in Eq. 5.2 is very accurate at low bias, it diverges at large bias where $E_\mathrm{C} \approx eV_\mathrm{jct}$. This divergence stems from Eq. 2.7, which is derived assuming that $eV_\mathrm{jct} \ll E_\mathrm{C}$. When $E_\mathrm{C} \approx eV_\mathrm{jct}$, Eq. 2.7 does not accurately describe the behavior anymore. Since $\mathcal{P}_j$ is never allowed to be larger than unity, the divergence can be solved in an *ad hoc* fashion by taking the arctangent of the term:

$$\mathcal{P}_j = \left(\frac{G_\mathcal{T}}{G_0}\right)^j \frac{2}{\pi} \arctan\left(\frac{\pi}{2}\frac{(eV)^2 + (2\pi k_\mathrm{B}T)^2}{E_\mathrm{C}^2}\right)^{j-1}. \tag{5.10}$$

This ensures that the transmission probability does not become larger than one at large applied bias or temperature. This is important, since in large nanoparticle networks and a total applied bias $eV > E_\mathrm{C}$, there is always a cotunneling distance such that $E_\mathrm{C} \approx jeV_\mathrm{jct}$. Additionally, the E_C in the denominator originates from the difference in energy between the initial and virtual states involved in the cotunneling process. Although this reduces to E_C at small applied bias, at large bias, the denominator can be replaced by $E_\mathrm{C} - eV_\mathrm{jct}$, which takes into account the shift in E_C with applied bias.

Expanding this for multiple cotunneling is slightly more involved. Considering the system depicted in Fig. 5.2; for the j^th nanoparticle, the charging energy is reduced by jeV_jct. However, the process also involves transport through the previous nanoparticles, which have a different charging energy. For example: a cotunneling event with $j = 3$ (note that Fig. 5.2 shows an event with $j = 5$) involves transport through the first two nanoparticles with effective charging energies of $E_\mathrm{C} - eV_\mathrm{jct}$ for the first, $E_\mathrm{C} - 2eV_\mathrm{jct}$, finally settling on the third nanoparticle. The third nanoparticle is the final state, therefore a multiple cotunneling event with $j = 3$ requires two cotunneling events and three barrier transmissions. This probability can be written as the product of all intermediate cotunneling probabilities:

$$\mathcal{P}_{j=3} = \left(\frac{G_\mathcal{T}}{G_0}\right)^3 \left(\frac{2}{\pi}\right)^2 \arctan\left(\frac{\pi}{2}\frac{(eV)^2 + (2\pi k_\mathrm{B}T)^2}{(E_\mathrm{C} - eV_\mathrm{jct})^2}\right) \times \arctan\left(\frac{\pi}{2}\frac{(eV)^2 + (2\pi k_\mathrm{B}T)^2}{(E_\mathrm{C} - 2eV_\mathrm{jct})^2}\right). \quad (5.11)$$

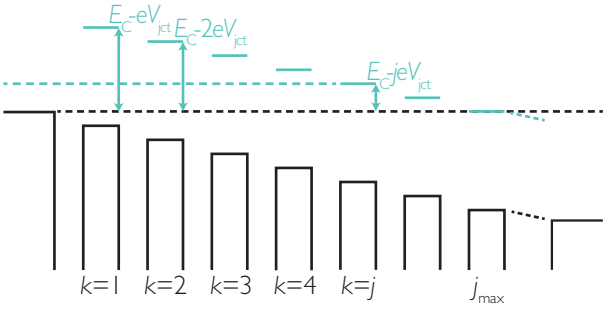

Fig. 5.2: Energy diagram of a cotunneling event with order $j = 5$ nanoparticle chain coupled to two leads. This event consists of five virtual electron transfers, each experiencing a different charging energy $E_\mathrm{C} - keV_\mathrm{jct}$. The maximum cotunneling length j_max is depicted here as the last shown nanoparticle.

Expanding this for any value of j gives:

$$\mathcal{P}_j = \left(\frac{G_\mathcal{T}}{G_0}\right)^j \prod_{k=1}^{j-1} \frac{2}{\pi} \arctan\left(\frac{\pi}{2}\frac{(eV)^2 + (2\pi k_\mathrm{B}T)^2}{\left(E_\mathrm{C} - keV_\mathrm{jct}\right)^2}\right). \quad (5.12)$$

The product series starts at $k = 1$ when $j = 2$, as $j = 1$ does not involve cotunneling, but is instead one sequential tunneling event. This probability decreases with increasing j in two ways. First, the transmission probability $(G_\mathcal{T}/G_0)$ is smaller than one and $\mathcal{P}_j$ therefore decreases exponentially with increasing j. Second: the second term also decreases with increasing j, but only up to a certain maximum j_max. When $jeV_\mathrm{jct} \geq E_\mathrm{C}$, the product series starts taking into account terms where the denominator goes to zero. These terms approach unity, and do not decrease the product any further. The total probability however, still decreases even when $j > j_\mathrm{max}$, as $(G_\mathcal{T}/G_0)^j$ still decreases with increasing j. This means that the transmission probability in Eq. 5.12 is always larger than the one calculated with the Arrhenius model, seen in Eq. 5.2.

5.3.3 THE FULL EQUATION

Now that both terms are discussed individually, the total multiple cotunneling current can be discussed. Combining the terms in Eq. 5.12 and Eq. 5.9 and summing over all cotunnel-

ing lengths gives:*

$$I \propto \frac{G_0}{e} \sum_j \left(\frac{G_\mathcal{T}}{G_0}\right)^j \prod_{k=1}^{j-1} \left\{ \frac{2}{\pi} \arctan\left(\frac{\pi}{2} \frac{(eV)^2 + (2\pi k_\mathrm{B}T)^2}{\left(E_\mathrm{C} - keV_\mathrm{jct}\right)^2} \right) \right\} \times \left[\frac{E_\mathrm{C} + jeV_\mathrm{jct}}{1 - \exp(^{(E_\mathrm{C} + jeV_\mathrm{jct})}/_{k_\mathrm{B}T})} - \frac{E_\mathrm{C} - jeV_\mathrm{jct}}{1 - \exp(^{(E_\mathrm{C} - jeV_\mathrm{jct})}/_{k_\mathrm{B}T})} \right]. \quad (5.13)$$

The first line describes the tunneling probability $\mathcal{P}$, whereas the second line describes the number of available electrons $\mathcal{N}$.

5.4 Consequences of the new model

Since $\mathcal{N}$ increases with increasing j, but $\mathcal{P}$ instead decreases, it is interesting to see what Eq. 5.13 predicts. Using MATLAB we now calculate the current versus voltage for various temperatures, using $^{G_\mathcal{T}}/_{G_0} = 0.1$ and $E_\mathrm{C} = 25$ meV. Since we cannot sum over an infinite amount of cotunneling lengths, we set $j_\mathrm{max} = 50$. Additionally, we determine j_mean, which is the current averaged cotunneling distance (and hence a continuous variable) given by:

$$j_\mathrm{mean} \equiv \frac{\sum_j j I_j}{\sum_j I_j}. \quad (5.14)$$

Here, I_j is the current per cotunneling length. The result can be seen in Fig. 5.3. An important feature is that the current does not diverge at large bias (in contrast to the Arrhenius model), due to the corrections to $\mathcal{P}$ and $\mathcal{N}$. Additionally, from this diagram, it can be seen that the shape of the IV-curve can be described as a combination of three regimes, similar to the Arrhenius model. Analogously, we call these regimes CI, CII and CIII, described as:

$$\text{CI}: \quad eV_\mathrm{jct} < k_\mathrm{B}T \quad (5.15)$$

$$\text{CII}: \quad k_\mathrm{B}T < eV_\mathrm{jct} < E_\mathrm{C} \quad (5.16)$$

$$\text{CIII}: \quad eV_\mathrm{jct} > E_\mathrm{C}. \quad (5.17)$$

In CI, the electrostatic potential difference per junction is smaller than the thermal energy ($eV_\mathrm{jct} < k_\mathrm{B}T$) and the IV-curve is linear. In CIII, the electrostatic energy per junction is larger than the Coulomb charging energy ($eV_\mathrm{jct} > E_\mathrm{C}$) and the IV-curve is also linear. The CII regime is interesting, since the electrostatic energy per junction is between the thermal

*The electron charge in the denominator comes from the last term, which has dimensions of energy. Dividing by the electron charge gives a voltage, which times G_0 has units of current. All other terms are dimensionless.

energy and Coulomb charging energy ($k_BT < eV_{jct} < E_C$) and the IV-curve is nonlinear. This is only possible when the system is cooled down such that $E_C \gg k_BT$. As the temperature decreases, the domain of the CII regime increases. At high temperatures where $E_C \ll k_BT$, the IV-curve is linear everywhere, as the thermal energy of the electrons is enough to overcome the Coulomb barrier.

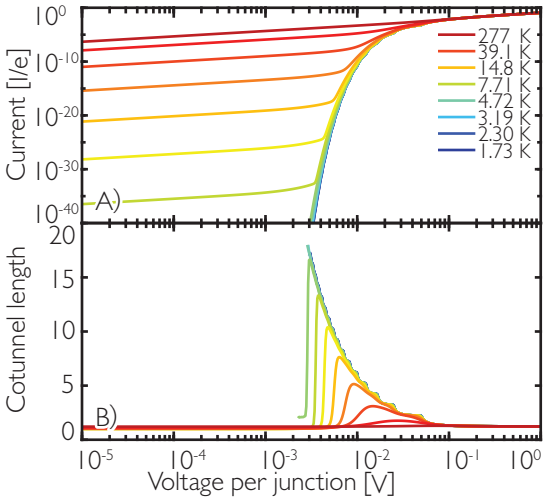

Fig. 5.3: Current versus voltage curves on a log-log scale for varying temperatures (A) with corresponding j_{mean} (B)., ${}^{G_T}/_{G_0} = 0.1$ and $E_C = 25$ meV. In the CI regime, the IV-curve is linear, as in the CIII regime. In the CII regime, the IV-curves are nonlinear, the slope increasing with decreasing temperatures. The increasing slope correlates with an increase in average cotunneling length (j_{mean}). Interestingly, transport in the CI regime is not due to multiple cotunneling, but due to sequential tunneling, in contrast to the predictions made by the Arrhenius model. Currents below 10^{-50} A e^{-1} are omitted in favour of calculation speed.

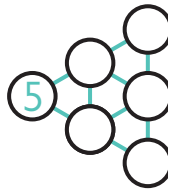

Taking a closer look at Fig. 5.3 reveals more interesting characteristics. In the CIII regime, the current is due to sequential hopping, as j_{mean} is one. Interestingly, this is also true in the CI regime, which is in contrast to previous predictions stated that transport at low bias is due to cotunneling[2]. In the CII regime, the IV-curve becomes nonlinear, which is paired with a transition from sequential tunneling ($j_{mean} = 1$) to cotunneling ($j_{mean} = 2$) to multiple cotunneling ($j_{mean} > 2$) as seen in the bottom graph. Interestingly, after reaching a maximum, the average cotunneling length decreases again, almost becoming unity. This means that (multiple) cotunneling is only significant in the intermediate CII regime.

In the C2 regime of the Arrhenius model the current should scale as follows: $I \propto V^{\alpha}$, with $\alpha = 2j_{mean} - 1$†. This means that the slope α in Fig. 5.3 (top graph) should directly relate to the cotunneling length, as $\alpha = 2j_{mean} - 1$. With this in mind, we calculate the predicted j_{mean} from the slope for the data in Fig. 5.3. The results can be seen in Fig. 5.4.

Comparing the data in Fig. 5.4 to Fig. 5.3B shows that the estimated cotunneling length

†Dayen *et al.* [2] use the variable N, which is very similar to j_{mean}. N is derived by assuming that all current has a cotunneling length of j_{opt} and that j_{opt} is a continuous variable.

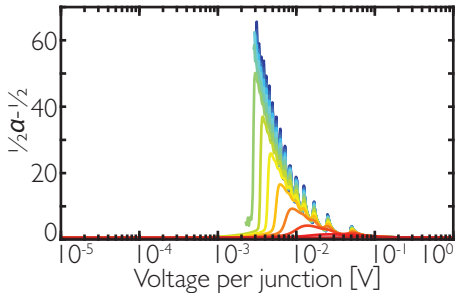

Fig. 5.4: $^1/_2\alpha - {}^1/_2$ (α is the slope of the IV-curve on a log-log scale) of the IV-curves in Fig. 5.3 versus V_{jct}. In the CI and CIII regimes, the slope is unity, but in the CII regime, the slope increases with decreasing temperature. The peaks in the slope correlate with the stepwise increase of j_{mean} in the previous figure. At low voltages and temperatures, the current is lower than 50 A e^{-1} and is omitted, hence the absence of data here.

correlates very well with j_{mean}. However, the estimated cotunneling length is much larger, going up to 60, whereas j_{mean} only reaches around 18. Furthermore, the function is not smooth, but contains peaks, especially at lower temperatures. These peaks correspond to stepwise increases in the cotunneling length, as also seen in Fig. 5.3B. This means that although there seems to be a correlation, there is no one-to-one connection between the predicted cotunneling length and the actual cotunneling length j_{mean}. From this, we predict that the slope of the log-log IV curve holds no direct information about the cotunneling length. Additionally, we did a more thorough exploration of the parameter space for both models, and found no direct correlation between j_{mean} and the slope, even for the Arrhenius model. These data can be found in appendix D.

5.5 Comparison to experimental data

In order to test the new model and compare it to the Arrhenius model, both were fitted to experimental data. A sample was prepared according to the procedures described in chapter 4. The nanoparticles used had a diameter of 10 nm and had dodecanethiol ($C_{12}SH$) as capping ligands. I-V curves were taken at various temperatures. The results are shown in Fig. 5.5. The data points below the noise floor were removed by hand.

At high temperatures, the I-V behavior is linear, indicating sequential transport outside of the Coulomb blockade regime. At high bias, the same is true for all temperatures, as the Coulomb blockade is lifted electrostatically. At 50 K and below, however, the current deviates from linearity, which indicates the onset of the Coulomb blockade. Especially at temperatures below 10 K, the current decreases very rapidly with decreasing voltage.

Fitting these data with both models proves difficult. Although its only parameters are $G_{\mathcal{T}}$ and E_{C}, the result of changing even one of these has a complex influence on the shape of the curves. Moreover, as the model depends on the voltage per junction V_{jct}, the number of nanoparticles between the electrodes N is an additional parameter. Lastly, as the devices do not have single chains of nanoparticles but entire arrays, the geometry also determines the current. The geometry is taken into account through the aspect ratio (AR, length divided

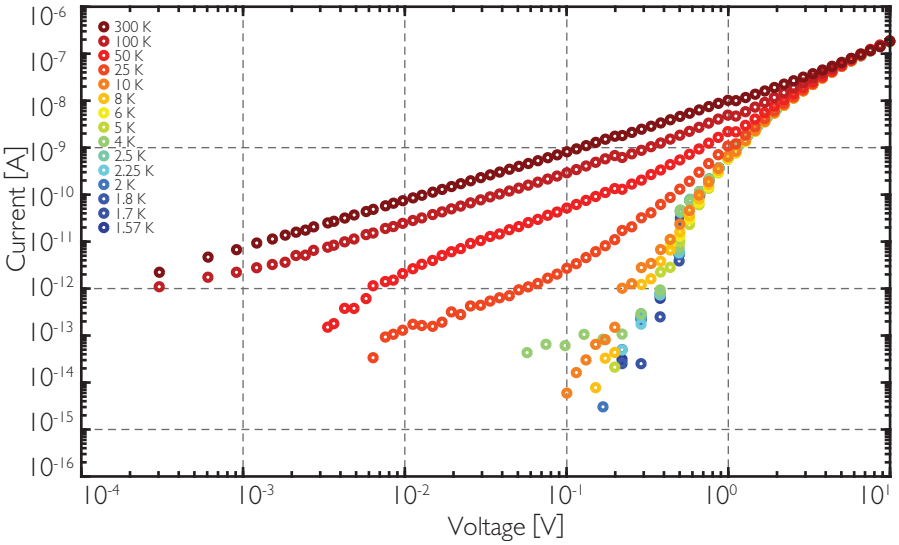

Fig. 5.5: Current versus voltage plots of an array of 10 nm diameter nanoparticles capped with dodecanethiol at various temperatures, plotted on a double-log scale. The data points below the noise floor were removed by hand. The discontinuities at 1 V and 0.2 V come from stitching together three datasets. At 300 K and 100 K, the I-V behavior becomes Ohmic., the same is true for all temperatures at high bias >3 V. Below this voltage, the curves start to deviate from linearity, especially at low temperatures.

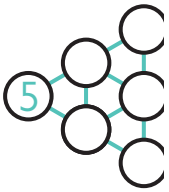

by width), the fourth and final parameter.

As the new model should reduce to Ohmic behavior at high temperatures, this puts limits on the other variables. At high temperatures, cotunneling should not contribute to the current, and the model reduces to:

$$I = \frac{1}{\sqrt{3}} AR\, G_{\mathcal{T}} \frac{V}{N}. \tag{5.18}$$

This equation can be rewritten to yield:

$$N = \frac{AR\, G_{\mathcal{T}}}{\sqrt{3}\, G}, \tag{5.19}$$

where G is the conductance of the network at room temperature. Making a linear fit to the current at room temperature gives G, which is used to constrain N. Furthermore, as E_C

can be estimated from the transition voltage V_{tr} (ideally, $V_{tr} \propto NE_C$) where linear behavior transitions into nonlinear behavior, this can be used as a starting point for the fitting process.

As we fit both the alternative model as the Arrhenius model, it is worthwhile to look at the latter one again. The original Arrhenius model diverges, which will not provide a fair comparison. This model has two terms that diverge: both $\mathcal{P}$ from Eq. 5.2 and $\mathcal{N}$ from 5.3. To correct for this, $\mathcal{P}$ was constrained by taking the arctangent of it, resulting in Eq. 5.12. Similarly, $\mathcal{N}$ was constrained by taking the arctangent of the exponential term. The resulting equation fitted to the data is given by:

$$I = ARV_{jct} \sum_j \left(\frac{G_\mathcal{T}}{G_0}\right)^j \left[\frac{2}{\pi}\arctan\left(\frac{\pi}{2}\frac{(eV)^2 + (2\pi k_B T)^2}{E_C^2}\right)\right]^{j-1} \times \frac{2}{\pi}\arctan\left(\frac{\pi}{2}\exp\left[\frac{jeV_{jct} - E_C/j}{k_B T}\right]\right). \quad (5.20)$$

Similarly for the alternative model, Eq. 5.13 is multiplied by AR to yield the current according to the new model. Using these estimates, both models were fitted to the data. The fitted parameters were $G_\mathcal{T}$, AR and V_{tr}. The parameters E_C and N were functions of the other parameters through V_{tr} and as a result of Eq. 5.19. In order to increase the weight of the currents at low temperatures and voltages, the logarithm of the data was fitted to the logarithm of the model. The results can be seen in Fig. 5.6, the top graph shows the fit of the new model, the bottom graph shows the fit of the Arrhenius model. The fitted parameters for both models are shown in the table below.

	E_C	$G_\mathcal{T}$	AR	N
New model	3.5 meV	$4.12{\cdot}10^{-9}$ G_0	379	209
Arrhenius model	3.4 meV	$4.17{\cdot}10^{-9}$ G_0	379	212

It can be seen from the figure that although the general trend of the I-V curves are captured by the model, the fit is not very good. Although the curves seem to match the data, the fits do not match the trends in temperature. It matches the current at high temperatures due to the constraints discussed above, but the fit does not overlap with the data at low temperatures. This is not only true for the alternative model; the Arrhenius model also suffers the same flaw. More importantly, the Arrhenius model predicts that the current above V_{tr} is higher for lower temperatures, something that clearly conflicts with available data[‡]. The alternative model does correctly predict lower currents at lower temperatures above V_{tr}, but similarly predicts currents that are too large at low temperatures. Moreover, as the nanoparticles have a diameter of 10 nm and the distance between the electrodes is 500 nm, the predicted value for N; 209 and 212 are not realistic. From this, we conclude that neither of

[‡]It should be noted however that this model is only considered valid when $jE_C > V_{jct}$, which is not the case at these high bias values.

these two models is sufficient to describe current through networks of nanoparticles, even when given a large parameter space to explore.

There is one thing, however, that this model does not capture: disorder. The two models assume perfect linear chains of nanoparticles, rather than networks. Real networks have imperfections such as crystal boundaries, variations in nanoparticle size and trapped charges in the substrate below.

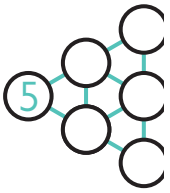

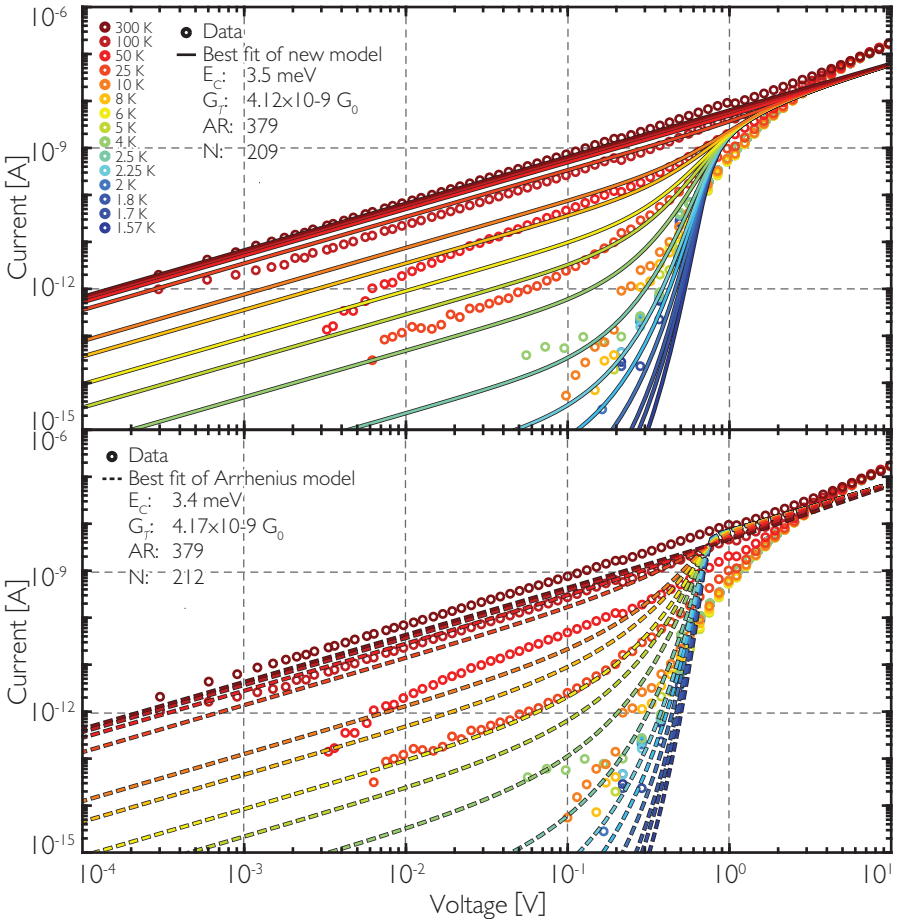

Fig. 5.6: Current versus voltage plots of an array of 10 nm diameter nanoparticles capped with dodecanethiol at various temperatures, plotted on a double-log scale. The circles are the data points, the lines are the fits to the data. The top graph shows the fitted curves using the new model, the bottom graph shows the fitted curves using the old model.

5.5.1 Disorder

Disorder in nanoparticle networks can have different origins: variations in nanoparticle size and trapped charges in the substrate lead to variations in E_C. This in addition to holes in the network can cause percolation effects, as some current paths are more favourable than others. Moreover, as the networks are interconnected, some nanoparticles may be part of several current-carrying paths. It can also be that favourable percolating paths do not cross the shortest distance between the two contacts, resulting in a variation in V_{jct}.

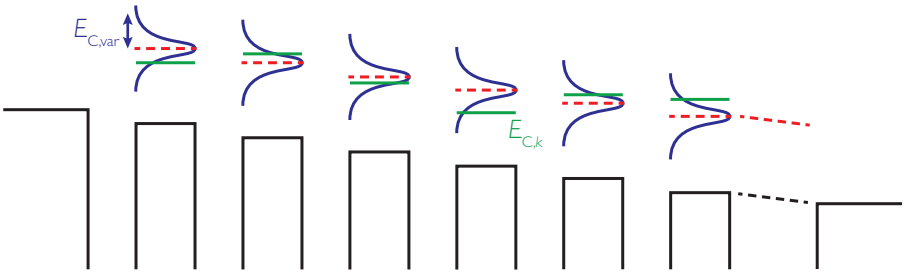

Fig. 5.7: Energy diagram of a chain of nanoparticles with a variation in charging energy. Instead of having a single charging energy E_C, each nanoparticle has a slighly different charging energy, indicated by the green lines. The variation follows a normal distribution with maximum $E_{C,0}$ (indicated by the dashed red line) and a standard deviation of $E_{C,var}$, seen in blue.

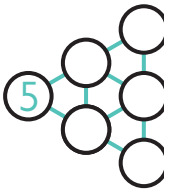

In order to take into account some of this disorder, E_C is varied along the chain, shown schematically in Fig. 5.7. This approach is very similar to that proposed by Wingreen *et al.* [12], except that after a cotunneling event with length j, it does not consider the rest of the chain. Moreover, rather than gating each nanoparticle individually and calculating the first available state in equilibrium at each voltage, only E_C is varied[§] The cotunneling current is calculated for many (around 10 000) of these chains in parallel, each with different charging energies. The charging energy is varied according to a normal distribution, with $E_{C,var}$ the standard deviation. The probability term from Eq. 5.12 then becomes:

$$\mathcal{P}_j = \left(\frac{G_\mathcal{T}}{G_0}\right)^j \prod_{k=1}^{j-1} \frac{2}{\pi} \arctan\left(\frac{\pi}{2} \frac{(eV)^2 + (2\pi k_B T)^2}{\left(E_{C,k} - keV_{jct}\right)^2}\right). \tag{5.21}$$

The charging energy E_C is now different for each nanoparticle, and hence the product series

[§]This approximation might also include unstable states, as nanoparticle chains could be generated which could lower their energy by charge transfer from one nanoparticle to the next, especially when $E_{C,var} \approxeq E_C$. A complete model should include this consideration. For further information, we refer to the second page of the article by Wingreen *et al.* [12], where the authors discuss the maximum charge on each individual nanoparticle, putting a limit on $E_{C,i}$.

takes this into account. The probability term in the alternative model (Eq. 5.9) is adapted analogously and becomes:

$$\mathcal{N}_j = -\frac{E_{\mathrm{C},j} - jeV_{\mathrm{jct}}}{1 - \exp\left(\left(E_{\mathrm{C},j} - jeV_{\mathrm{jct}}\right)/k_{\mathrm{B}}T\right)} + \frac{E_{\mathrm{C},j} + jeV_{\mathrm{jct}}}{1 - \exp\left(\left(E_{\mathrm{C},j} + jeV_{\mathrm{jct}}\right)/k_{\mathrm{B}}T\right)}. \tag{5.22}$$

Note that this does not take into account percolation, but simply assumes that a network consists of many nanoparticle chains in parallel, *i.e.* not interconnected. The total current is then taken as the average over the currents in all individual chains. Each individual chain has different charging energies of each nanoparticle. Effectively, this model is an expansion of a previous model of disorder in nanoparticle arrays[10], which ignores cotunneling. We explicitly include cotunneling in our model.

As predicted by Wingreen *et al.*[12], disorder in networks at zero temperature will also lead to a threshold voltage, below which all current is suppressed¶. For one-dimensional chains, the current above the threshold always scales linearly with the voltage. For two-dimensional networks however, above the threshold, the current scales almost quadratically ($I \propto V^{5/3}$) with the voltage, up to another characteristic voltage, where the current scales linearly. This can be understood as follows: the current per chain scales linearly, and the number of contributing chains scales with $V^{2/3}$. Both of these terms result in a current that increases almost quadratically with voltage up to the second characteristic voltage. At this point, all chains already contribute to the current, resulting in Ohmic behavior.

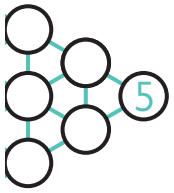

Interestingly, this should imply that the shape of the IV curve holds information about the disorder that is present in the network. As we know that at zero temperature, each chain carries a current that scales linearly with the applied voltage, as long as the voltage is higher than the threshold voltage for that chain. Any deviation in linearity can then be related back to the number of conducting chains. At finite temperatures, this should become more complex, as chains can already contribute to the current below their threshold, due to thermal excitation of the electrons. A complete description of the system that includes two-dimensional disorder rather than parallel non-connected chains should more accurately predict this. In the model developed in this chapter, however, the threshold voltage for the i^{th} chain is simply $NE_{\mathrm{C},i}$.

Using the variation in the charging energy $E_{\mathrm{C,var}}$ as a fitting parameter, both models were fitted to the previous data. The result can be seen in Fig. 5.8. The best-fit parameters for both models are shown in the table below.

	E_{C}	$E_{\mathrm{C,var}}$	$G_{\mathcal{T}}$	AR	N
New model	26.7 meV	6.45 meV	$5.44{\cdot}10^{-10}$ G_0	430	33
Arrhenius model	25 meV	6.32 meV	$8.21{\cdot}10^{-10}$ G_0	598	58

¶This makes sense, as at zero temperature, no electrons are available for transport below $eV_{\mathrm{jct}} = E_{\mathrm{C}}$.

Compared to the curves from Fig. 5.6, taking disorder into account enhances the quality of the fit drastically. Whereas both models without disorder only give moderately accurate fits for high temperatures, Fig. 5.8 shows that a variation in E_C of only 6 meV is sufficient to give good fits over the entire temperature range. The prediction of a charging energy of around 25 meV is about six times smaller than that of an isolated 10 nm nanoparticles, a reasonable value[13]. As the fitted charging energy is roughly equal to $k_B T$ at room temperature, we expect that the curves will start to deviate from linearity when cooling down. This deviation can indeed be seen in the data, although the current still behaves roughly Ohmically even at 50 K. We expect that this is due to chains of nanoparticles with a lower charging energy, which carry a large part of the total current. The parameters $G_\mathcal{T}$, AR and N also have values in line with expectations. Although the designed AR of 10 000 is much larger than the fitted 430 and 598, this can be explained by low network quality. If cracks and holes are present in the largest part of the network, it could very well be that only around 5% of the device is connected, resulting in a lower than expected aspect ratio. The number of nanoparticles determined from the fits are 33 for the new model and 58 for the Arrhenius model. Additionally, N can be determined from SEM images, and was found to be around 40.

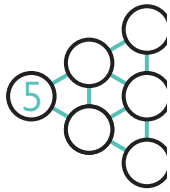

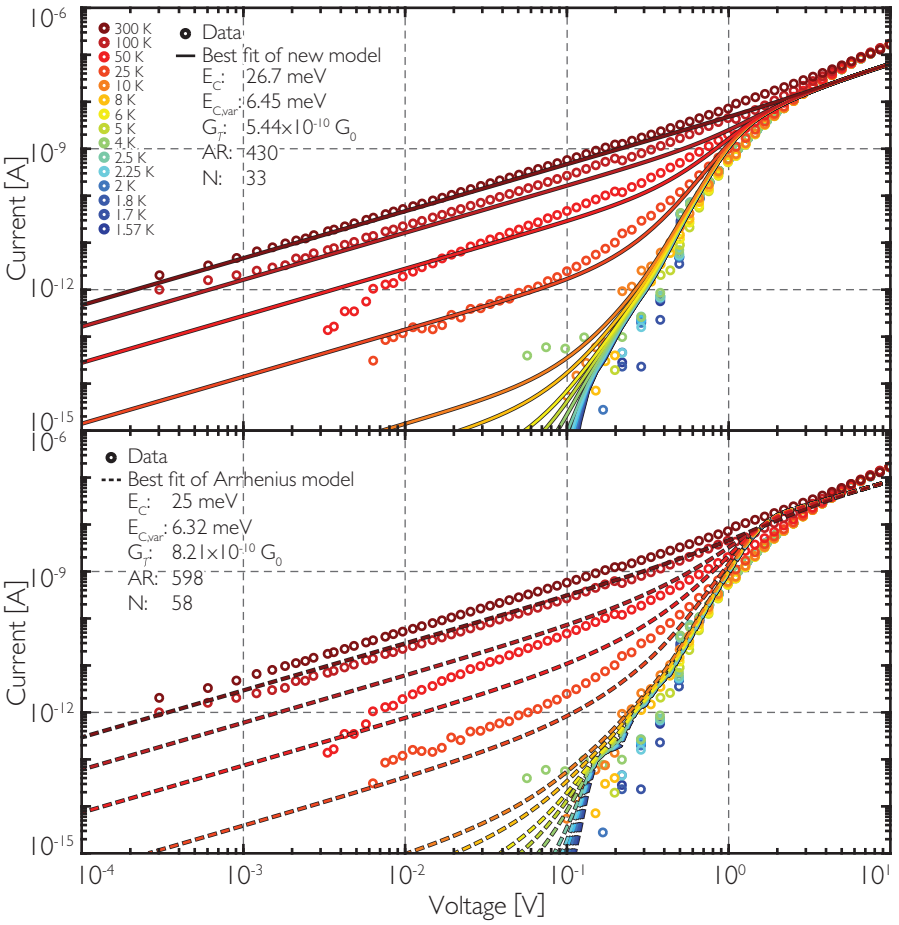

Fig. 5.8: Current versus voltage plots together with the curves fitted by the models taking into account disorder. The top graph shows the fitted curves using the new model, the bottom graph shows the fitted curves using the old model. It can be seen that taking disorder into account greatly increases the quality of the fits for both models, compared to Fig. 5.6. Especially the new model follows the IV curves accurately, even down to low temperatures, where the current hits the noisefloor. Moreover, the best fit parameters are roughly equal for both models, only being significantly different for N and AR. These fits indicate that disorder cannot be ignored when describing the current through nanoparticle networks.

As a second test, we performed molecular place-exchange on the network, using biphenylthiol (BPT) as the exchange molecule. As BPT is a monothiol, it does not chemically connect two neighboring nanoparticles. However, the molecules are more conductive[14], and the $\pi - \pi$ stacking between neighbouring molecules should allow the electrons to more easily tunnel from one nanoparticle to the next[15]. Ideally, this only changes $G_{\mathcal{T}}$. Additionally, exchange also affects the dielectric constant of the effective medium surrounding the nanoparticles, and hence slightly changes E_{C}. After exchange, the current through the networks was measured analogous to before exchange. Using the same values for AR, N as for Fig. 5.8, but leaving no constraints on E_{C}, $G_{\mathcal{T}}$ and $E_{\mathrm{C,var}}$, the models were again fitted to the data. The results can be seen in Fig. 5.9. The best-fit parameters for both models are shown in the table below.

	E_{C}	$E_{\mathrm{C,var}}$	$G_{\mathcal{T}}$	AR	N
New model	21.4 meV	5.22 meV	$4.40{\cdot}10^{-5}$ G_0	430	33
Arrhenius model	16.7 meV	4.07 meV	$5.02{\cdot}10^{-6}$ G_0	598	58

After exchange, the high-bias resistance of the network has decreased from 100 MΩ to only 10 kΩ, indicating successful exchange. This change in resistance of five orders of magnitude directly translates to a change in $G_{\mathcal{T}}$ of the same order of magnitude when fitted using the new model. The old model shows the same trend, although it predicts a change of the tunneling conductance one order of magnitude less. The parameters E_{C} and $E_{\mathrm{C,var}}$ also change slightly, E_{C} decreases by 20% in the new model, and 33% in the old model, with $E_{\mathrm{C,var}}$ showing the same pattern. This is to be expected when variation in E_{C} stems mostly from variations in nanoparticle size, as $G_{\mathcal{T}}$ changes with E_{C} through the dielectric constant of the medium. ♮

Most importantly, the fits to the data indeed show that the models can both be fitted to the post-exchange data, with no change in geometry and only a small change in E_{C}. Especially the new model matches the trends shown in the experimental data, such as the transition to nonlinear behavior. The data shows a smooth transition where the current deviates further from linearity as the temperature and voltage decrease. At low voltages, the Arrhenius model shows similar behavior. However, at high voltages ($>$1.5 V), it instead predicts that the current is higher at lower temperatures, a feature that is not observed experimentally. From this, we conclude that using the full equation with the Fermi-Dirac distribution shown in Eq. 5.9 is the more accurate model, especially at high bias and temperature. We additionally fitted data from a second device on the same sample, which can be found in Fig. E.1 in the appendix. The findings here also support what we found in this section. As an attempt to compare the data from these networks to networks of nanoparticles with different sizes, we also made devices with 5 nm nanoparticles. However, due to fabrication issues and organic residue on the sample, we were not able to obtain conclusive data.

♮ Interestingly $E_{\mathrm{C,var}}$ is internally determined as a percentage of E_{C}, which hardly changes at all between the pre- and post-exchange situations.

Interestingly, all data show a slight deviation from linearity at high bias (>3 V). This was seen previously by Tran *et al.* [3], who explained it by disorder. However, this disorder should be captured by our model as well, which however still predicts Ohmic behavior at high bias. The observed deviation from linearity could be due to nonlinear transport characteristics between the nanoparticles themselves (*i.e.* due to an energy-dependent transmission function). This implies that the corresponding transmission probability varies significantly with electron energy (see chapter 3). Although this is possible, the effect should be low, as the voltage drop per nanoparticle even at high bias is only on the order of 100 mV, and the typical distance of a molecular level from the Fermi energy of gold is a few eV. It could also be the deviation from linearity is caused by percolation, as our model does not fully capture this feature.

Summarizing, our data suggests that disorder is a key factor in understanding electron transport in nanoparticle arrays. Although a variation in E_C captures a large part of this disorder, the data can still not be fully matched to the model. As the number of nanoparticles per chain can differ from one to the next, we predict that incorporating a variation in V_{jct}, analogously that in E_C will result in a model that follows the data even better.

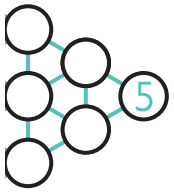

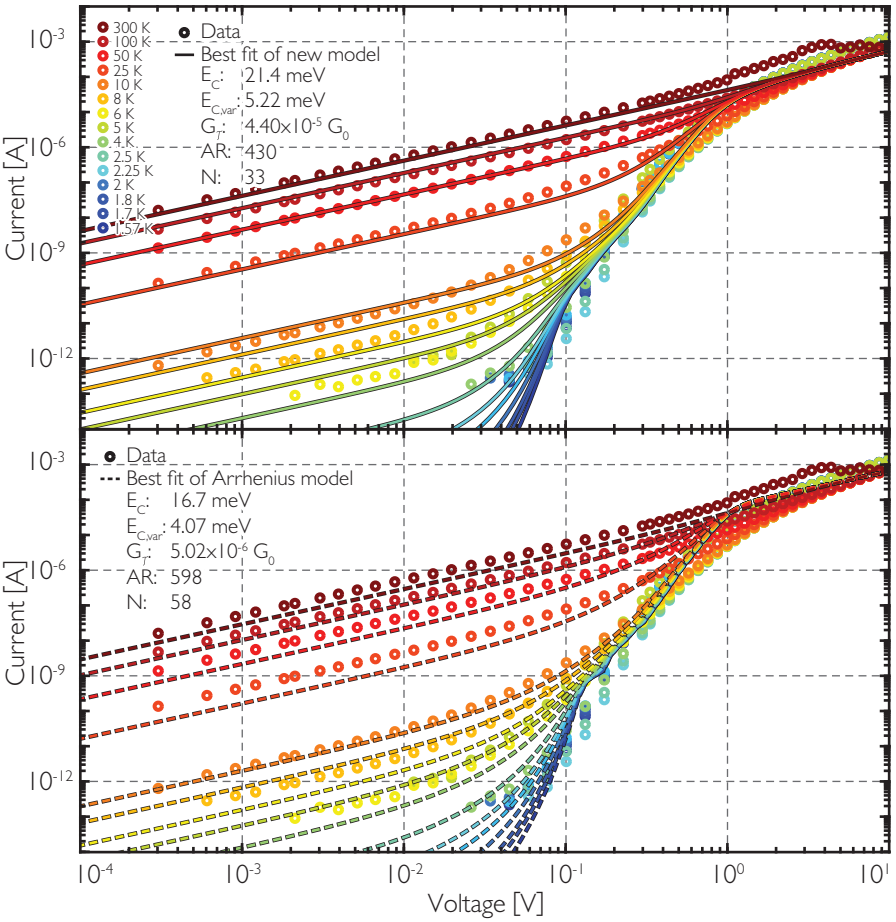

Fig. 5.9: Post-exchange current versus voltage plots together with the curves fitted by the models taking into account disorder. The top graph shows the fitted curves using the new model, the bottom graph shows the fitted curves using the old model. The fits show that a large change in $G_{\mathcal{T}}$ and relatively small changes in E_{C} and $E_{\mathrm{C,var}}$ are sufficient to fit the data. At low voltages specifically, both models fit the data relatively well. At high bias however, the Arrhenius model incorrectly predicts that the current increases with decreasing temperature. At these voltages, the new model more accurately captures the behavior.

5.6 Cotunneling length

Now that the validity of both models has been discussed, it is interesting to look at their consequences. As seen before, the I-V behavior of nanoparticle networks deviates from linearity at low temperatures and bias, resulting in a steeper slope on a double log scale. According to Dayen *et al.* [2], this is due to multiple cotunneling, and the slope can be directly related to the multiple cotunneling length. Moreover, the cotunneling length at zero bias should scale inversely proportional to the square root of temperature.

To see if this trend is also present in the current dataset, we take the log-log derivative ($\alpha = {}^{\mathrm{d}\log(I)}/_{\mathrm{d}\log(V)}$) of the post-exchange measured data and use this to calculate the predicted cotunneling distance. The result is shown in Fig. 5.10.

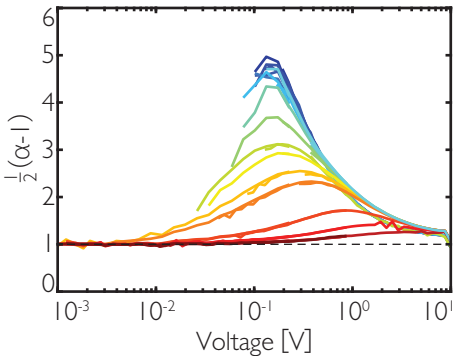

Fig. 5.10: Predicted cotunneling distance within the Arrhenius model versus voltage at different temperatures, determined from the measured data in Fig. 5.9 (the colors representing the temperature are the same as in Fig. 5.9). The parameter α is the slope of the double log I-V curve (${}^{\mathrm{d}\log(I)}/_{\mathrm{d}\log(V)}$), which relates to the predicted cotunneling distance as seen on the vertical axis label. The data below the noise floor is removed by eye for visual clarity, the original data can be found in the appendix (see Fig. E.2). The dashed line indicates Ohmic transport. The maximum slope increases with decreasing temperature.

As can be seen in the figure, α approaches unity at high voltage for all temperatures, indicating close-to Ohmic behavior. At high temperatures, the behavior is Ohmic at all voltages, as the Coulomb barrier can be overcome thermally. As the temperature and voltage decreases however, the slope increases to a maximum and then decreases again. This maximum is larger for lower temperatures and additionally occurs at lower voltages. For sufficiently low temperatures and voltage, the current drops below the noisefloor, causing a wildly fluctuating slope. These datapoints are removed, the full dataset can be found in Fit. E.2 in the appendix. To see how the slope scales with temperature, the maximum of the slope is taken and plotted versus temperature in Fig. 5.11 (note that the temperature scale is not linear, but scales with $T^{-0.5}$).

The figure shows that the maximum of the slope increases as the temperature decreases. More specifically, it scales approximately inversely proportional to the square root of temperature. Within the reasoning by Dayen *et al.*, the transport through our network should be almost completely sequential at room temperature. Below 25 K, most of the transport is facilitated through cotunneling, and below 5 K, multiple cotunneling is dominant, increas-

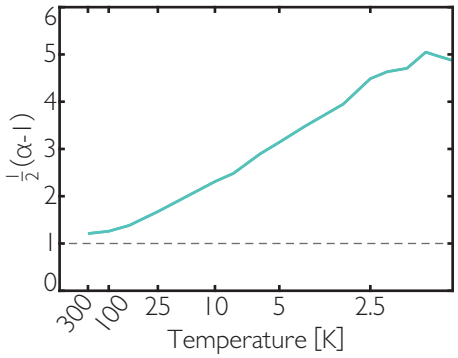

Fig. 5.11: Maximum of the predicted cotunneling distance versus temperature determined from the data in Fig. 5.10, the horizontal axis increases inversely proportional to the square root of the temperature. The predicted cotunneling distance scales linearly with $T^{-0.5}$, in agreement with the prediction made by Dayen *et al.*.

ing to a maximum distance of five nanoparticles at 1.58 K.

With these data, we show that our findings are in line with previous measurements done on similar systems. We have seen that using disorder, we can accurately fit the data and get reasonable fitting parameters, both pre- and post-exchange. Moreover, the predicted cotunneling length matches the trend in the data in earlier articles. However, as we now have a working model, we can use this model to accurately calculate the actual cotunneling length in our system.

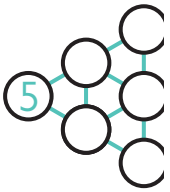

5.6.1 IS THERE HIGHER-ORDER TRANSPORT?

As we now have a working model to describe transport through the networks, we can use this model to directly predict the average cotunneling distance j_{mean} (see Eq. 5.14) from the fitted parameters. To do so, the current was calculated individually for each cotunneling distance. From this, we calculate j_{mean} cotunneling distance and plot it as a function of voltage for the temperatures used in the experiment. We do this for both the new model and the Arrhenius model by Tran *et al.*[4], using the parameters extracted from the fits. The results are shown in Fig. 5.12.

Strikingly, neither the new, nor the old model needs cotunneling to explain transport in this system. Only at the lowest temperatures, cotunneling contributes somewhat to the current, albeit only around 1% according to both models. Additionally, as the voltage decreases, j_{mean} reaches a maximum at around 20 meV and then decreases again. Here, both models slightly diverge in their predictions, as the new model predicts a j_{mean} of one, and the Arrhenius model predicts a non-unitary j_{mean}. This is similar to what we saw earlier in Fig. 5.3, where j_{mean} reaches a maximum, and then decreases again. In both models, the maximum values of j_{mean} are so close to unity, that for all practical purposes, cotunneling can be completely ignored when discussing electron transport in nanoparticle arrays.

This finding is in stark contrast with earlier reports, which stated that cotunneling is key in understanding the current through networks of nanoparticles[1–4]. We think that

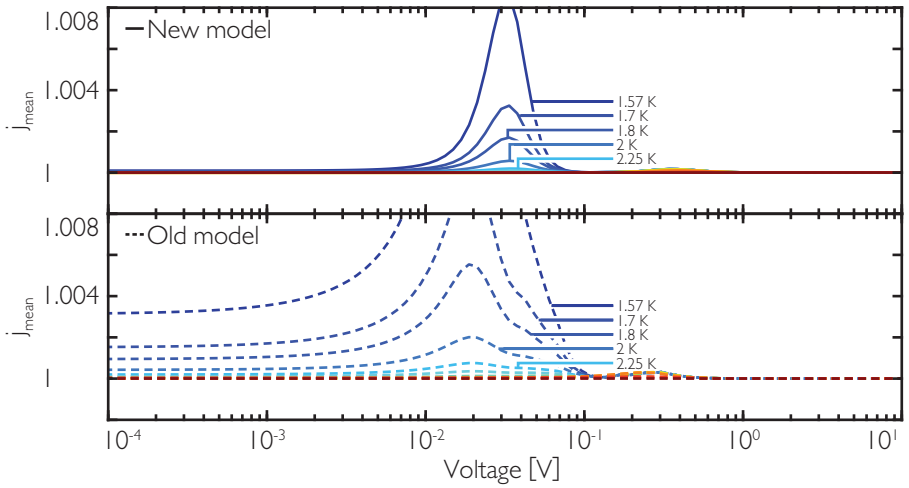

Fig. 5.12: Calculated average cotunneling length versus voltage for different temperatures, using both the new and Arrhenius models and their fitted parameters from the post-exchange data in Fig. 5.9. Interestingly, neither models indicate the presence of cotunneling, as j_{mean} is almost one.

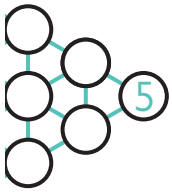

this is because fitting a complete model to the data has not been done before. Most data analysis in earlier research relied on *ad hoc* approximations of the Arrhenius model (leading to three different regimes: C1, C2, C3), rather than the full model itself. We now find that the features of these approximations, such as the trend in α in Fig. 5.11, can be captured by our model as well, completely ignoring cotunneling. In our model, the trend is due to the disorder in the network becoming more pronounced at lower temperatures, rather than due to a change in cotunneling length.

The trend in Fig 5.12, and also the trend in Fig. 5.10 should then be due to the disorder in E_{C}. At higher temperatures, the thermal energy of the electrons is high enough to smear out this disorder, as $k_{\text{B}}T > E_{\text{C,var}}$. At lower temperatures, the effect of the distribution of E_{C}becomes more pronounced, as each individual nanoparticle chain has a more clearly defined V_{tr} where it starts conducting. If this is indeed the case, the specific trend in α does not hold information on the cotunneling distance (as predicted by Dayen *et al.*[2]), but rather on the disorder in the array.

5.7 Conclusion

We explored electron transport in nanoparticle arrays from a theoretical perspective and developed a new model to capture sequential transport, as well as higher order behavior. The

new model does not suffer from the divergencies that the model developed by Tran *et al.* [4] does. Additionally, this is, to our knowledge, the first model that both includes cotunneling as well as disorder. Moreover, the shape of the I-V curves calculated with the alternative model more closely resembles the experimental data. We tested both models by fitting them to experimental data. Here we found that a good fit with realistic parameters can only be achieved when taking into account disorder in the networks. By averaging the current through chains of nanoparticles, each of which with a different Coulomb charging energy, we obtain good fits to the experimental data. Strikingly, using the parameters extracted from the fit, we calculate that (multiple) cotunneling does not contribute to the current significantly. This is true both for our model and the previous model. We therefore conclude that electron transport through our Coulomb blockaded arrays of nanoparticles is not due to higher order processes, but simply due to thermally and electrostatically excited sequential hopping in the presence of significant disorder. Additionally, our model captures the same features observed by earlier studies [1–4], such as the scaling of α with $T^{-0.5}$, or even the enhanced sensitivity to the interconnecting molecules, as we will see in the next chapter.

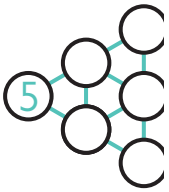

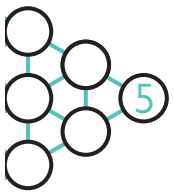

References

[1] H. Moreira, Q. Yu, B. Nadal, B. Bresson, M. Rosticher, N. Lequeux, A. Zimmers, and H. Aubin. Electron cotunneling transport in gold nanocrystal arrays. *Physical Review Letters*, 107(17), 2011.

[2] Jean-Francois Dayen, Edwin Devid, Mutta Venkata Kamalakar, Dmitry Golubev, Constant Guédon, Vina Faramarzi, Bernard Doudin, and Sense Jan van der Molen. Enhancing the Molecular Signature in Molecule-Nanoparticle Networks Via Inelastic Cotunneling. *Advanced Materials*, 25(3):400–404, 2013.

[3] T. Tran, I. Beloborodov, Jingshi Hu, X. Lin, T. Rosenbaum, and H. Jaeger. Sequential tunneling and inelastic cotunneling in nanoparticle arrays. *Physical Review B*, 78(7), 2008.

[4] T. Tran, I. Beloborodov, X. Lin, T. Bigioni, V. Vinokur, and H. Jaeger. Multiple Cotunneling in Large Quantum Dot Arrays. *Physical Review Letters*, 95(7), 2005.

[5] Mikhail Viktorovich Feigelman and Alexey Solomonovich Ioselevich. Variable-range cotunneling and conductivity of a granular metal. *Journal of Experimental and Theoretical Physics Letters*, 81(6):277 283, 2005.

[6] I. Beloborodov, A. Lopatin, V. Vinokur, and K. Efetov. Granular electronic systems. *Reviews of Modern Physics*, 79(2):469–518, 2007.

[7] I. Beloborodov, A. Lopatin, and V. Vinokur. Coulomb effects and hopping transport in granular metals. *Physical Review B*, 72(12), 2005.

[8] D. V. Averin and Yu V. Nazarov. Virtual Electron diffusion during quantum tunneling of the electric charge. *Physics Review Letters*, 65(16):2446–2449, 1990.

[9] Rolf Landauer. Spatial variation of currents and fields due to localized scatterers in metallic conduction. *IBM Journal of Research and Development*, 1(3):223–231, 1957.

[10] Mir Massoud Aghili Yajadda. Calculating electronic tunnel currents in networks of disordered irregularly shaped nanoparticles by mapping networks to arrays of parallel nonlinear resistors. *Journal of Applied Physics*, 116(15):153707, 2014.

[11] K.-H. Müller and M. M. A. Yajadda. Electron transport in discontinuous gold films and the effect of Coulomb blockade and percolation. *Journal of Applied Physics*, 111 (12):123705, 2012.

[12] A. Alan Middleton and Ned S. Wingreen. Collective transport in arrays of small metallic dots. *Physical review letters*, 71(19):3198, 1993.

[13] Chao Duan, Ying Wang, Jinling Sun, Changrong Guan, Sergio Grunder, Marcel Mayor, Lianmao Peng, and Jianhui Liao. Controllability of the coulomb charging energy in close-packed nanoparticle arrays. *Nanoscale*, 5:10258–10266, 2013.

[14] Songmei Wu, Maria Teresa González, Roman Huber, Sergio Grunder, Marcel Mayor, Christian Schönenberger, and Michel Calame. Molecular junctions based on aromatic coupling. *Nature Nanotechnology*, 3:569, 2008.

[15] Riccardo Frisenda, Vera A. E. C. Janssen, Ferdinand C. Grozema, Herre S. J. van der Zant, and Nicolas Renaud. Mechanically controlled quantum interference in individual π-stacked dimers. *Nature Chemistry*, 8(12):1099–1104, 2016.

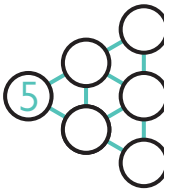

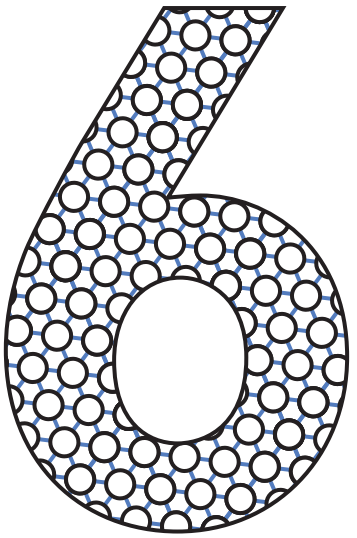

Nanoparticle network devices interlinked by molecular switches

6.1 INTRODUCTION

6.1.1 PREDICTION OF ENHANCED SWITCHING

In the previous chapter, we stated that cotunneling in nanoparticle networks does not give a significant contribution to the total current, even at low temperatures. This has an important impact on the expectation by Dayen *et al.* [1], who predicted that the ON-OFF ratio of a device incorporating molecular switches should scale with the cotunneling distance. Indeed, if cotunneling does not occur, no direct enhancement of the ON-OFF ratio should be expected, assuming that switching only changes $G_\mathcal{T}$. However, switching also has an indirect effect, as changing $G_\mathcal{T}$ changes ϵ and hence E_C. This in turn changes the current at low temperature.

To investigate if this can lead to sizeable effects, we calculated IV curves for two systems (one high-conductance, one low-conductance) with parameters similar to those used in the previous chapter. The parameters are defined as shown in the table below. We discarded all currents lower than 10 fA, to replicate the noise floor in our set-up. We then calculated the ratio of the currents and plotted the maximum ratio versus the temperature, as can be seen in Fig. 6.1.

	E_C	$E_\mathrm{C,var}$	$G_\mathcal{T}$	AR	N
High conductance	20 meV	4 meV	$G_\mathcal{T}$=4.40·10^{-5} G$_0$	430	33
Low conductance	25 meV	5 meV	$G_\mathcal{T}$=8.80·10^{-7} G$_0$	430	33

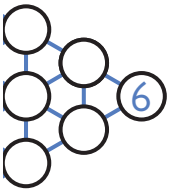

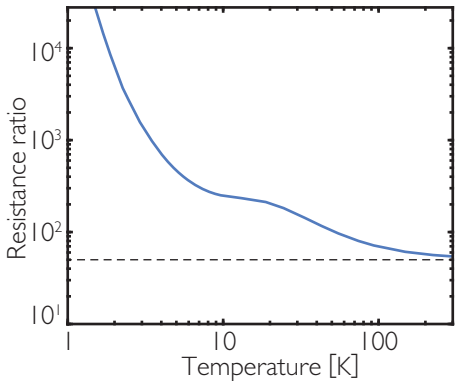

Fig. 6.1: Calculated (using the alternative model from chapter 5) maximum resistance ratio of two systems with a factor of 50 difference in $G_\mathcal{T}$ and a 20% difference in E_C and $E_\mathrm{C,var}$ versus temperature. To increase the speed of computation, (multiple) cotunneling was ignored, and only values for $j = 1$ were calculated. The blue line shows the calculated maximum of the resistance ratio, the dashed black line shows the expected ratio if transport was only Ohmic. As can be seen from the graph, the resistance ratio increases dramatically as the temperature decreases, even without cotunneling.

This figure shows that even without cotunneling, the maximum resistance ratio increases rapidly with decreasing temperature. This is similar to an analogous result found by Dayen *et al.* [1] and shown in Fig. 2.12, which shows that the resistance ratio between a pre- and a post-exchange device increases with decreasing temperature. We found that increasing E_C

increases the maximum ratio and additionally saw that increasing $E_{C,var}$ decreases the maximum ratio at lower temperatures. These results seem to suggest that nanoparticle networks can indeed be used to enhance the ON-OFF ratio of molecular switches, without even needing cotunneling to explain this phenomenon.

6.2 MOLECULAR SWITCHES

As discussed in chapter one, molecular switches are arguably among the most interesting types of functional molecules[2,3]. These are molecules that can switch between multiple states, where each state has distinct optical, electronic or chemical properties. They are interesting from a fundamental point of view, as the quantum mechanical nature of the switching can be studied in the lab. Additionally, they have many possible applications, such as chemical sensors (*e.g.* pH sensors[4]) or optoelectronic circuits[5]. In these two cases, the resistance of the molecule changes upon capture of a chemical species or upon absorption of light, respectively. It is of course important that the change in resistance is large enough to measure. The switchable molecular device discussed briefly in chapter one has a resistance that only changes by 20% upon illumination[2], much lower than the orders of magnitude difference between the ON and OFF states of the average transistor.

This resistance ratio could be improved chemically, by altering the molecule. However, a molecule can only be changed so much before it loses its functionality. As discussed in the previous section, a Coulomb blockaded network of nanoparticles has an enhanced sensitivity to the molecules between the particles. By incorporating the molecular switch into the network, the ON-OFF ratio of the entire network can become larger than the ON-OFF ratio of the individual switches.

This chapter focuses on the trans-10b,10c-dimethyl-10b,10c-dihydropyrene molecular switch, as seen in Fig. 6.2. This molecule has two stable states: a closed DHP state, and an open CPD state*, the cores of which are illustrated in Fig. 6.3. The DHP isomer is the most stable of the two and has a deep red color, contrasting with the open metastable CPD state, which is colorless. Illumination of the DHP state with visible light breaks the center bond in the molecule, causing the two phenyl rings on either side to snap out of plane. The resulting CPD state has less orbital overlap, causing both sides of the molecule to be electronically separated, and hence has a lower conductance[6]. Switching back to the DHP state can be accomplished by illumination with UV-radiation, or by thermal excitation, illustrated in Fig. 6.3. An important reason for choosing this particular switch is the fact that the change in length upon switching is negligible. Hence, mechanical hampering of the switching process is not expected.

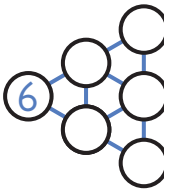

*DHP and CPD are abbreviations of DiHydroPyrene and CycloPhaneDiene respectively, referring to the cores of the molecules.

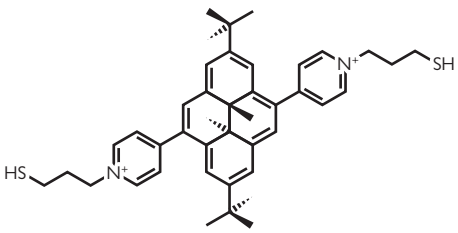

Fig. 6.2: Schematic depiction of the DHP based molecular switch (trans-10b,10c-dimethyl-10b,10c-dihydropyrene). The two thiol groups on either end facilitate the binding to the gold nanoparticles. The pyridine rings are present to decouple the core of the molecule from the contacts, while still allowing electronic transport through the molecule[7].

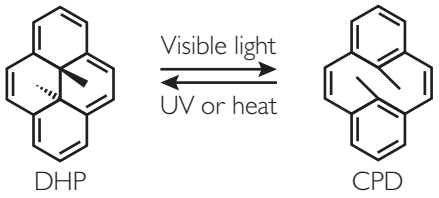

Fig. 6.3: Schematic depiction of the two states of the cores of the molecular switch. The high-conductance DHP state can be switched to the low-conductance CPD state by illumination with visible light. Switching back can be done by applying heat or illuminating with UV radiation. Adapted from Roldan *et al.*[6].

This change in conductance upon switching was tested in solution using a MCBJ by Roldan *et al.*[6] on a very similar molecule†. For the DHP state, they found a conductance of 10^{-4} G_0. Upon illumination with visible light however, the conductance changed to $\approx 10^{-8}$ G_0, a change of almost four orders of magnitude. This change was reversible, as the conductance changed back to the original value of 10^{-4} G_0 upon heating of the solution. These results suggest that both states are stable when connected to electrodes. Moreover, the two states have very different conductances.

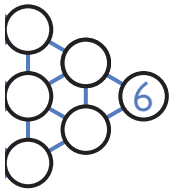

There is a caveat however, as it is not clear if switching occurs when the molecule is contacted. As the measurements are done in solution, each conductance trace is most probably a measurement of a different molecule. It is therefore likely that the molecules switch in solution, before being contacted to the MCBJ where they are measured. This means that although switching is observed in this particular setting, it is likely that the ON and the OFF states are not the same molecule. Therefore, it is not clear whether or not the molecules can be switched after being contacted.

6.3 Device fabrication

Device fabrication was done analogously to the procedure in section 4.3.1. Prior to exchange, the room temperature resistance of the devices was checked in a probe station. As the molecular switch, trans-10b,10c-dimethyl-10b,10c-dihydropyrene (DHP) was used. Due

†The only difference is the presence of the thiol groups, which are present in our molecule, but are not present in the cited research. Roldan *et al.*[6] used pyridine anchoring groups for binding to the contacts of the MCBJ.

to the small available quantity of the molecule, only around half a milligram was dissolved in a mixture of THF with 20% triethylamine. Since this switch reacts irreversibly with oxygen upon illumination [8,9], special care was taken when the network was in contact with oxygen. To minimize contact with the ambient environment, the device was attached to the chip carrier under nitrogen atmosphere and transported to the cryostat wrapped in aluminum foil. Loading the sample was done in the dark.

6.4 Optical measurements

First, the switchable molecules were tested for switchability in solution. For that, a tiny amount of material was dissolved in acetonitrile to create a solution with an estimated concentration of 1.2 μM, which was placed into a 1 cm quartz cuvette. The solution was illuminated using a tungsten halogen light source (5 W) to measure the optical absorption spectrum as a function of time. The results can be seen in Fig. 6.4.

At the start of the measurement (indicated by the topmost dark blue curve), the spectrum shows two peaks at 530 nm and 683 nm, in agreement with previous results [6]. Illuminating with visible light should switch the molecule to the colorless CPD state. This is indeed observed, as the initial spectrum shows distinct peaks at 530 nm and 683 nm, which decrease in height over time (time progression is indicated by the color of the curves changing from blue to yellow to red). This is more clearly seen in the inset, which shows the normalized absorption at three different wavelengths. The absorption at the chosen wavelengths all decrease over time, corresponding to conversion of the DHP state to the CPD state.

In order to see if this transition is reversible by illumination with UV radiation, another set of optical experiments was done. The molecule was stored in the dark to allow thermal relaxation to the DHP state. Subsequently, the solution was illuminated by a mercury arc lamp (100 W) with a high-pass filter at 400 nm, only allowing larger wavelengths to pass. The spectrum of the light source can be seen in Fig. 6.5, including the two used filters (high-pass and low-pass). At the start of the experiment, and successively after every ten minutes, the light source was turned off and the absorption spectrum was measured using the tungsten light source. After taking one spectrum, the tungsten light source was turned off, and illumination with the Hg source was resumed

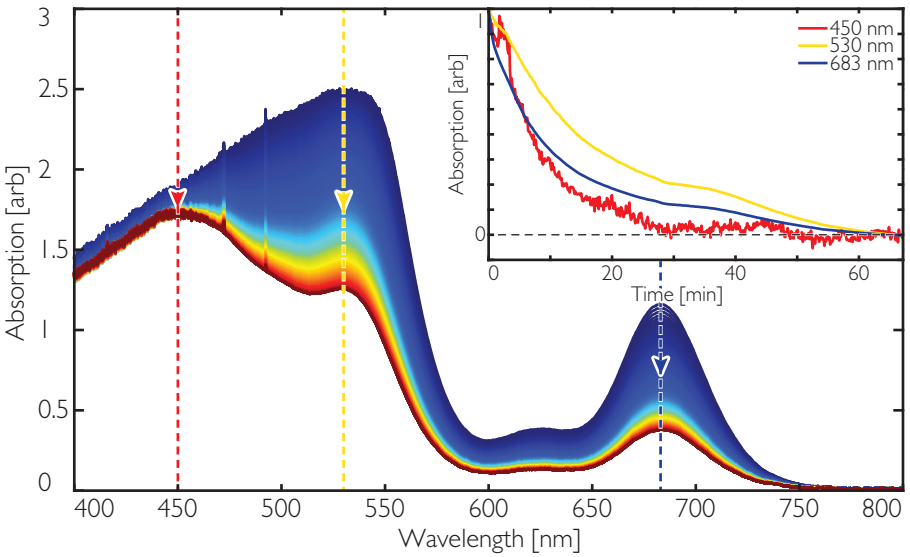

Fig. 6.4: Change over time in the absorption spectrum of DHP dissolved in acetonitrile at 25 °C. Blue is the first absorption curve, red shows the spectrum after 67 minutes. The inset shows the normalized absorption at 450 nm, 530 nm and 683 nm (indicated by the lines of the same color in the spectrum) over time. The curves are normalized to the absorption at the respective wavelength at $t = 0$ and $t = 67$ min. The decrease in the absorption corresponds to conversion from the closed DHP state to the open CPD state, caused by illumination by the tungsten light source used to measure the spectrum. The absorption below 450 nm could not be measured accurately, as the intensity of the light source at these wavelengths is too low to give reliable data.

After this experiment, the high-pass filter was replaced by a low-pass filter, only allowing wavelengths smaller than 450 nm to pass[‡], and the experiment was repeated. As visible light causes the DHP → CPD transition, and UV radiation causes the CPD → DHP transition, we expect to see a decrease in absorption during the first experiment, and an increase in absorption during the second. This is exactly what can be seen in Fig. 6.6.

[‡] The low-pass filter becomes transparent again above 630 nm. However, the intensity of the light source is low at these wavelengths, and we found that it does not interfere with the CPD → DHP transition.

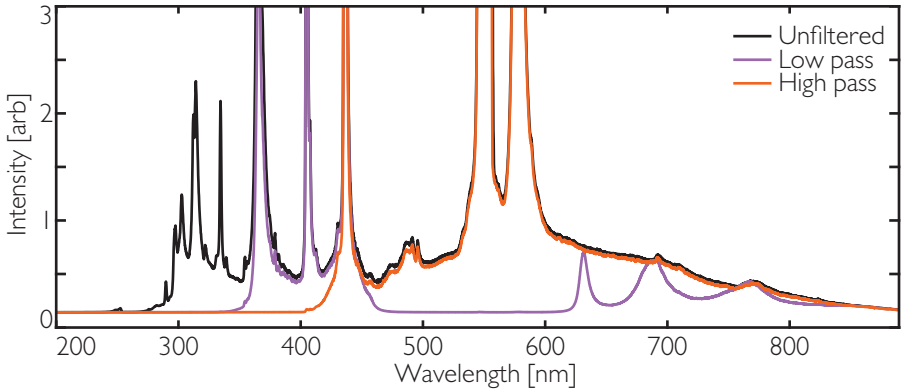

Fig. 6.5: Optical spectra of the Hg light source, black shows the unfiltered source, red shows the high-pass filtered source, and purple shows the low-pass filtered source. The high-pass filter starts transmitting above 400 nm, whereas the low-pass filter becomes transparent below 450 nm. Moreover, the low-pass filter again becomes slightly transparent above 630 nm. We found that the transmission at these wavelengths do not significantly affect our results.

The left figure shows the absorption spectra of the first experiment, where the inset shows the change in absorption over time at the indicated wavelengths. The right figure shows the results of the second experiment. As expected, illumination with long-wavelength light shows a decrease in absorption, agreeing with the DHP $\rightarrow$ CPD transition, whereas illumination with short-wavelength light shows the reverse. Moreover, the switching in either direction is very fast, as most of the conversion is already complete before the second measurement.

These results show that this particular batch of molecules indeed show reversible switching behavior, and that the switching can be controlled by illumination with a chosen frequency of light. In order to confirm that the switches can be incorporated into a network of nanoparticles, an array was stamped on a glass substrate. The transparent glass substrate allowed us to measure the UV-VIS transmission through the network. The absorption before exchange and after exchange was measured, the results of which can be seen in Fig. 6.7.

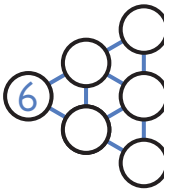

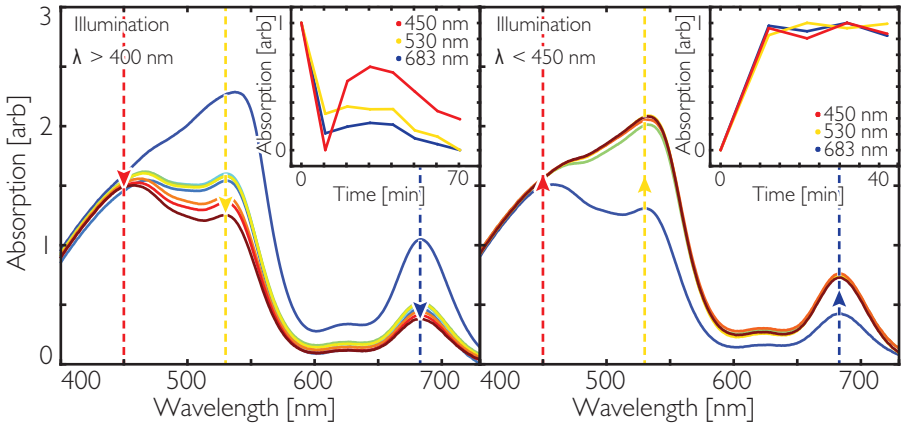

Fig. 6.6: Change over time in the absorption spectra of the switch dissolved in acetonitrile at 42 °C. Progression of time is indicated by change in color of the curves from red to blue, the inset shows normalized absorption over time at chosen wavelengths. In the left figure, the solution is illuminated by the Hg light source using the high-pass filter, on the right, the low-pass filter is used instead. Left plot shows that the absorption decreases over time, corresponding to the DHP → CPD, obtained when illuminating with long wavelengths (> 400 nm). We attribute the dip in the first and second measurement points to a misalignment of the fiber optic cable. The right plot shows an increase in absorption, indicating the reverse transition upon illumination with short wavelengths (< 450 nm).

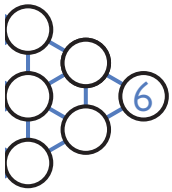

As can be seen in the figure, molecular exchange shifts the absorption peak by 10 nanometers and also broadens it. This indicates that exchange on this sample is indeed successful and that the switches are present in the network.

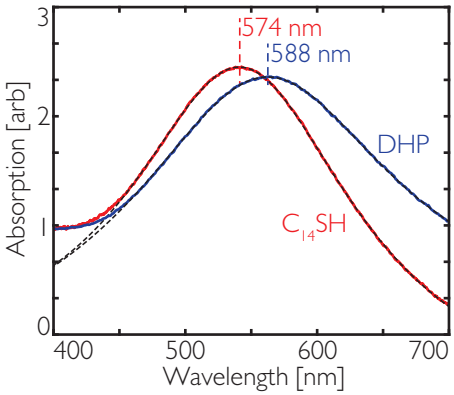

Fig. 6.7: Absorption spectra of the nanoparticle array before (red) and after (blue) exchange with the DHP based molecular switch, the black dashed lines show the Lorentzian fits. The absorption peak shifts by almost 10 nanometers after exchange and also increases in width. Both of these factors indicate successful insertion of the molecules.

6.5 Initial results in dark environment

Prior to exchange, the IV behavior was checked at room temperature in a probe station to ensure that fabrication was successful. After exchange, the one-volt resistance of the network changed from 10 GΩ to 100 kΩ, indicating successful crosslinking of the nanoparticles. This was followed by investigation at variable temperatures in a dark environment, the results of which can be seen in Fig. 6.8.

As the room temperature conductance of the network is large ($\approx 30\,\mu S$), we assume that the molecule is initially in the DHP state and did not switch during transfer to the cryostat. The current is similar to the post-exchange result obtained in the previous chapter, albeit roughly an order of magnitude smaller. Fits using the new model can be found in Fig. F.1 in the appendix.

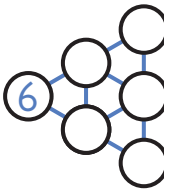

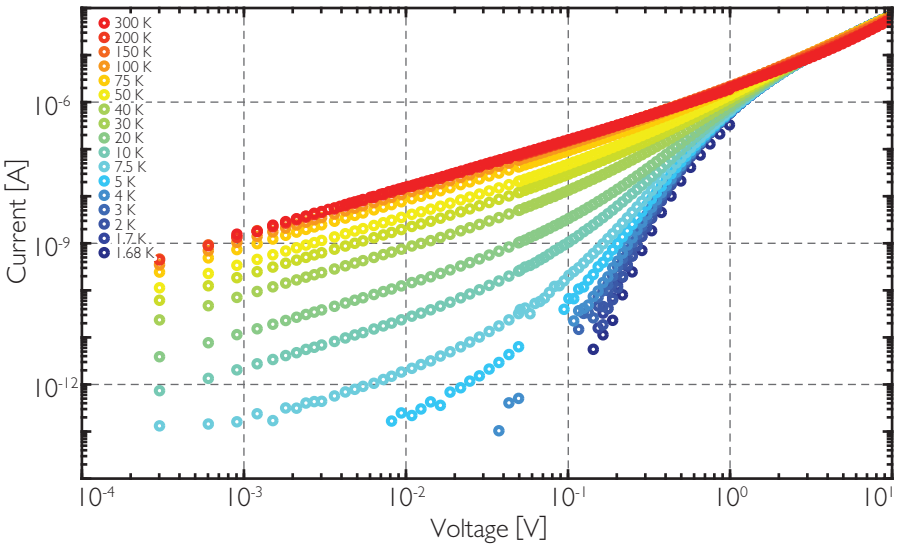

Fig. 6.8: Current versus voltage plots of a nanoparticle network interlinked by molecular switches at various temperatures, plotted on a double-log scale. The data points below the noise floor were removed by hand. The IV curves are similar to those observed in the previous chapter, indicating successful insertion of the switches into the array. See appendix F for fits to these curves using our alternative model.

6.6 Effect of light at constant temperature

In order to check the switchability of the network interconnected by the molecular switches, the sample was heated to room temperature under helium atmosphere inside the cryostat. As the insert was fitted with a fiber optic cable, we were able to illuminate the sample *in situ* using various light sources. The resistance at 1 V was measured over time and the sample was illuminated with the mercury light source using the high-pass filter. This should initiate the DHP → CPD transition, causing an increase in resistance. Fig. 6.9 shows the one-second averaged resistance versus time.

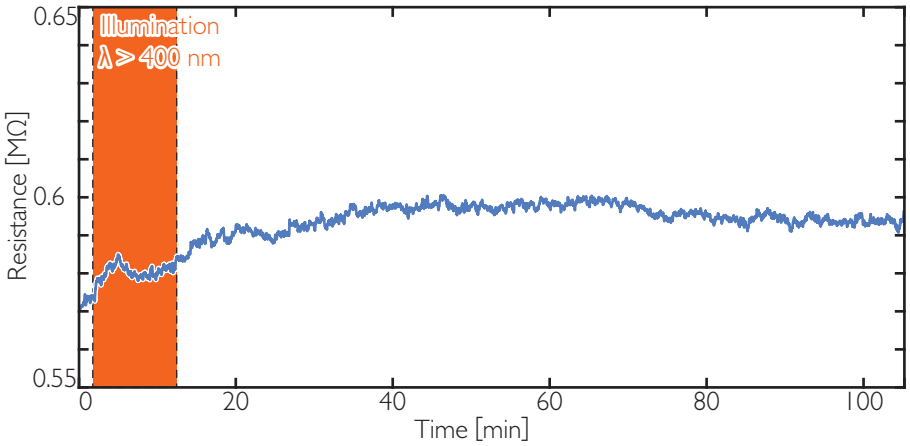

Fig. 6.9: One-second averaged resistance at 1 V of the nanoparticle network interconnected by molecular switches at room temperature versus time. The sample was illuminated using a mercury light source through a high pass (> 400 nm) filter during the time indicated by the orange window. The illumination should facilitate the DHP → CPD transition, corresponding to a decrease in resistance of four order of magnitude. However, no significant change is observed.

The illumination was started after 120 seconds and stopped after 800 seconds, as indicated by the orange window. From Fig. 6.6, left plot, we expect that the conversion should be almost complete after 600 seconds. However, during this time, no significant change in resistance is observed. If all molecules were in the DHP state before the measurement, illumination should trigger the DHP → CPD transition, which is paired with an increase in resistance. However, if the molecules are already in the CPD state, the resistance should not change. Therefore, the observation that the resistance does not change might indicate that all molecules are already in the CPD state, not allowing further switching. To check if this is indeed the case, a second measurement was done, this time illuminating using a low-pass filter, allowing only high energy light to pass. The results can be seen in Fig. 6.10.

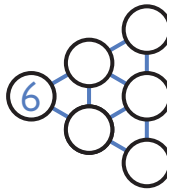

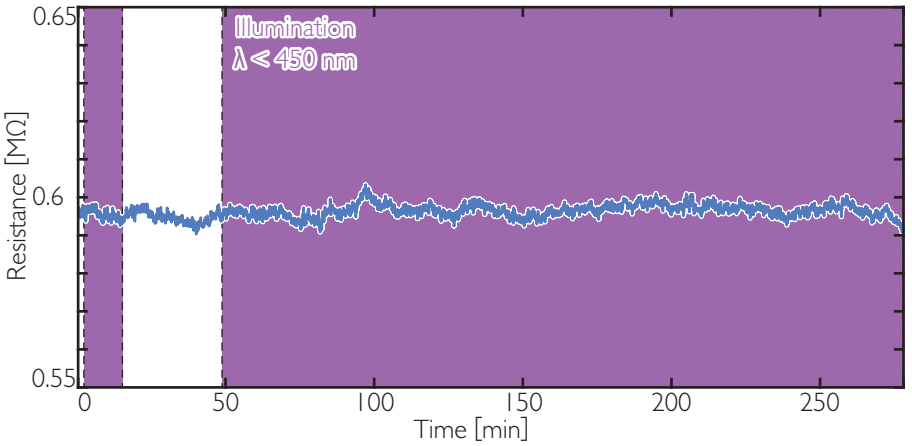

Fig. 6.10: One-second averaged resistance at 1 V of the nanoparticle network interconnected by molecular switches at room temperature versus time. The sample was illuminated using a mercury light source through a high pass (> 400 nm) filter during the entire measurement. The illumination should facilitate the DHP → CPD transition, corresponding to an increase in resistance of four order of magnitude. Even after 900 minutes, no significant change in resistance is observed.

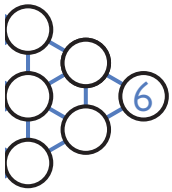

Illumination was started after 120 seconds and stopped after 830 seconds, indicated by the first purple window. During illumination, there is no significant change in the resistance. This is confirmed by the trend in the resistance without illumination, indicated by the white window. We found earlier that the switches should complete the CPD → DHP transition within ten minutes. However, as the environment might affect the transition rate, we again start the illumination after 50 minutes, in order to see slower changes in the resistance. However, even after three hours of illumination, no change in the resistance was observed.

As the DHP → CPD transition might also be slower when the switch is integrated in a nanoparticle network, we change the filters in order to illuminate only with a wavelength larger than 400 nm, identical to the experiment from Fig. 6.9. However, we now illuminate for 15 hours to ensure that even a slower transition rate is captured. The results of this can be seen in Fig. 6.11.

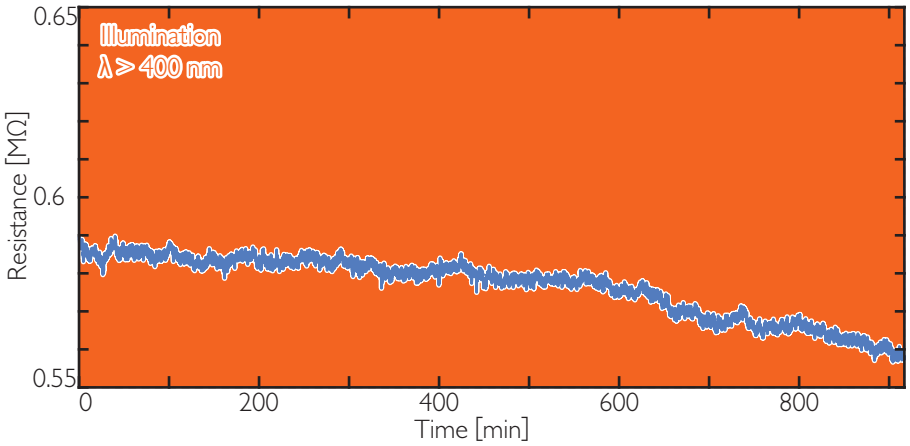

Fig. 6.11: One-second averaged resistance at 1 V of the nanoparticle network interconnected by molecular switches versus time. The sample was illuminated using a mercury light source through a low pass (< 450 nm) filter during the time indicated by the purple windows. The illumination should facilitate the CPD → DHP transition, corresponding to an increase in resistance of four order of magnitude. However, no significant change is observed.

Although the resistance changes slightly over the course of 900 minutes, no clear switching is observed. As illumination at these wavelengths should facilitate the DHP → CPD transition, we expect to see an increase in resistance of four order of magnitude, which is clearly not observed.

To summarize: neither illumination with large, as with small wavelengths results in a change in resistance, even after extended periods of illumination. This could be due to several reasons. The first of which is the absence of the molecule itself. If molecular place-exchange was unsuccessful, illumination should not have any effect.

In order to study if the molecules are present, we measured the optical spectra before and after exchange. We saw a clear change between the pre-exchange and the post-exchange spectra in Fig. 6.7, indicating that exchange was indeed successful. Moreover, exchange was paired with a change in resistance, supporting this conclusion. Additionally, we used Raman spectroscopy (facility at Dublin City University, group of Prof. Tia Keyes) to determine the presence of the switches. However, the measured signal was too low to provide a definite conclusion.

If the molecule is indeed present, it could be that the molecule is chemically pacified. As the CPD state of the molecule is very sensitive to oxygen, it could be that the presence of oxygen during sample transfer has caused the molecule to react with it. However, this requires the molecule to be in the CPD state, which requires prolonged illumination (≈ 10 min). Transfer was done at night where illumination in contact with oxygen was only

by the dim light of an LCD computer monitor and took no longer than a minute. These conditions should be insufficient to realise the DHP → CPD transition.

Moreover, chemically bonding the molecule to the gold nanoparticles could alter the electronic structure of the molecule. These effects are not uncommon, and as we saw in chapter 1, can indeed prohibit switching in molecules. Alternatively, as the switching requires an electronically excited transition state, this excited state can lose its energy to the surrounding nanoparticles, pacifying the switch. Vice versa, the nanoparticles could be optically excited and transfer the excitation to the molecules. In our system, it could be that the excitation is quenched by the nanoparticles, preventing the molecules from switching.

6.7 Conclusion

We attempted to explore the enhancement of the ON-OFF ratio of nanoparticle networks interlinked with molecular switches. We predict that this ratio should increase with decreasing temperature, due to a change in E_C of the nanoparticles between the ON and OFF states. To experimentally confirm this, we fabricated a nanoparticle network interlinked by trans-10b,10c-dimethyl-10b,10c-dihydropyrene, a molecule that can switch between two resistance states upon irradiation with visible light (ON → OFF) or UV radiation (OFF → ON). Although we observed reversible switching of the molecule in solution and also found a change in SPR frequency and resistance after molecular exchange (indicating successful insertion of the molecule), we observed no change in the resistance of the interlinked network. Neither UV radiation or visible light had a significant effect, even after prolonged illumination.

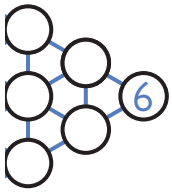

Although the exact cause of this is unclear, it might be due to passivation of the functionality of the molecule due to chemical bonding with the nanoparticles. This chemical bond might allow the excited transition state to be quenched due to interaction with the nanoparticles. As the length change of the molecule upon switching is negligible, mechanical inhibition of the switch is not expected. Future experiments involving the same molecule should rule out these predictions, possibly by directly measuring switching in a MCBJ while the molecule switches when connected, directly observing the switching. Moreover, other tried and tested molecules, such as diarylethylenes[2] might provide a better alternative to the molecule used in this research.

References

[1] Jean-Francois Dayen, Edwin Devid, Mutta Venkata Kamalakar, Dmitry Golubev, Constant Guédon, Vina Faramarzi, Bernard Doudin, and Sense Jan van der Molen. Enhancing the Molecular Signature in Molecule-Nanoparticle Networks Via Inelastic Cotunneling. *Advanced Materials*, 25(3):400–404, 2013.

[2] Sense Jan van der Molen, Jianhui Liao, Tibor Kudernac, Jon S. Agustsson, Laetitia Bernard, Michel Calame, Bart J. van Wees, Ben L. Feringa, and Christian Schönenberger. Light-Controlled Conductance Switching of Ordered Metal−Molecule−Metal Devices. *Nano Letters*, 9(1):76–80, 2009.

[3] Sense Jan van der Molen and Peter Liljeroth. Charge transport through molecular switches. *Journal of Physics: Condensed Matter*, 22(13):133001, 2010.

[4] John R. Rumble. *CRC Handbook of Chemistry and Physics*. CRC Press, 2027.

[5] Diana Dulić, S. J. van der Molen, T. Kudernac, H. T. Jonkman, J. J. D. de Jong, T. N. Bowden, J. van Esch, B. L. Feringa, and B. J. van Wees. One-Way Optoelectronic Switching of Photochromic Molecules on Gold. *Physical Review Letters*, 91(20), 2003.

[6] Diego Roldan, Veerabhadrarao Kaliginedi, Saioa Cobo, Viliam Kolivoska, Christophe Bucher, Wenjing Hong, Guy Royal, and Thomas Wandlowski. Charge Transport in Photoswitchable Dimethyldihydropyrene-Type Single-Molecule Junctions. *Journal of the American Chemical Society*, 135(16):5974–5977, 2013.

[7] Wenjing Hong, David Zsolt Manrique, Pavel Moreno-García, Murat Gulcur, Artem Mishchenko, Colin J. Lambert, Martin R. Bryce, and Thomas Wandlowski. Single Molecular Conductance of Tolanes: Experimental and Theoretical Study on the Junction Evolution Dependent on the Anchoring Group. *Journal of the American Chemical Society*, 134(4):2292–2304, 2012.

[8] Diego Roldan, Saioa Cobo, Frédéric Lafolet, Neus Vilà, Constance Bochot, Christophe Bucher, Eric Saint-Aman, Martial Boggio-Pasqua, Marco Garavelli, and Guy Royal. A Multi-Addressable Switch Based on the Dimethyldihydropyrene Photochrome with Remarkable Proton-Triggered Photo-opening Efficiency. *Chemistry - A European Journal*, 21(1):455–467, 2015.

[9] Saioa Cobo, Frédéric Lafolet, Eric Saint-Aman, Christian Philouze, Christophe Bucher, Serena Silvi, Alberto Credi, and Guy Royal. Reactivity of a pyridinium-substituted dimethyldihydropyrene switch under aerobic conditions: self-sensitized photo-oxygenation and thermal release of singlet oxygen. *Chemical Communications*, 51(73):13886–13889, 2015.

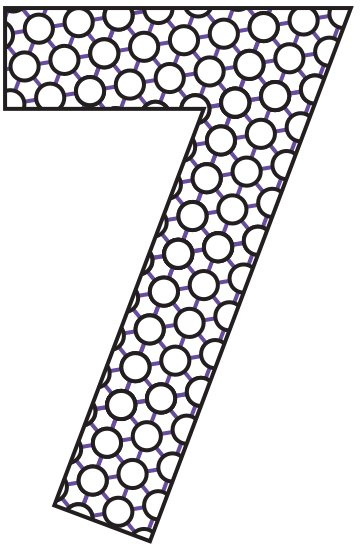

LEEM-POTENTIOMETRY ON GOLD NANOPARTICLE NETWORKS

7.1 Introduction

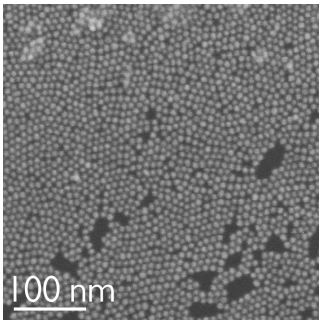

Fig. 7.1: SEM image of a nanoparticle network. The individual nanoparticles are ≈10 nm in diameter.

Elucidating the nanoscopic structure of nanoparticle networks is important when studying the electronic properties of these networks. Although electronic measurements at varying temperatures give a lot of information (as seen in the previous chapters), they do not always provide a complete picture. For example: unusually high device resistances could be due to high contact resistances, network inhomogeneities or even the absence of large parts of the network. Optical microscopy can usually provide information about the latter case, as its resolution is good enough to see the presence of a network on the micrometer scale. To study the homogeneity of the network on the smaller scale, SEM (Scanning Electron Microscopy) is ideal, since it provides the high resolution required to see individual nanoparticles, as seen in Fig. 7.1. The downside of SEM is that the electrons typically have energies of around 20 keV, which transforms any organic residue on the network (such as alkanethiols) to graphitic carbon (paired with a change in contrast), changing the network irrevocably.

Low Energy Electron Microscopy or LEEM is an imaging technique that uses electrons with an energy of only a few eV. Electrons at these low energies lack the 'oomph' required to damage the sample. Furthermore, the low energy electrons are very sensitive to local (applied) potentials, making it possible to sense these. LEEM therefore does not only provide structural information, it also provides electronic information on the nanoscale, making it an ideal technique for the study of nanoparticle networks*.

7.2 Low-Energy Electron Microscopy

LEEM is similar to optical microscopy, in that a sample is illuminated by a source, and that the intensity reflected by the sample is observed. The difference is that in the case of LEEM, the source is not a photon emitter, but an electron gun. Furthermore, LEEM is similar to TEM because the area of interest is illuminated simultaneously, i.e. it is not a scanning technique like Scanning Electron Microscopy or Scanning Tunneling Microscopy. The specific LEEM used in this chapter is the ESCHER setup[1,2] (see Fig. 7.2).

In this setup, the electrons are accelerated to 15 keV after leaving the gun, deflected by a prism and rapidly decelerated by 15 keV between the objective lens and the sample. In order to achieve this, the gun as well as the sample are held at the same potential of -15 kV (the

*The surface sensitivity can also be detrimental, as any organic residue present on the surface of the network can have a large effect on the image quality.

potential of the sample can be varied slightly, as explained later in this chapter), whereas the rest of the machine is grounded. After hitting the sample, the reflected electrons are accelerated back to the prism and deflected to the second prism. After the second prism, the electrons are corrected for the lowest order aberrations of the objective lens and sample[3]. This correction is done by an electrostatic mirror. The electrons are then accelerated back to the prism array, deflected downwards where they hit the detector.

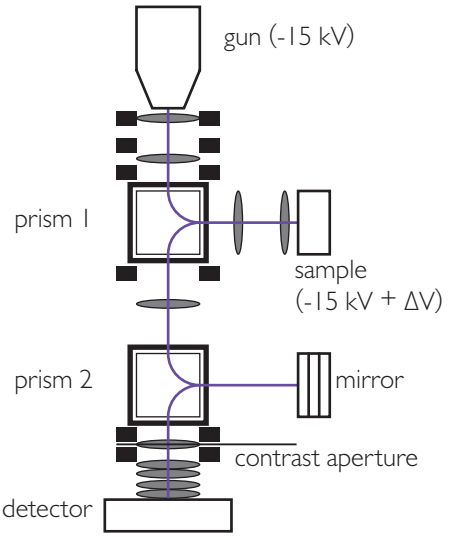

Fig. 7.2: Schematic picture of the ESCHER LEEM setup. Electrons leave the gun with 15 keV, are deflected by the prism and slowed down to a few eV before hitting the sample. They are then accelerated backwards, are deflected downwards by the prism and deflected again by the second prism to the mirror for aberration correction. After hitting the mirror, they are accelerated backwards and finally deflected to the detector where they are absorbed.

Using aberration correction, the ESCHER microscope can achieve a lateral resolution down to 1.4 nm[2]. Since the electron gun is always held at -15 kV, the electron landing energy can only be changed by changing the potential of the sample. The landing energy is given by:

$$E_{\mathrm{L}} = e\Delta V + \Delta\Phi, \qquad (7.1)$$

where ΔV is the difference in potential between the gun and the sample ($\Delta V = V_{\mathrm{S}} - V_{\mathrm{G}}$) and $\Delta\Phi$ is the difference in work function between the gun and the sample ($\Delta\Phi = \Phi_{\mathrm{S}} - \Phi_{\mathrm{G}}$).

Since V_{S} can be controlled, E_{L} is a tunable parameter. At low electrostatic potential of the sample, $E_{\mathrm{L}} < 0$ and the incoming electrons do not have enough energy to reach the sample and are simply reflected. Upon increasing the sample potential such that $E_{\mathrm{L}} = 0$, the electrons have just enough energy to graze the sample before being accelerated back to the detector. This is called the mirror mode transition, which is a very important concept in the next section. When the potential of the sample is further increased, $E_{\mathrm{L}} > 0$, and the electrons can reach the sample and interact with it before being reflected or absorbed. The elastically backscattered electrons are then detected. This process of increasing the landing energy can be seen in Fig 7.3, which shows images for different landing energies. Since the penetration depth depends on electron energy[4], this depth can be tuned. As the landing energy increases, more electrons are lost to scattering and are not detected since we measure in bright-field mode. This results in the general trend of lower intensity at higher energy.

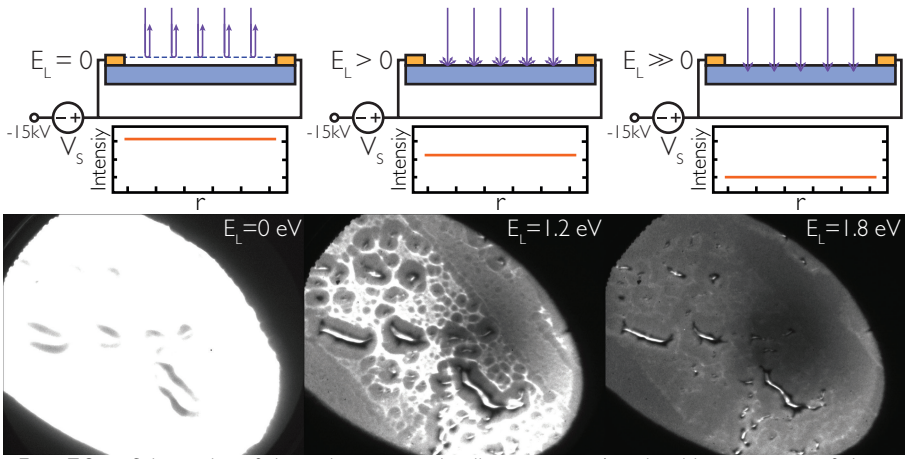

Fig. 7.3: Schematic of intensity versus landing energy (used with courtesy of Jaap Kautz[5] (edited)) above the corresponding bright field LEEM images of a nanoparticle network with holes for changing electron landing energies. Left is lower landing energy, right is higher landing energy. The contacts on the network can be seen in the lower left and upper right corners of the middle picture and have an interelectrode spacing of 5 µm. Left image: landing energy is close to zero and the mirror mode transition occurs, allowing the electrons interact with the sample. Center image: landing energy is larger than zero, electrons interact with the sample before reflecting and a clear image is formed. Right image: landing energy is much larger than zero. Inelastic scattering inside the sample, but also elastic scattering with large angles causes fewer electrons to reach the detector, resulting in a darker image.

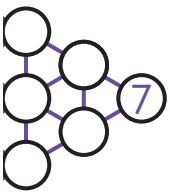

In LEEM, a plot of reflected electron intensity versus landing energy is called a LEEM-IV curve†. The exact shape of this LEEM-IV curve holds a lot of information about the structure of a sample, as this structure determines whether an electron with a certain energy is reflected or absorbed. Graphene for example has different IV-curves for monolayers and bilayers/multilayers[6]. This means that the thickness of graphene flakes can be measured with nanometer lateral resolution. Moreover, since LEEM uses low energy electrons, a small change in surface electrostatic potential can already have a significant effect on the electron landing energy. Using these effects to determine the potential will be discussed in the next section.

† It is interesting to note here that in LEEM literature, these measurements are also referred to as IV-curves, as one measures the reflected electron intensity -and thus current-as a function of electron energy, and thus voltage on the sample

7.2.1 Potentiometry

When a voltage bias is applied across a nanoparticle device (or across an object in general), the potential drop is not necessarily homogeneous and linear. Local imperfections and defects alter the current path across the sample and hence the local potential drop. Inversely, this means that studying these local drops in potential can give information about the structure of the sample. Locally sensing the potential is called potentiometry. In nanoparticle arrays, potentiometry can for example elucidate poor nanoparticle cluster connectivity, or even favored percolation paths across the array. Potentiometry is not a new technique; it has for example been possible to sense local potentials with probe microscopy using a technique called Kelvin Probe Microscopy[7]. This technique uses active feedback of the current between the sample and tip of an atomic force microscope (AFM) to determine the work function and potential.

In LEEM, the electron landing energy depends greatly on the local potential $V_{\mathrm{P}}(\vec{r})$, in the sample. If a voltage V_{bias} is applied across a sample in the LEEM Eq. 7.1 changes to:

$$E_{\mathrm{L}} = e\Delta V + \Delta\Phi + \mathrm{eV_P}\left(\vec{r}, V_{\mathrm{bias}}\right). \tag{7.2}$$

This means that the mirror mode transition ($E_{\mathrm{L}} = 0$) now no longer occurs when $e\Delta V = -\Delta\Phi$, but when $e(\Delta V + V_{\mathrm{P}}(\vec{r})) = -\Delta\Phi$. The voltage drops from one side of the sample to the other, and the mirror mode transition now 'shifts' across the sample as the incoming electron energy is increased, seen in Fig. 7.4.

Since the mirror mode transition shifts in energy when the local potential is taken into account, this shift can be related to the value of the local potential. From Eq. 7.2, it can be seen that ΔV changes by exactly $-V_{\mathrm{P}}(\vec{r})$ compared to the situation with no local potential. By fitting the LEEM-IV curves without an applied potential across the sample to the case with the applied potential, the shift can be determined and related to the local potential[8]. Moreover, if there are clear features in the LEEM-IV curve, a mirror mode transition is not needed to obtain the local potential. The local potential can then be measured with great accuracy, almost down to nanometer resolution[6].

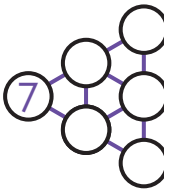

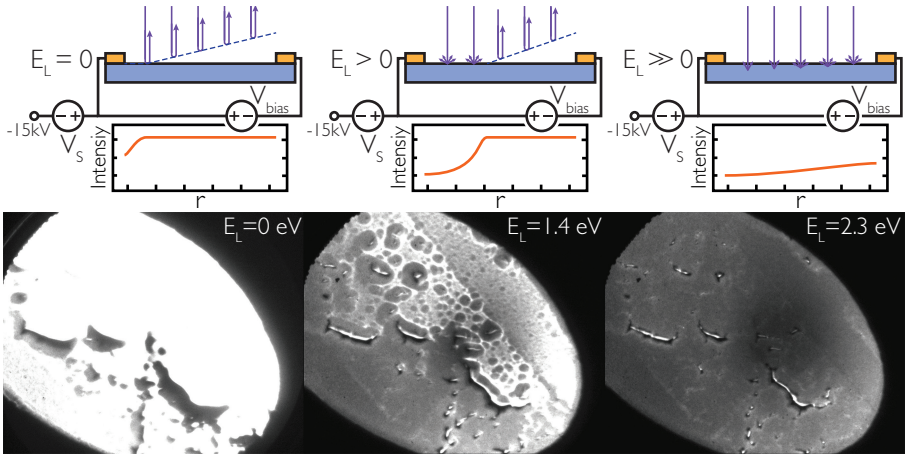

Fig. 7.4: Schematic of intensity versus landing energy above a LEEM image of a nanoparticle network, analogously to Fig. 7.3. However, in contrast to Fig. 7.3, there is an applied potential across the nanoparticle network. Left image: landing energy is close to zero and the mirror mode transition occurs, allowing the electrons interact with the sample. Due to a potential drop across the cracks in the network, the image is distorted slightly in this region. Center image: landing energy is larger than zero for the bottom left of the array, but still around zero for the top right part of the array. Electrons on the bottom left interact with the sample, but the top right electrons are reflected before hitting the sample. The transition between these two regions defines an equipotential line. Right image: landing energy is much larger than zero, but still differs across the array. In the bottom left, the image is different from the top right, as on the top right, a lacy network can be seen, which is not visible on the bottom left. This is likely due to the energy dependent interaction depth of the electrons varying across the sample.

7.3 Experimental methods

7.3.1 Sample preparation

Nanoparticle networks were prepared analogously to described in chapter 4 and stamped on lithographically defined gold contacts on a Si/SiO_2 substrate. This was followed by exchange with OPE3 molecules to increase the conductance of the network, allowing the electrons from the LEEM to flow out easily without charging the network significantly. Additionally, since LEEM is very sensitive to surface contamination, an extra step was taken to remove as much organic residue as possible. Unfortunately, gold nanoparticle networks are fragile and cannot withstand harsh cleaning techniques. To allow the evaporation of any organic molecules (such as the unbound (physisorbed) thiols left after exchange), the sample was kept in vacuum (10^{-7} mbar) for two weeks. Although the optimal resolution of 1.4 nm was not reached, this turned out to be good enough for low resolution imaging and

potentiometry.

7.3.2 Measurement technique

To obtain the local potential in the nanoparticle networks, it is first imaged without any applied potential. This imaging consists of measuring the reflected electron intensity as a function of incoming electron energy. In effect, this results in taking a LEEM-IV at every pixel of the image.

After these reference images have been taken, a potential is applied across the network. This potential locally changes the electron landing energy, and therefore causes a shift of the IV-curve by exactly the local potential. By measuring a LEEM-IV with this applied potential and fitting the reference IV-curve to it, the shift is determined. It should be noted that the shift in the LEEM-IV is exactly the opposite of the local potential, as can be seen from Eq. 7.2 in the case where $E_L = 0$. In principle, the best fit can be obtained by taking a reference curve for every pixel and fitting it to the potentiometry data. Due to technical limitations, a single reference curve is used. Since the local LEEM-IV changes slightly from position to position, even in the unbiased case, this results in some fitting errors, which are shown in the next section. It should still be noted however, that although there are slight differences in the local IV curves, the general features such as the mirror mode transition are similar across the entire network.

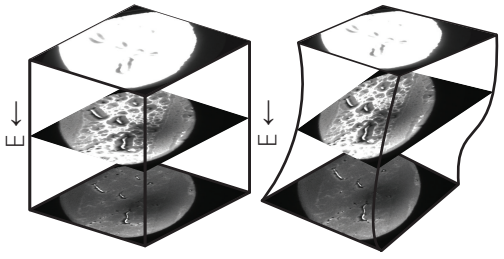

Fig. 7.5: LEEM images as a function of electron landing energy, lower pictures are higher landing energies. The left image shows the ideal situation without any distortions. The right image shows possible distortions. Not only is there an overall drift, the drift is inhomogeneous. Furthermore, due to local potentials, the landing energy varies across the sample, represented by the tilting of the images. Local distortions are not shown on this image.

Ideally, applying a potential across the array only results in a shift of the LEEM-IV. However, as is usually the case in physics, the practical situation is far from the ideal one. The applied potential does not only result in a change in landing energy, but also causes lateral electric fields. At high electron energies where $E_L \gg eV_P$, these fields can be ignored, but at electron landing energies around the mirror mode transition, they cannot. At these low energies, these fields cause a significant shift of the image, resulting in distorted images, shown schematically in Fig. 7.5. Most of the distortion consists of a shift of the image as a function of electron landing energy. This drift means that the LEEM-IV is not taken from a single

spot on the image, but of a spot that shifts as a function of energy. Using image processing, the data can be mostly corrected for this drift. However, drift is not the only distortion to take into account. Cracks in the nanoparticle network cause significant potential drops over small distances, resulting in large local electric fields. These local fields deflect the incoming electrons. Furthermore, this deflection depends on the electron landing energy, with larger deflections at lower landing energies. This makes intuitive sense, as lower energy electrons move more slowly and spend more time in the deflecting field. Moreover, cracks or holes in the network reveal the underlying silicon oxide which shows charging in LEEM, contributing to the deflection. These local deflections usually only affect the dataset locally and do not change the overall result. The effects of these local deflections can be seen as local spots of higher/lower potential in the potentiometry map and will be discussed in the next section.

7.4 Results and discussion

Using LEEM, we now compare two areas of a gold nanoparticle network. Before applying a voltage across the network, a reference LEEM-IV curve is taken at every pixel of the image of the network. The network is then biased with +1 V and the process is repeated, yielding two IV curves for every pixel. Fig. 7.6 shows a LEEM image of area 1 with the LEEM-IV curves (continuous) compared to the reference curves (dashed) at four different locations. It is worthwhile to note here that the electron landing energy is not set directly, only the sample potential (V_S in Fig. 7.4). The landing energy scale has been shifted artificially to let the mirror mode transition of the red location occur at $E_L = 0$. The bottom left electrode is grounded, whereas the top right electrode is elevated to +1 V.[‡]

From the IV curves, it can be seen that the mirror mode transition does not shift on the blue and green locations, indicating that the local potential doesn't change significantly. This is in accordance with expectations, as the lower left electrode is grounded. The IV curves in the yellow and red locations do shift by roughly 1 eV, indicating a local potential of +1 V at both locations.

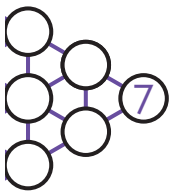

In order to study this further, we now fit the shift of the IV curves to the reference data at every pixel and produce a potential map of the network. The process is schematically depicted in Fig. 7.7, the left image shows a SEM picture of the network, the middle shows a LEEM image, and the full potentiometry map is shown on the right. Fig. 7.9 shows the potential map of area one overlaid on a SEM image. In order to correct for distortions, the potential map is slightly deformed in order to overlap completely with the SEM image. (The original SEM image, as well as the LEEM image and the potential map can be seen in Fig. 7.7.) An interesting feature is the rapid change in potential in the top right corner, visible as a semicircular pattern. This is an artefact of the fitting algorithm, as these parts are not illuminated in the LEEM. A striking feature is that there is negligible voltage drop between

[‡] Interestingly, this ground is not a true ground, as the entire sample is lifted to -15 keV. To be more precise: bottom left electrode is lifted to -15 keV, whereas the top right electrode is lifted to -14.999 keV.

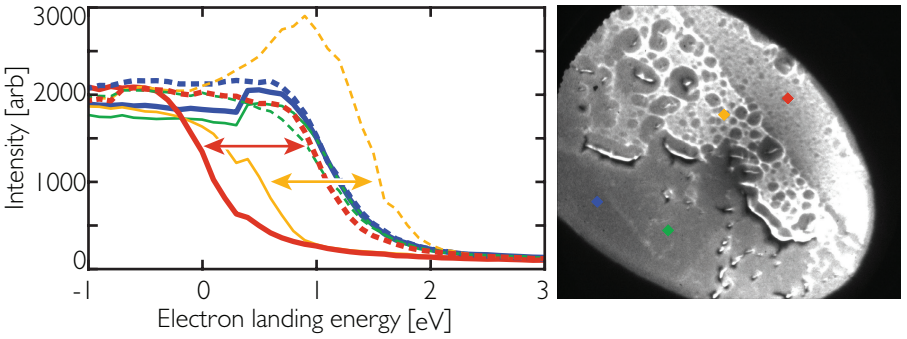

Fig. 7.6: LEEM-IV curves taken at different locations of the sample with and without an applied bias. The LEEM image of the applied bias case is shown. The dashed lines represent the reference situation without bias, continuous lines represent the situation with the top right electrode biased to 1 V. The induced potential shifts the yellow and red IV-curves by about 1 eV, whereas the blue and green IV curves remain approximately the same. This makes sense, since the lower left electrode is grounded. These IV-curves imply that the potential at the red and yellow sites, but also at the blue and green sites are equal. This suggests that there is a bad connection between these sites, supported by the cracks visible in the image.

the contacts and the network, implying a very low contact resistance. Furthermore, the map indeed shows that the voltage drop is small in the top right and bottom left, but large in between. The cause of these features can be clearly seen in the underlying SEM image. Large holes are present in the center of the device, but not near the contacts. The current is forced in between the small connections between the cracks, causing large potential drops in these areas.

This can be seen more clearly in Fig. 7.8, where the potential along three lines across the network has been plotted. The blue line does not cross any large cracks and has a roughly homogeneous potential drop. In contrast, the red and yellow lines both cross cracks in the network, which show large potential drops. These large voltage drops might have implications for electron transport in the Coulomb blockade regime.

As we saw in the previous chapter, transport in this regime is mostly facilitated by a few percolating paths. Increasing the voltage, increases the amount of paths contributing to the current. Therefore, having a large voltage drop in some areas might reduce the effects of disorder in E_C, as the voltage is enough to overcome the Coulomb barrier for these paths. On the other hand, these large voltage drops in some areas must be paired with smaller drops in others. Here, the effect of disorder might instead be larger. The effect of network quality on electron transport therefore is an interesting area for further research.

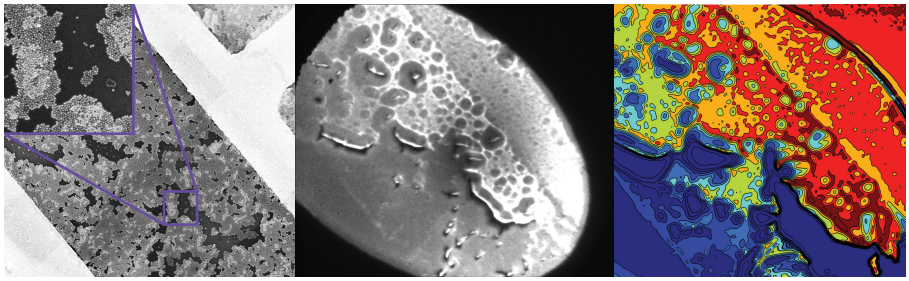

Fig. 7.7: Left: SEM image of the nanoparticle network, inset is roughly 1 μm^2. Center: LEEM image of the same area, a potential of +1 V is applied to the top right electrode. Right: potential map of the network. See Fig. 7.9 for a specification of the color scale.

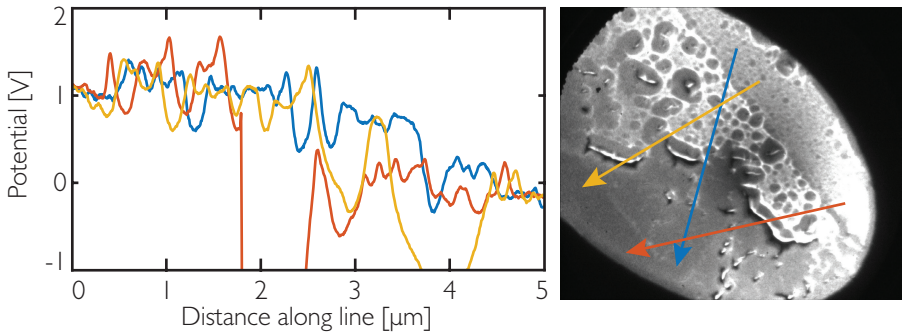

Fig. 7.8: Left: fitted potential versus distance along the line segment shown on the LEEM image on the right. The blue line does not cross any cracks in the network, and shows an approximately linear decrease in potential. In contrast, the red and yellow lines cross cracks, which show a significant potential drop. Furthermore, the fitting algorithm fails in these areas, showing a much lower potential due to distortions in the image.

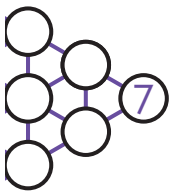

Fig. 7.9: LEEM-Potential map overlaid on a SEM image of area one, rotated 90 degrees counter-clockwise with respect to the previous images of this area. The colormap represents the fitted voltage. The electrodes can be seen in white. The top left electrode is grounded, whereas the other electrode is set at 1V. In contrary to area 2, a large crack in the network is present in the middle. A large potential drop is visible across this crack. This feature is enhanced even further by the fitting errors induced by electron deflection due to charging and lateral electric fields.

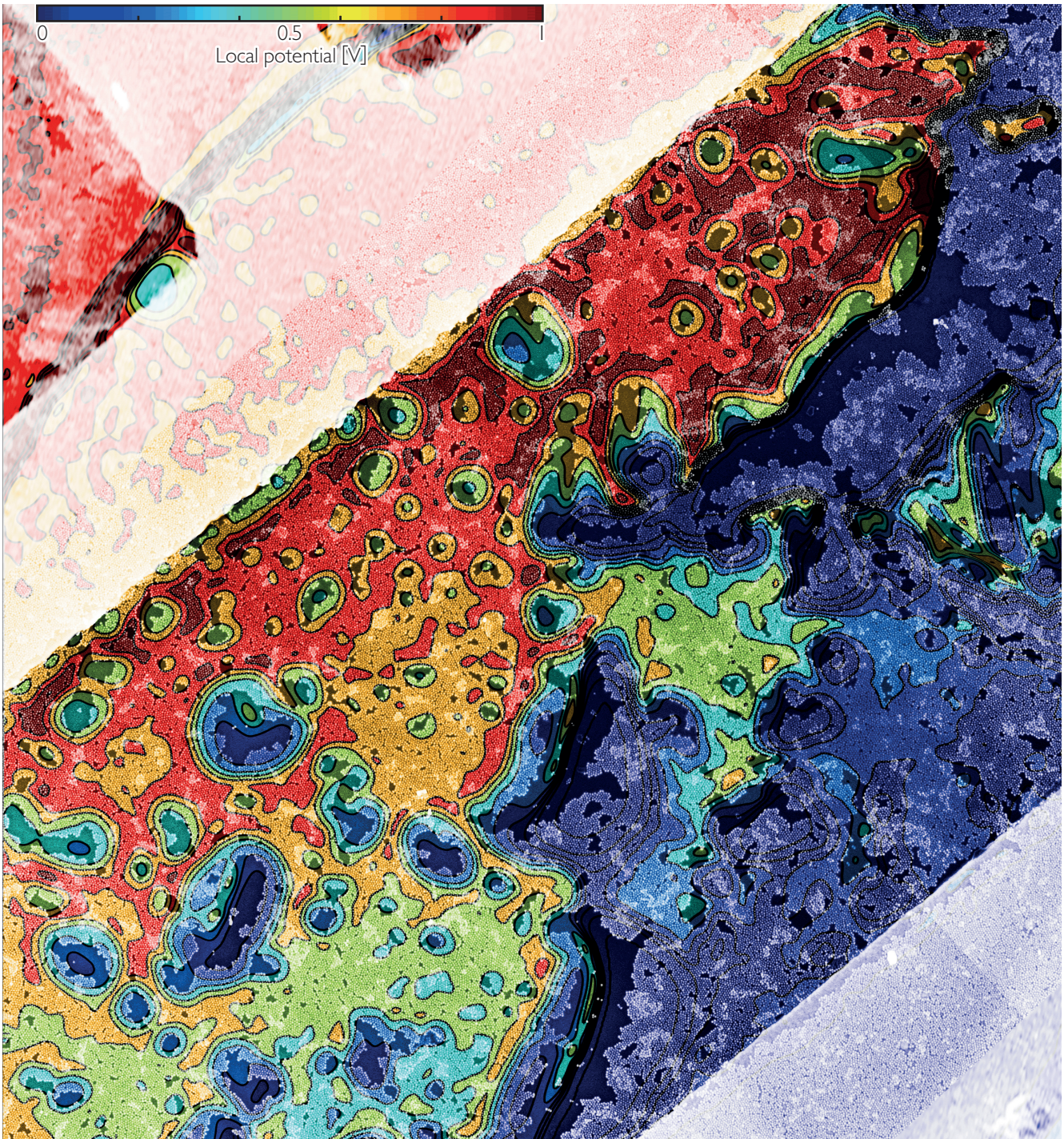

In addition to Fig. 7.9, we imaged a different area on the same device (henceforth labelled as area 2, with the previous named area 1). Unlike area 1, no reference images were taken, and the applied bias was raised to 2 V, instead of 1 V. An IV-curve was measured at every pixel of the network, four of which can be seen in Fig. 7.10. The space between the red and blue lines is roughly equal to 2 eV, in agreement with the 2 V of applied potential on the top right electrode. Interestingly, these IV-curves are roughly equally spaced, indicating a homogeneous potential drop across the array. This is in contrast to area 1, where the blue and green, and red and yellow IV-curves almost overlap. The homogeneity of the potential drop seems to indicate that this part of the network is of better quality than area 1.

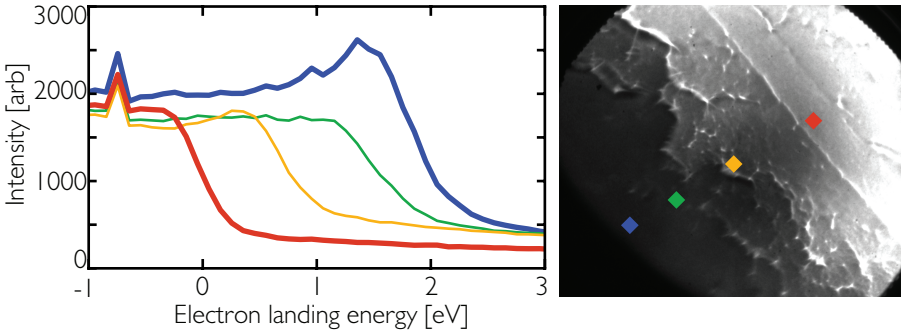

Fig. 7.10: LEEM-IV curves taken at different locations of area 2 of the nanoparticle network with an applied bias of 2 V. The LEEM image of the applied bias case is shown. No reference curves were measured for this area in contrast to area 1. The spacing between the red and blue curves is roughly 2 eV, in agreement with the 2 V applied bias on the top right electrode. Furthermore, the spacing between each curve is almost equal, indicating a homogeneous potential drop.

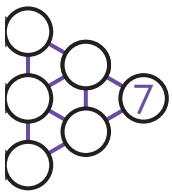

To further investigate the network quality, we now produce a potential map of area 2, analogous to area 1. The map overlaid on a SEM image can be seen in Fig. 7.12. Identical to in area 1, the rapid potential drop in the lower left corner is an artefact resulting from the fitting algorithm in an area that is not illuminated. The negligible potential drop between the network and the contacts seen in area 1 is also visible here. The potential drop across area 2 is more homogeneous than across area 1. The underlying SEM image shows why. Compared to area 1, area 2 has fewer and smaller holes. With the exception of these small holes, the network is continuous. This means that a current can easily flow around the holes and across the array. Although small potential drops are visible across the holes, this can also be partly due to an incorrect fit around the holes. Since the holes expose the insulating silicon oxide below, the charge built up here will deflect the incoming electrons, causing fitting errors in these regions. These features are supported by the potential curves shown in Fig. 7.11. Here, all lines show an almost linear decrease in potential along the line segment, the only exception being the middle of the yellow line, which crosses a crack in the network

around 2.5 μm.

An interesting feature (or absence of feature) is that grain boundaries in the network seemingly do not affect the potential drop. Moreover, no features that indicate percolation are visible in the potential map. This suggests that the electrical properties of nanoparticle networks are not extremely sensitive to irregularities and small holes. Areas where the networks looks roughly continuous are connected electrically. This is an important conclusion which supports the methods used in the previous chapters. It is also important to note that the device used in this chapter has an interelectrode spacing of 5 μm, an order of magnitude larger than the 500 nm used in chapter 6. With these smaller devices, the chance of an irregularity in the network significantly affecting the percolation is much lower.

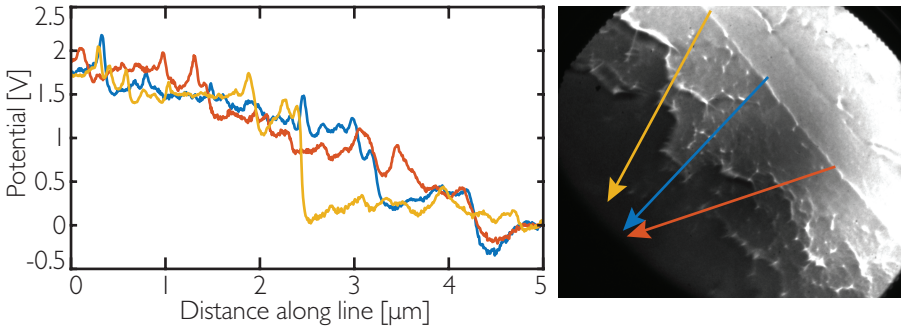

Fig. 7.11: Left: potential versus distance along the line segment shown on the LEEM image on the right (note: the lines are not of equal length, but the blue line is roughly 5 μm in length). The potential drop is much more homogeneous than in area 1. Only the yellow path shows a significant potential drop halfway along the path. Even though the potential drop is twice as large as in area 1, no significant distortions occur, suggesting a continuous network.

Fig. 7.12: LEEM-Potential map overlaid on a SEM image of area two, rotated 90 degrees counterclockwise with respect to the previous images of this area. The colormap represents the fitted voltage. The electrodes can be seen in white. The top right electrode is set at 2V, whereas the other electrode is grounded. It can be clearly seen that although there are a few irregularities, the voltage drops almost homogeneously from the top right to the bottom right electrode, indicating a good network quality.

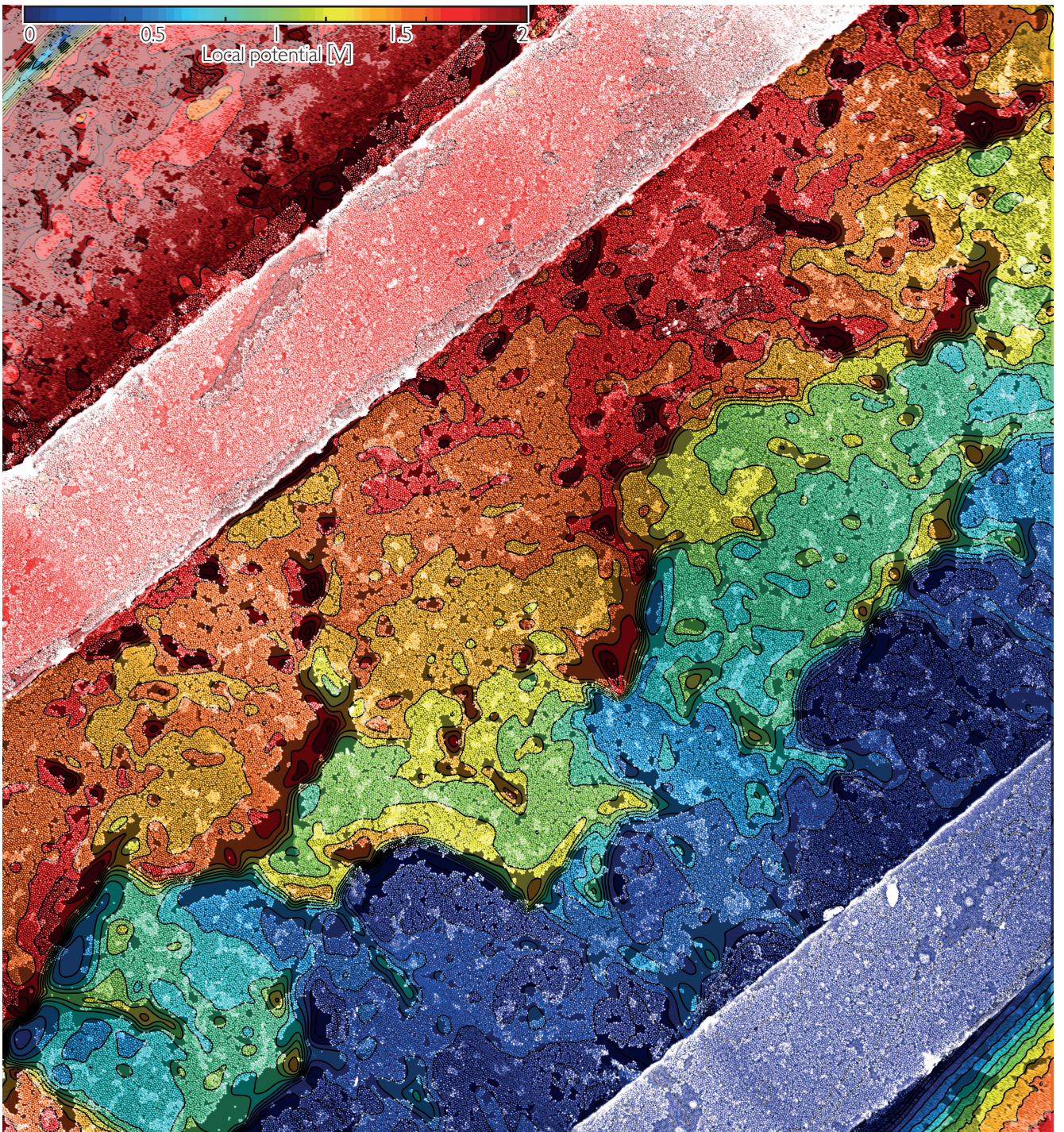

7.5 Conclusion

We study gold nanoparticle networks using potentiometry in LEEM. Although the networks are inherently 'dirty' and LEEM is surface-sensitive, we obtain sub-micron resolution which proves adequate for potentiometry. We analyzed the potential drop in two areas of a gold nanoparticle network: a well-connected area, and an area with significant cracks along the array. In both areas, we find that the contact resistance is negligible. Additionally, we find that in the well-connected area, the voltage drop is relatively unaffected by any small holes or grain boundaries present, indicating good electrical connectivity in the presence of small irregularities. However, the large cracks in the other area have a significant effect on the current path, as large current densities between the cracks cause large voltage drops in these areas. These large voltage drops might affect transport by lifting these areas out of the Coulomb blockade, an interesting area for further studies.

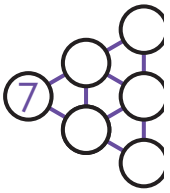

References

[1] R.M. Tromp, J.B. Hannon, A.W. Ellis, W. Wan, A. Berghaus, and O. Schaff. A new aberration-corrected, energy-filtered leem/peem instrument. i. principles and design. *Ultramicroscopy*, 110(7):852 – 861, 2010.

[2] S. M. Schramm, J. Kautz, A. Berghaus, O. Schaff, R. M. Tromp, and S. J. van der Molen. Low-energy electron microscopy and spectroscopy with escher: Status and prospects. *IBM Journal of Research and Development*, 55(4):1:1–1:7, 2011.

[3] S.M. Schramm, A.B. Pang, M.S. Altman, and R.M. Tromp. A contrast transfer function approach for image calculations in standard and aberration-corrected leem and peem. *Ultramicroscopy*, 115:88 – 108, 2012.

[4] M. P. Seah and W. A. Dench. Quantitative electron spectroscopy of surfaces: A standard data base for electron inelastic mean free paths in solids. *Surface and Interface Analysis*, 1(1):2–11, 1979.

[5] J. Kautz. *Low-Energy Electron Microscopy on Two-Dimensional Systems*. PhD thesis, Universiteit Leiden, 2015.

[6] J. Kautz, J. Jobst, C. Sorger, R. M. Tromp, H. B. Weber, and S. J. van der Molen. Low-Energy Electron Potentiometry: Contactless Imaging of Charge Transport on the Nanoscale. *Scientific Reports*, 5:13604, 2015.

[7] Wilhelm Melitz, Jian Shen, Andrew C. Kummel, and Sangyeob Lee. Kelvin probe force microscopy and its application. *Surface Science Reports*, 66(1):1 – 27, 2011.

[8] Johannes Jobst, Jaap Kautz, Maria Mytiliniou, Rudolf M. Tromp, and Sense Jan van der Molen. Low-energy electron potentiometry. *Ultramicroscopy*, pages 74 – 80, 2017.

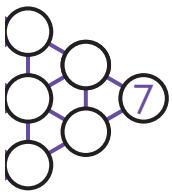

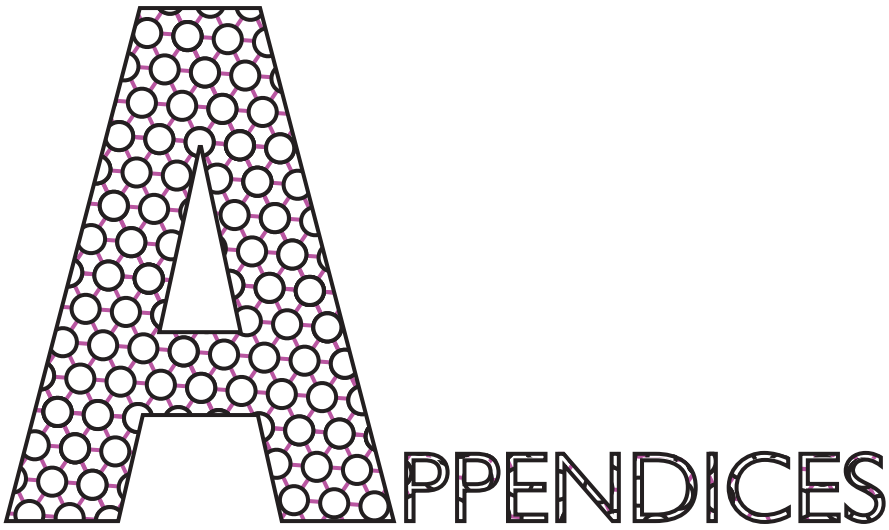
APPENDICES

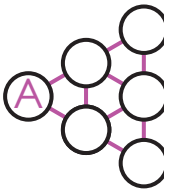

Appendix A

Theoretical background of approach 1

Starting from Eq. 3.3, we first take at a look at one of the two possible virtual states. The first virtual state is where an electron from the left lead tunnels through the left molecule onto the nanoparticle. This pathway is finalized by an electron from the nanoparticle that tunnels through the right molecule to the right lead. The matrix element for this state is as follows:

$$\frac{\langle i|\hat{H}|v_1\rangle\ \langle v_1|\hat{H}|f\rangle}{E_{v_1}-E_{\mathrm{i}}}=\frac{T_{\mathrm{M1}}T_{\mathrm{M2}}}{E_{\mathrm{L}}-E_{\mathrm{S1}}+E_{\mathrm{C}}+eV_{\mathrm{L}}}. \tag{A.1}$$

For the other virtual state, an electron first goes from the nanoparticle through the right molecule to the right lead and is then followed by an electron from the left lead that goes through the molecule onto the nanoparticle. The expression for this process is as follows:

$$\frac{\langle i|\hat{H}|v_2\rangle\ \langle v_2|\hat{H}|f\rangle}{E_{v_2}-E_{\mathrm{i}}}=\frac{T_{\mathrm{M2}}T_{\mathrm{M1}}}{E_{\mathrm{S2}}-E_{\mathrm{R}}+E_{\mathrm{C}}-eV_{\mathrm{R}}}. \tag{A.2}$$

The initial, virtual and final states are the unperturbed eigenstates of the molecule-nanoparticle-molecule system, defined analogously to the definition used by Averin et al.[Ch. 3, ref 3]. Substituting this back into Eq. A.1, we have to take the occupation of states into account to change the sum over states to a sum over energies. Also rewriting the delta function in terms of the energies in the system, we obtain:

$$\begin{aligned}\mathcal{R}=&\frac{2\pi}{\hbar}\sum_{E_{\mathrm{L}},E_{\mathrm{R}},E_{\mathrm{S1}},E_{\mathrm{S2}}}|T_{\mathrm{M1}}|^2\,|T_{\mathrm{M2}}|^2\\&\times\left|\frac{1}{E_{\mathrm{L}}-E_{\mathrm{S1}}+E_{\mathrm{C}}+eV_{\mathrm{L}}}+\frac{1}{E_{\mathrm{S2}}-E_{\mathrm{R}}+E_{\mathrm{C}}-eV_{\mathrm{R}}}\right|^2\\&\times f(E_{\mathrm{L}})\big[1-f(E_{\mathrm{R}})\big]f(E_{\mathrm{S2}})\big[1-f(E_{\mathrm{S1}})\big]\\&\times\delta(E_{\mathrm{R}}+E_{\mathrm{S1}}-E_{\mathrm{L}}-E_{\mathrm{S2}}-eV).\end{aligned} \tag{A.3}$$

We change the sum for an integral and pragmatically assume:

$$|T_{\mathrm{M1}}|^2\,|T_{\mathrm{M2}}|^2=T_{\mathrm{M1}}(E_{\mathrm{L}})T_{\mathrm{M2}}(E_{\mathrm{S2}}) \tag{A.4}$$

to obtain Eq. 3.4. This is done analogously to previous work[Ch. 3, ref 3], where these matrix elements are replaced by constants. To solve this integral numerically, we use the delta function to relate E_{R} to the other energies ($E_{\mathrm{R}}=E_{\mathrm{L}}-E_{\mathrm{S1}}+E_{\mathrm{S2}}+eV$) and replace

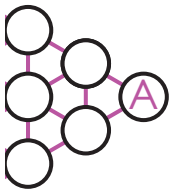

the four-dimensional integral by a three-dimensional one. We also calculated the current by relating E_{L} to the other energies ($E_{\mathrm{L}} = E_{\mathrm{R}} + E_{\mathrm{S1}} - E_{\mathrm{S2}} - eV$) and found no difference between results.

Appendix B

Equivalence of multiple cotunneling model to second-order cotunneling

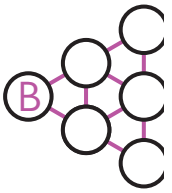

We start with the Fermi golden rule, just as with normal cotunneling:

$$\mathcal{R}_{\mathrm{i}\to\mathrm{f}} = \frac{2\pi}{\hbar}|M|^2\delta(E_\mathrm{f} - E_\mathrm{i}), \tag{B.1}$$

where E_i and E_f are the initial energy and final energy of the system respectively and M the matrix element for a fourth order cotunneling event. For the model considered by Averin *et al.*[Ch. 3, ref 3], this matrix element can be written as:

$$M = \sum_v \frac{\langle i|\hat{\hat{H}}|v\rangle\ \langle v|\hat{\hat{H}}|f\rangle}{E_v - E_\mathrm{i}}, \tag{B.2}$$

whereas for the fourth order cotunneling event, M can be written as:

$$M = \sum_{\{j_1,j_2,j_3,j_4\}} \prod_{k=1}^{3} \frac{\langle v_{k+1}|\,\hat{H}\,|v_k\rangle}{E_{v_k} - E_\mathrm{i}}\,\langle v_1|\,\hat{H}\,|i\rangle\,. \tag{B.3}$$

The summation is now over 4! virtual states, and the product is over the whole sequence of cotunneling events. In other words, this product can be written as:

$$\prod_{k=1}^{3} \frac{\langle v_{k+1}|\,\hat{H}\,|v_k\rangle}{E_{v_k} - E_\mathrm{i}}\,\langle v_1|\,\hat{H}\,|i\rangle = \frac{\langle i|\,\hat{H}\,|v_1\rangle\,\langle v_1|\,\hat{H}\,|v_2\rangle\,\langle v_2|\,\hat{H}\,|v_3\rangle\,\langle v_3|\,\hat{H}\,|f\rangle}{\Delta E_1 \Delta E_2 \Delta E_3}, \tag{B.4}$$

where the energy differences of the Heisenberg uncertainty relation are taken into account by the ΔE_i in the denominator. Following the derivation by Averin *et al.*[Ch. 3, ref 16], we can replace the matrix elements by transmission constants. The previous equation then becomes:

$$\prod_{k=1}^{3} \frac{\langle v_{k+1}|\,\hat{H}\,|v_k\rangle}{E_{v_k} - E_\mathrm{i}}\,\langle v_1|\,\hat{H}\,|i\rangle = \frac{T_1 T_2 T_3 T_4}{\Delta E_{v1} \Delta E_{v2} \Delta E_{v3}}. \tag{B.5}$$

Since the result of multiplication does not depend on the order of multiplication, we can simply write the transmission coefficients as follows:

$$T_1 T_2 T_3 T_4 = T_{\mathrm{L,M1}} T_{\mathrm{M1,NP}} T_{\mathrm{NP,M2}} T_{\mathrm{M2,R}}. \tag{B.6}$$

where the transmission coefficients here are respectively from the left lead to the first molecule, from the first molecule to the charging island, from the charging island to the second molecule and from the second molecule to the right lead.

If we assume that the energy differences ΔE_i are dominated by the charging energies of the nanoparticle and molecules, all other energies can be ignored. This means that the sum over all virtual pathways becomes a constant which only depends on the charging energies of the molecules and nanoparticle.

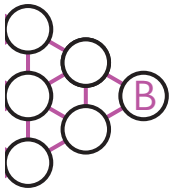

$$\sum_v \frac{T_1 T_2 T_3 T_4}{\Delta E_1 \Delta E_2 \Delta E_3} = \frac{T_{\mathrm{L,M1}} T_{\mathrm{M1,NP}} T_{\mathrm{NP,M2}} T_{\mathrm{M2,R}}}{E_{\mathrm{S}}(E_{\mathrm{C,M1}}, E_{\mathrm{C}}, E_{\mathrm{C,M2}})}, \tag{B.7}$$

$$E_{\mathrm{S}}(E_{\mathrm{C,M1}}, E_{\mathrm{C}}, E_{\mathrm{C,M2}}) \equiv \left(\sum_v \frac{1}{\Delta E_{v1} \Delta E_{v2} \Delta E_{v3}} \right)^{-1}.$$

If we now define $T_1^\dagger \equiv T_{\mathrm{L,M1}} T_{\mathrm{M1,NP}}$ and $T_2^\dagger \equiv T_{\mathrm{NP,M2}} T_{\mathrm{M2,R}}$, we have:

$$M = \frac{T_1^\dagger T_2^\dagger}{E_{\mathrm{S}}}, \tag{B.8}$$

which is similar to the matrix element in cotunneling derived by Averin *et al.*[Ch. 3, ref 16]. This therefore means that our fourth order cotunneling event will resemble the already familiar cotunneling, with a transmission function that decreases with increasing Coulomb charging energy. This in turn means that even if there are single levels in between the charging island and the leads, the transmission probability of these levels will be constants.

Appendix C

Pulse tube operation

The Oxford Instruments Teslatron is a closed loop cryostat, which means that it uses a compression/decompression cycle in a pulse tube to cool down the sample. A typical pulse tube is shown in Fig. C.1. In the beginning of the compression cycle, the piston moves downwards, increasing the pressure of the gas and forcing it to flow through the regenerator, heating it. The flow continues through the cold end of the pulse tube (T_C) to the hot end (T_H). The hot end is kept at room temperature, and the compressed gas is cooled down at the end of the compression cycle (Fig. C.1 center image). During the decompression cycle (Fig. C.1 right image), the gas in the pulse tube expands, causing it to cool down. The cool gas cools down the heat exchanger at the cold end and enters the regenerator. Here, the regenerator exchanges heat with the cold gas, causing it to cool down to a lower temperature than in the previous cycle. Since the regenerator pre cools the gas before compression the cold end of the pulse tube iteratively achieves a lower temperature. In most systems, the gas on the hot end of the pulse tube does not reach the cold end, which thermally insulates both ends.

The Teslatron uses a two-stage pulse tube cooler to achieve its base cold stage temperature of 3 K. This means that a second pulse tube and regenerator are added to the loop. The first pulse tube and regenerator cool a stage down to between 70 and 40 K, which is used to pre-cool the second stage. Although Fig. C.1 shows a piston to act as a compressor, no piston is used in the cryostat. Instead, an external 7.5 kW compressor compresses and pre-cools the helium back to room temperature. The high pressure (20 bars) helium is fed

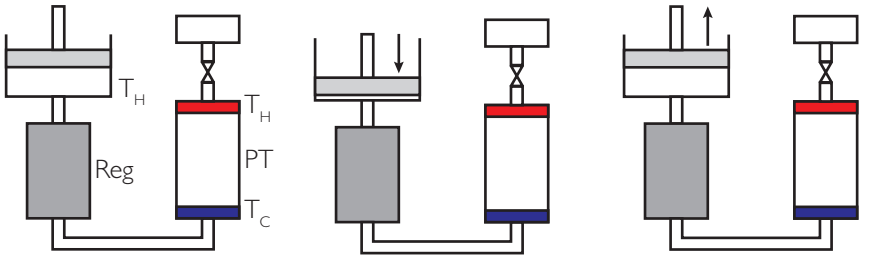

Fig. C.1: Schematic of a pulse tube cooler during various stages of the cooling cycle. Left is before the compression cycle, center is after the compression cycle, right is after the decompression cycle, seen as a difference in position of the piston. Each cycle iteratively cools down the regenerator (Reg), by repeatedly compressing and expanding the gas in the pulse tube (PT).

into the cryostat using a rotary valve to control the flow. This valve periodically switches between the high and low pressure lines of the compressor

In order to cool down to even lower temperatures, the 3 K stage is used to cool down a helium gas flow. The helium exchanges heat with the stage, causing it to cool down. By pumping on the other side of the helium, the helium expands and cools down even further. It then flows past the insert chamber, cooling down the chamber and the insert inside of it. By varying the flow of the helium using a needle valve, the cooling power can be regulated. A lower flow gives a lower pressure, causing the helium to cool down more. However, since the helium pressure is low, the amount of helium flowing past the insert chamber is also low, causing a low cooling power. Increasing the helium flow increases the cooling power, but raises the helium temperature. Therefore, in order to cool down quickly, the insert is first cooled down to 50 K at high helium flow, after which the flow is reduced in order to reach base temperature.

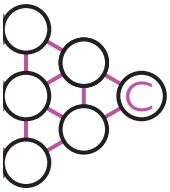

It is worthwhile to note that the bottom of the insert is physically separated from the insert chamber. In order to allow heat to flow from the insert to the chamber walls, the insert chamber is filled with room pressure helium exchange gas before cooling down. In order to increase heat exchange at low temperatures, extra helium is added at low temperature*.

*Due to the ideal gas law, a volume of room pressure gas at low temperatures will build up a high pressure when heated up. It is therefore important that a properly working overpressure valve is fitted to the insert chamber.

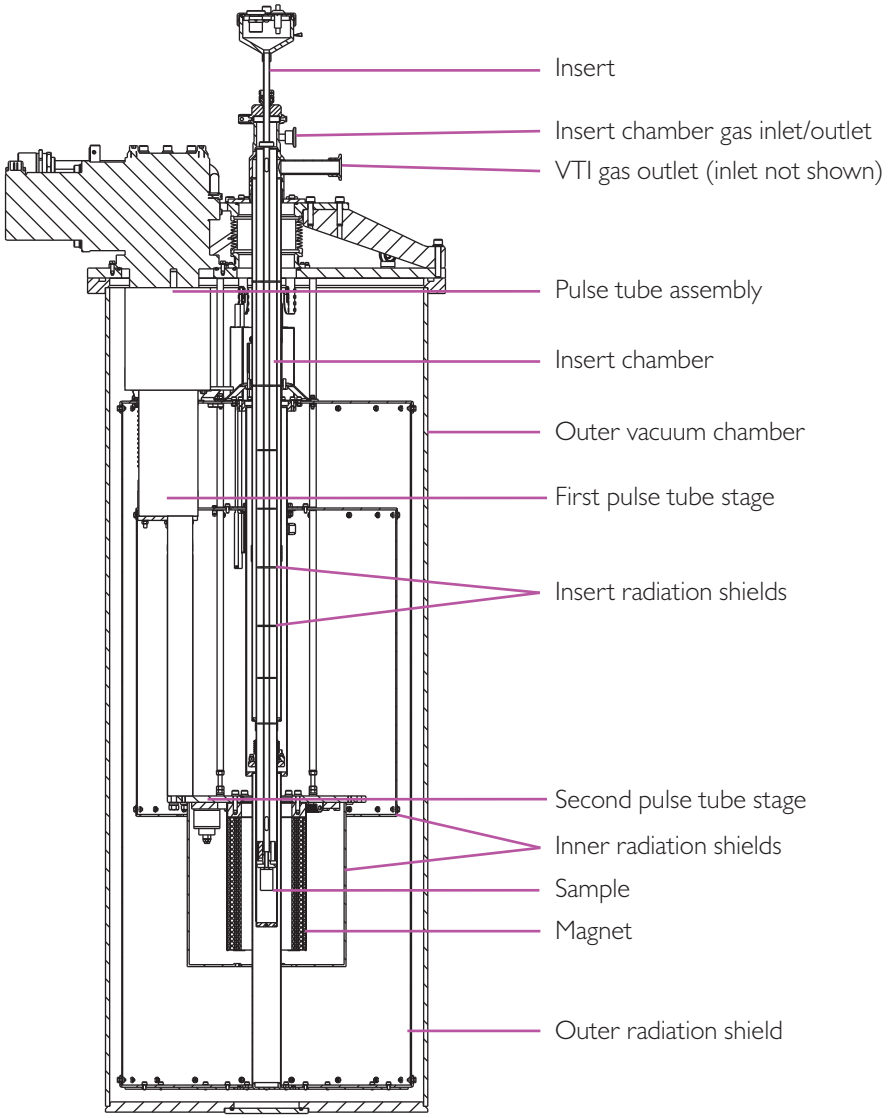

Fig. C.2: Schematic of the Teslatron cryostat as delivered by Oxford Instruments. The bulk of the machine is made up by the outer vacuum chamber providing thermal solation from the environment. The placement of the two stage pulse tube and the attachment to the radiation shields can be clearly seen in this figure.

Appendix D

Exploring the parameter space of the alternative model

In order to determine whether the correlation between the slope and the average cotunneling length, we explore more of the parameter space by varying E_C and $G_\mathcal{T}$. We repeat the calculation for 30 values of the transmission probability $G_\mathcal{T}/G_0$ and 30 values of E_C, each for 25 temperatures (22 500 IV-curve calculations for 11 250 000 total data points). Since 22 500 IV-curves are too many to analyze individually, we determine j_{mean} and the slope at each data point and correlate them in a histogram. The results can be seen in Fig. D.1, which shows the logarithm of the number of occurrences of each combination of j_{mean} and slope. The logarithm is taken, since a large part of the IV-curves are sequential tunneling (CI and CIII regimes) and push the rest of the histogram off of the scale.

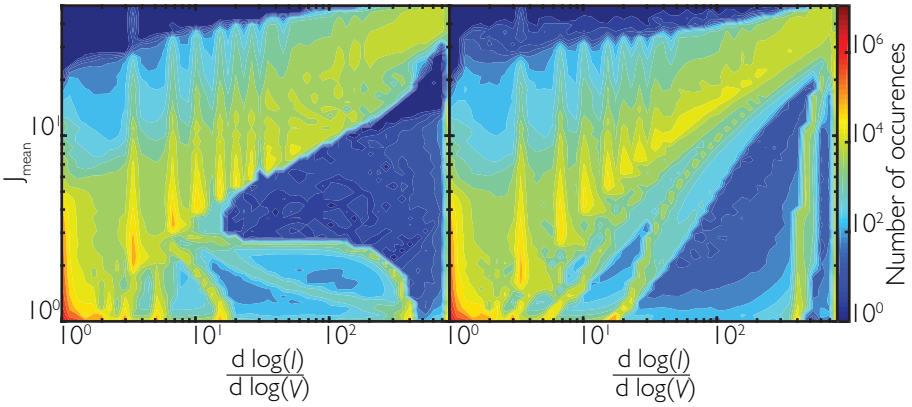

Fig. D.1: Histogram showing the number of occurrences for each combination of j_{mean} and slope, colormap is on a logarithmic scale. Left is the model using the alternative model in Eq. 5.13, right replaces the probability term $\mathcal{P}$ from Eq. 5.12 by the term in Eq. 5.10, effectively removing the dependence on cotunneling length of E_C. Removing this dependence slightly decreases the cotunneling length for all systems, seen as the general downward shift of the green graph. Otherwise, the graphs look similar. It can be seen that as the slope increases, so does the cotunneling length. However, certain values of slope (e.g. 3.5, 7, 10) correspond to many values of average cotunneling length. We think this might have something to do with the sharp steps in j_{mean} corresponding to peaks in the slope, as seen in Fig. 5.4, but the exact origin of this is unclear.

The graphs show that although no one-to-one correspondence is present, there is a correlation between the slope and j_{mean} in both diagrams. Interestingly, there are certain values of slope which occur more often than others and correspond to a range of j_{mean}. Although the origin of these features is unclear, they might have to do with the stepwise increase in j_{mean} correlating with peaks in the slope, seen in Fig. 5.4.

Since the prediction of the Arrhenius model that j_{mean} depends on the slope is only an approximation valid in a certain regime, it makes sense to compare the results in Fig. D.1 to the same calculation using the Arrhenius model. These can be seen in Fig. D.2.

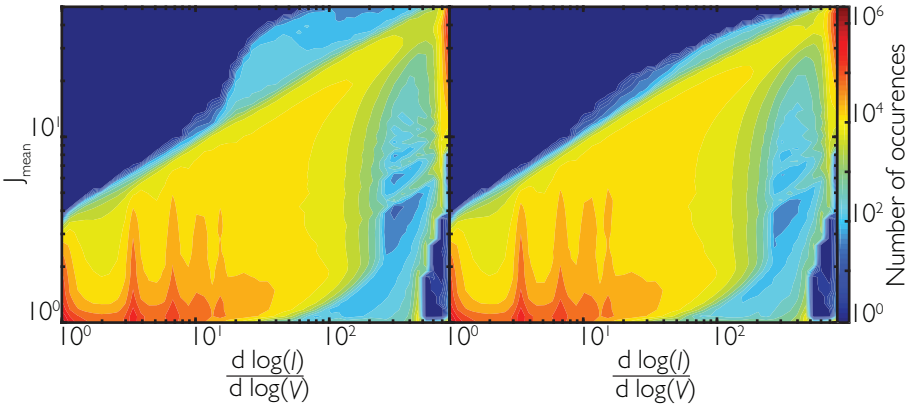

Fig. D.2: Histogram showing the number of occurrences for each combination of j_{mean} and slope, calculated with the Arrhenius model. Left is the model using Eq. 5.1, but replaced the probability term by Eq. 5.12, left is calculated using Eq. 5.1. The left therefore has a reduction in E_{C}, and the right one has not, identical to Fig. D.1. Using the reduction in E_{C} slightly increases the cotunneling length in cases of high slope. The graphs are smoother than those in Fig. D.1, indicating less preference for certain values of slope. Otherwise, there is a wide distribution in j_{mean} and slope, similar to the previous graph.

Although the general structure is similar to Fig. D.1, there are some striking differences. The first is that the predicted cotunneling length according to the Arrhenius model is lower than according to the new model. Furthermore, the graphs are more smoothed out than Fig. D.1, which have more detailed features. This means that there are no preferred values for slope, such as in the previous model, nor are there preferred cotunneling lengths. Otherwise, the graphs have the same structure, indicating that the overall correlation between j_{mean} and the slope is similar in both models across all regimes. It should be noted that these figures show data across all regimes, not only the C2 regime.

We further investigated both models in the C2 and CII regimes, so see if the link between slope and j_{mean} is more clear here. The results are shown in Fig. D.3.

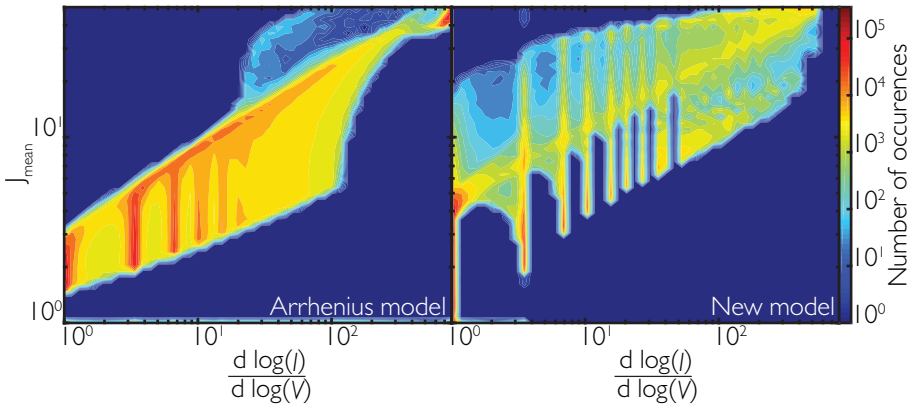

Fig. D.3: Histogram showing the number of occurrences for each combination of j_{mean} and slope, calculated with the Arrhenius model (left) and the new model (right). The Arrhenius model shows a much stronger correlation between j_{mean} and slope in the C2 regime, although there are still a lot of possible values for j_{mean} for each value of slope. The New model shows an even more peculiar pattern. Certain values of slope are preferred, which correspond to many different average cotunneling lengths.

Comparing these figures to the previous calculations, we see that there is less freedom in j_{mean} for each value of slope. However, there are still many possible values for j_{mean} at each slope, especially for the new model. Moreover, the new model shows that certain slopes have a very high occurrence rate, with those in between almost not happening at all. These features can also be seen in Fig. D.1. We think that these have the same origin, and the values in between the preferred slopes fall outside the CII regime.

From these data, we conclude that in both models, but especially in the new model, the correlation between j_{mean} and slope is non-trivial. Specifically, it is not generally possible to determine j_{mean} from α.

Appendix E

Additional data for chapter 6

E.1 Additional fitting on 10 nm nanoparticle networks

In addition to the data shown in Fig. 5.8, we show that a different device on the same sample can be fitted using the new model. We fit the model to the data before and after exchange, as can be seen in Fig. E.1. The model follows the pre-exchange data nicely, although it predicts a current that is too low at around 0.1 V. This underestimation is less present in the post-exchange data. Moreover, the model gives an accurate fit to the post-exchange data, only needing a significant change in $G_{\mathcal{T}}$ (around four orders of magnitude) and E_{C} and $E_{\mathrm{C,var}}$ (a factor of two). The rest of the fitted parameters are almost identical.

	E_{C}	$E_{\mathrm{C,var}}$	$G_{\mathcal{T}}$	AR	N
Pre exchange	28.9 meV	5.75 meV	$3.50{\cdot}10^{-10}$ G_0	302	36
Post exchange	15.4 meV	2.87 meV	$5.94{\cdot}10^{-6}$ G_0	277	36

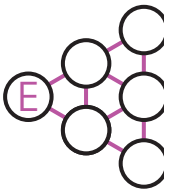

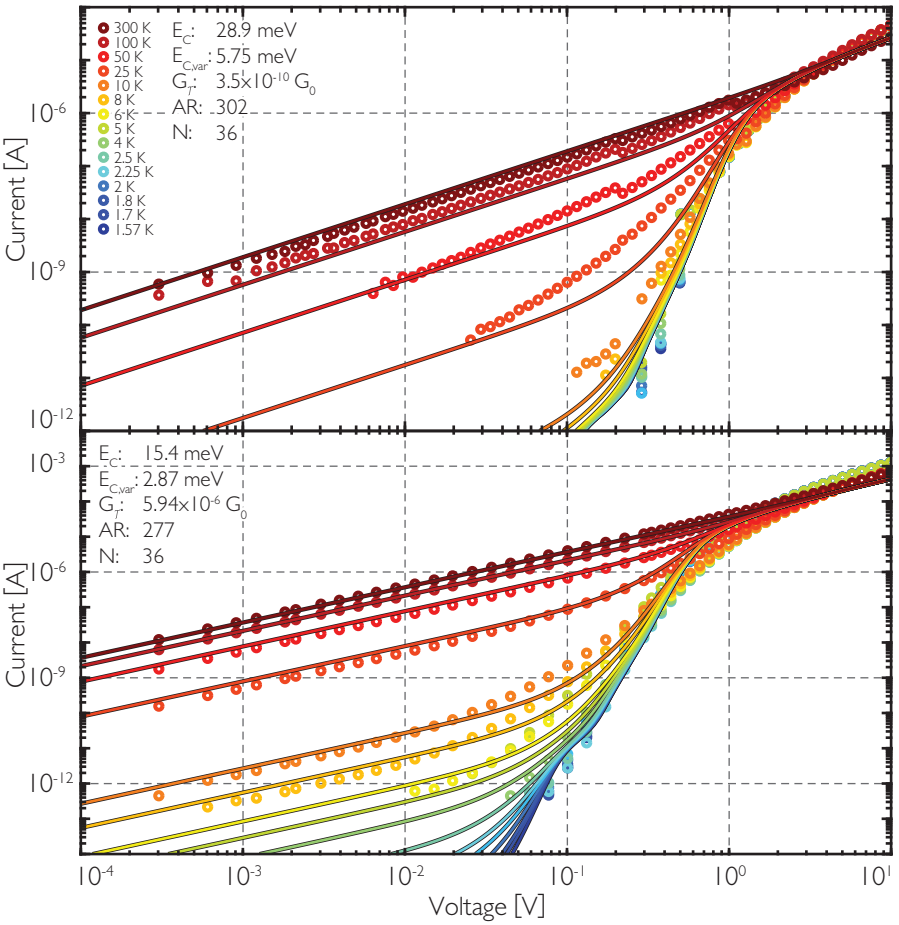

Fig. E.1: Pre-exchange (top) and post-exchange (bottom) current versus voltage plots with the corresponding fitted curves using the new model. The data is of a different device on the same sample as the data from Fig. 5.8. The fits show the same trend as in chapter 5, with the pre-exchange fit being slightly too low around 0.1 V, a feature which is less present post exchange. The parameters before and after exchange are similar to those in chapter 5, with the exception of the post-exchange $G_{\mathcal{T}}$ being an order of magnitude lower in this device. Additionally, the post-exchange E_C is 25% smaller in this device, which is half the pre-exchange value.

E.2 Full data set on slope versus voltage

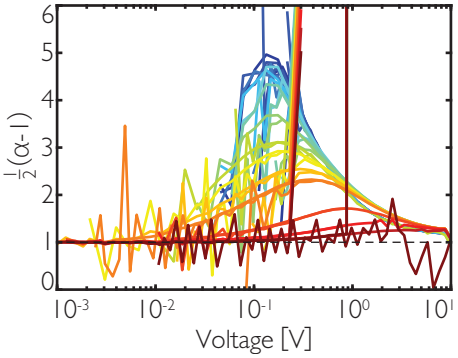

Fig. E.2: The original data from Fig. 5.10, including the data removed in this figure. For a complete description, see Fig. 5.10 in chapter 5.

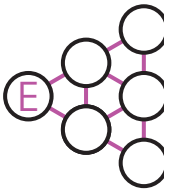

Appendix F

Fits to the data after exchange with molecular switches

The figure below shows the fits to the data obtained in chapter 6.

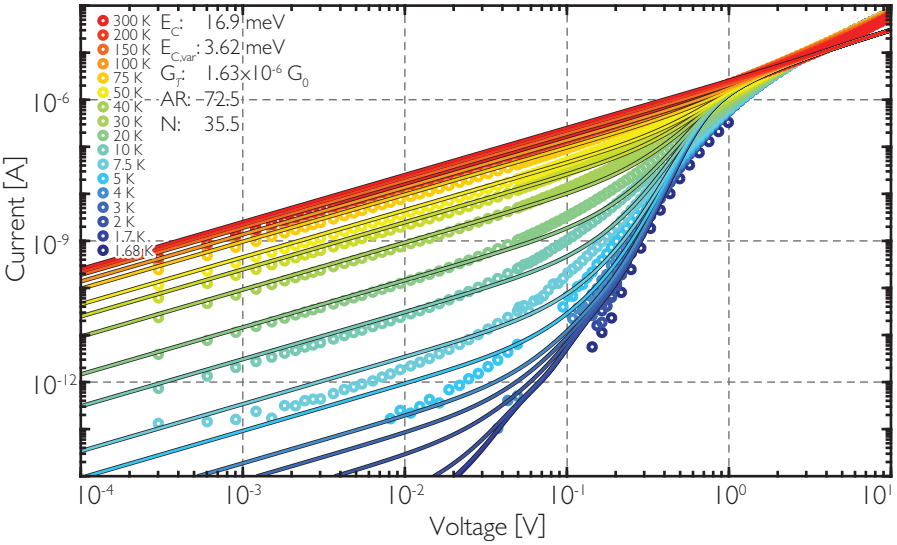

Fig. F.1: Fits to the data in Fig. 6.8 using the new model. The parameters are similar to those found in chapter 5, although E_C is around twenty percent lower.

Summary

The ultimate miniaturization of modern electronics was first discussed by Richard Feynman in 1959. During his lecture titled 'There's plenty of room at the bottom', the future Nobel laureate coined the idea of manipulating single atoms to create the smallest possible electronic components. Now, almost sixty years later, scientists in the field of molecular electronics work on its realization. Although the dream originally was to replace silicon-based technology by one based on single molecules, most scientists now agree that this is beyond our current reach. Single molecules prove to be too unstable to generate fast and consistent signals, something that is crucial for them to be used in our computers.

The greatest challenge that long hindered the development of molecular electronics, is the contacting of the individual molecules. Molecules are very small, typically a few nanometers*, or billionths of a meter. To study the electronic properties of single molecules, you have to connect your macroscopic measurement equipment to the micro- (or nano-) scopic molecule. This is not a trivial problem, and it took around 20 years to solve this problem (outlined in the introduction of chapter 1). Nowadays, a wide variety of methods to connect single, or clusters of molecules exists. One of these is a network of nanoparticles; an ordered structure of small spheres, in my case made of gold. By using the molecules as bridges between the nanoparticles, it is possible to study the molecules by investigating the entire network. Since a network is a hundred to a thousand times larger than the molecules in between the particles, this is much simpler. Moreover, a network like this has a much higher stability than a single molecule, as a network contains countless individual molecules. This is also its largest limitation; a network can not be used to study a single isolated molecule. Nevertheless, networks are an ideal platform to test the functionality of molecules. Functional molecules react to changes in their environment, a reaction which is usually measurable. Among these are light-sensitive switches which can be turned on or off using light, where the off-state has a higher electrical resistance. Other molecules react similarly when encountering a certain chemical compound. In these cases, networks of nanoparticles interlinked by molecules can act as sensors or switches. Moreover, these networks are also intrinsically interesting.

To explain why, let's first consider a single nanoparticle in between two electrodes, rather than an entire network. Electrical current consists of electrons that travel from A to B, which

*A nanometer is an important unit. Us humans usually think in meters (or feet if you want to use a less sensible unit of distance), as most things surrounding us are around a few meters or tenths of meters away from us. Single molecules are usually a few nanometers long, with the distance between the atoms typically being a few tenths of nanometers.

is why I talk about electron transport rather than electrical current[†]. An electrical current through the nanoparticle is facilitated by electrons hopping onto the nanoparticle from one side, and hopping off from the other side. This requires that the electron itself is located on the nanoparticle for a short time. This charges the particle, requiring a bit of energy. Under normal circumstances, like at room temperature and voltages of a few volts, this is not a problem. However, when we cool down the system to a few Kelvin[‡], and we only apply a few millivolts, the behavior changes drastically. Electrons lack the energy to charge the nanoparticle, and the current decreases sharply.

This is called Coulomb blockade, after Charles-Augustin de Coulomb, who described how two charges influence each-other. According to classical mechanics, the behavior inside the Coulomb blockade regime is clear, as conservation of energy forbids any electrons from flowing through the nanoparticle. However, electrons are so small that their behavior is governed by quantum mechanics. Quantum mechanics is not as unforgiving as classical mechanics, and is fine with electrons violating conservation of energy, given that they do not do so for too long. This behavior is described by the Heisenberg uncertainty principle of time and energy, which in this case describes that the shorter the electrons occupy the nanoparticle, the more they can break the law of conservation of energy. Loosely formulated, an electron that wants to travel from left to right through the nanoparticle is allowed to hop onto the nanoparticle, sit there for a while, before it realizes that it's breaking the law and hops back off. Similarly, an electron already residing on the nanoparticle is allowed to hop off, briefly, leaving the nanoparticle charged positively, before realizing this also violates conservation of energy and reluctantly returns to the nanoparticle. However, if these two electrons coincidentally decide to travel at the same time, one from the left onto the nanoparticle, the other to the right off of the nanoparticle, the particle remains uncharged, while we effectively took one electron from the right to the left. Electrical current!

This method of quantum transport is called cotunneling and is explained in more detail in chapters 2 and 3. What is important about this form of transport, is that both electrons need to contribute, otherwise the entire process is canceled. If the chance that one electron will contribute (also called the transmission probability or $\mathcal{T}$) is equal to trowing six with a die (one sixth), then the chance of both electrons contributing is equal to throwing six twice, or one thirty-sixth. In the case of longer chains of nanoparticles, electron transport is facilitated by multiple cotunneling, in which many electrons simultaneously participate in the process of generating an electrical current. Analogously to the previous example, you have to throw a die for every electron individually, and only if you throw six each time, a current arises. The current I therefore scales with the transmission probability $\mathcal{T}$ to a certain power N: $I \propto \mathcal{T}^N$.

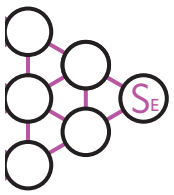

[†] In principle, these two are identical. However, there is one small difference: electrons are negatively charged. This means that an electrical current from left to right is caused by electrons traveling in the opposite direction, from right to left

[‡] One Kelvin is one degree above absolute zero, around 273 degrees Celsius below zero.

This has far-reaching consequences. The chance that one single electron hops from one to the next nanoparticle is strongly influenced by the molecule in between the particles. Moreover, if that molecule is a functional molecule, like a switch, this chance can be changed by shining light on the network. If in this case, this changes the probability from one sixth to one half, the current changes not by a factor of three, but by 3^N. For a chain of four nanoparticles ($N = 5$), this difference is a factor of 243, a large difference! You could say that cotunneling increases the sensitivity of the network to the molecules in between the nanoparticles. We try to test this prediction in chapter 6, but learn in chapter 5 that the current theory of multiple cotunneling is not sufficient to describe the current through our networks.

The current theory that describes cotunneling assumes that the probability of an electron hopping from one nanoparticle to the next is independent of the energy of the electron. Normally, this is a good assumption, however, depending on the interlinking molecule, it might not always be correct. If the highest occupied molecular orbital (HOMO) or lowest unoccupied molecular orbital (LUMO) is close to the Fermi energy of the contacts and the nanoparticle (compared to the energy required to charge the nanoparticle), the energy dependence of the transmission probability becomes significant. In chapter 3, we calculate the effect on the current through a single nanoparticle. We approach this problem in two different ways, first for the case that transport through the molecule is resonant. This means that the electron 'flows' through the molecule, during which one orbital or molecular level carries the entire current. In this case, we predict that at high voltages, the current increases as the resonance energy of the molecular level is further away from the Fermi energy of the contacts. This is opposite to the expected result when cotunneling does not play a role. The second approach assumes non-resonant transport through the molecule, which means that the electron hops on to, and off of the molecule rather than 'flowing' through it. In this case, electron transport through the entire molecule-nanoparticle-molecule system is facilitated by multiple cotunneling. If the charging energy of the molecules is larger than that of the nanoparticle, we predict a strong simplification of the behavior of the current. The transmission probability seems independent of the electron energy, and the behavior reduces to the current cotunneling theory by Averin and Nazarov[Ch. 3, ref 16]. This implies that a system with molecules is indistinguishable from one without.

To describe electron transport through entire networks, we not only need to account for cotunneling, but also for multiple cotunneling. The commonly used theory describing multiple cotunneling, however, is but an *ad hoc* expansion of normal cotunneling. It is an approximation that doesn't necessarily always agree with reality. In chapter 5, I describe a new model derived from basic principles which makes more accurate predictions. Moreover, this model is also applicable at high voltages (when the electrostatic energy eV is larger than the charging energy E_C). I fit this model to measured data, but only succeed when I account for disorder in the network. By assuming that the charging energy of every nanoparticle varies slightly from one particle to the next, I am able to model the experimental data. More

importantly, my fits imply no noticeable contribution of (multiple) cotunneling to the current through the network. Electron transport almost completely consists of highly energetic electrons that do not need cotunneling to cross the array. At low voltages and temperatures, a small number of percolating current paths carries all the current through the network. As the voltage increases, more paths contribute to the current, and at large voltages, all possible paths contribute. This is an important conclusion that is in sharp contrast with the current consensus.

This conclusion also has an impact on the prediction from a few paragraphs ago, where we said that networks of nanoparticles have an enhanced sensitivity for the molecules interconnecting them. As cotunneling does not contribute to the current significantly, it remains a question whether this prediction still holds. In chapter 6, I use my new theory to calculate the enhancement in sensitivity. Changing the molecules does not only change the transmission probability, it also changes the permittivity and therefore the charging energy. I predict that a small change in charging energy has a large effect on the current through the network, which means that the network can still enhance the properties of the molecule. To experimentally verify this prediction, we use a molecular switch as a bridge between the particles in the network and try to switch this while measuring the current through the network. Although the molecule does switch in solution, it does not appear to switch after being inserted into the network. Unfortunately, we therefore cannot make any decisive conclusion as to whether we can use nanoparticle networks to enhance the properties of the bridging molecules.

In the last chapter 7, we take a different perspective to look at the flow of electrons through nanoparticle networks. We use a low-energy electron microscope or LEEM to measure the voltage drop across a network with sub-micrometer accuracy. In the LEEM, we fire electrons at the network and slow them down to a near stop before arriving at the network. By applying a voltage across the network, the incoming electrons are locally attracted or repelled, dependent on the local potential. If the electron is repelled, it will end up at the detector and produces a signal. However, if it is attracted, it will reach the network, likely being scattered and not giving a signal at the detector. By tuning the velocity of the incoming electrons and determining at what exact energies they are absorbed, we can deduce the local potential. This does not only give the beautiful pictures in chapter 7, it also provides a lot of information on the electronic structure in the network. We see, for example, that electron are blocked by large gaps in the network, but remain largely unaffected by smaller holes and imperfections. Moreover, we see that they have no problem travelling from the electrodes into the network.

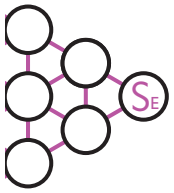

This thesis describes fundamental research on electron transport through networks of nanoparticles. The most important result is that this kind of transport can be described by only first-order contributions, *i.e.* without cotunneling. Disorder is the dominant factor. Despite the absence of higher-order transport, my model predicts that an enhanced sensitivity of the networks to the inserted molecules should still be present.

Samenvatting

De ultieme miniaturisatie van hedendaagse elektronica werd voor het eerst besproken door Richard Feynman in 1959. Tijdens zijn voordracht met de titel 'There's plenty of room at the bottom' besprak de latere Nobelprijswinnaar de mogelijkheid om enkele atomen te manipuleren om zo de kleinst mogelijke elektronische componenten te maken. Nu, bijna zestig jaar later werken wetenschappers in het veld van moleculaire elektronica hard aan de realisatie ervan. Hoewel het ooit de droom was om alle op silicium gebaseerde technologie te vervangen door één gebaseerd op moleculen, zijn de meeste wetenschappers in het veld nu van mening dat dit te hoog gegrepen is. Enkele moleculen blijken te instabiel om snel en consistent betrouwbare signalen te geven; iets wat absoluut vereist is voor het gebruik in onze computers.

De grootste uitdaging die de ontwikkeling van moleculaire elektronica lang heeft belemmerd, is het contacteren van het molecuul zelf. Moleculen zijn erg klein, typisch een paar nanometer[§], of een paar miljardste meter. Om de elektronische eigenschappen van het molecuul te bepalen, moet je je grote macroscopische meetapparatuur op het molecuul aansluiten. Dit is geen triviaal probleem, en het heeft ook rond de 20 jaar geduurd om dit op te lossen. Tegenwoordig zijn er verscheidene methoden om enkele moleculen, of clusters van moleculen te kunnen meten (deze worden kort besproken in hoofdstuk 1). Eén hiervan is een netwerk van nanodeeltjes; een geordende structuur van kleine bolletjes, in mijn geval van goud. Door de moleculen als bruggetjes tussen de nanodeeltjes te zetten, is het mogelijk om wat te leren over de moleculen door de eigenschappen van het hele netwerk te meten. Aangezien een netwerk tussen de honderd tot duizend keer groter is dan de moleculen in het netwerk, is dit veel eenvoudiger. Verder is zo'n netwerk ook veel stabieler dan een enkel molecuul, aangezien het netwerk bestaat uit talloze individuele moleculen. Dit is ook direct de beperking; een netwerk kan namelijk niet gebruikt worden om echt één enkel molecuul te meten. Desondanks zijn netwerken een uitstekend platform om functionaliteit van moleculen te testen. Functionele moleculen reageren op verandering in hun omgeving, wat veelal meetbaar is. Zo zijn er lichtgevoelige moleculaire schakelaars die aan of uit te schakelen zijn met licht, waarbij het in de uit-stand veel moeilijker is (dat wil zeggen dat de elektrische weerstand weerstand in de uit-stand veel hoger is) om er een elektrische stroom doorheen te sturen. Andere moleculen reageren soortgelijk als ze in contact komen met een specifieke chemische stof. In dit geval kunnen netwerken van nanodeeltjes verbonden door moleculen fungeren als sensoren of schakelaars. Echter zijn deze netwerken ook interessant *an sich*.

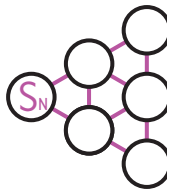

[§]De nanometer is een belangrijke eenheid. Wij mensen denken vaak in meters, aangezien de meeste dingen om ons heen typisch een paar meter of tiende meter verwijderd zijn. Enkele moleculen zijn ongeveer een nanometer groot, met de afstand tussen atomen typisch een paar tiende nanometer.

Om dit uit te leggen, laten we eerst niet kijken naar een compleet netwerk van nanodeeltjes, maar naar één enkel nanodeeltje tussen twee elektroden. Elektrische stroom bestaat uit elektronen die van A naar B reizen, vandaar dat we het ook wel hebben over elektrontransport in plaats van stroom[¶]. Elektrische stroom door het nanodeeltje wordt gefaciliteerd door elektronen die van de ene kant op het nanodeeltje 'hoppen', en er aan de andere kant weer af 'hoppen'. Dit vereist natuurlijk dat het elektron voor een korte tijd op het nanodeeltje zelf zit. Dit laadt het nanodeeltje op, wat een klein beetje energie kost. Onder normale omstandigheden, zoals bij kamertemperatuur en spanningen van enkele volts is dit geen probleem. Maar wanneer het hele systeem wordt afgekoeld tot enkele kelvins[♮] en er maar een paar duizendste volt over het nanodeeltje wordt gezet, verandert het gedrag drastisch. Elektronen hebben niet genoeg energie meer om op het nanodeeltje te gaan zitten, en de stroom door het deeltje neemt sterk af.

Dit wordt ook wel Coulomb-blokkade genoemd, naar Charles-Augustin de Coulomb, die ontdekte hoe twee ladingen invloed op elkaar uitoefenen. Volgens de klassieke mechanica is het gedrag tijdens Coulomb-blokkade duidelijk, aangezien de wet van behoud van energie verbiedt dat er elektronen door het nanodeeltje kunnen gaan. Elektronen zijn echter zo klein, dat hun gedrag wordt beschreven door de kwantummechanica. De kwantummechanica is minder streng, en vindt het prima dat de elektronen de behoudswet schenden, zolang ze het maar niet te lang doen. Dit wordt beschreven door de Heisenbergonzekerheidsrelatie van tijd en energie, wat in dit geval betekent dat hoe korter de elektronen op het nanodeeltje zitten, hoe meer ze de wet van behoud van energie mogen schenden. Losjes gezegd mag volgens de onzekerheidsrelatie, een elektron dat van links naar rechts door het nanodeeltje wil reizen, eventjes op het nanodeeltje zitten, voordat het zich realiseert dat het de wet geschonden heeft en weer terug naar links gaat. Op diezelfde wijze mag een elektron dat zich al op het nanodeeltje bevindt en ervan af wil, een korte tijd van het nanodeeltje af 'hoppen', het nanodeeltje positief geladen achterlatend, voor het zich realiseert dat dit ook de wet schendt en schoorvoetend terugkeert. Als beide elektronen toevallig tegelijkertijd besluiten om te gaan reizen, de ene van links op het nanodeeltje, de andere naar rechts eraf, dan blijft de lading op het nanodeeltje hetzelfde, terwijl we netto één elektron van links naar rechts gebracht hebben. Stroom!

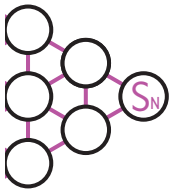

Deze manier van kwantumtransport wordt cotunnelen genoemd. Wat hier erg belangrijk is, is dat beide elektronen mee moeten doen, anders gaat het niet door. Als de kans dat één elektron meedoet (ook wel de transmissiekans of $\mathcal{T}$ genoemd) gelijk is aan de kans dat je zes gooit met een dobbelsteen, ofwel een zesde, dan is de kans dat beide elektronen meedoen gelijk aan de kans dat je twee keer zes gooit, ofwel één zesendertigste. In het geval van langere ketens van nanodeeltjes gaat elektrontransport door middel van meervoudig cotun-

[¶] In principe zijn deze twee begrippen hetzelfde. Toch is er een klein, maar belangrijk verschil. Elektronen zijn negatief geladen. Dat heeft tot gevolg dat een stroom van links naar rechts komt door elektronen die van rechts naar links reizen.

[♮] Eén Kelvin is één graad boven het absolute nulpunt, zo'n 273 graden onder nul.

nelen, waarbij vele elektronen tegelijk mee moeten doen aan het proces om een stroom te genereren. Analoog aan het vorige voorbeeld, moet je dus voor elk elektron afzonderlijk een dobbelsteen gooien, en alleen als je elke keer zes gooit, gaat er een stroom lopen. De stroom I gaat dus met de kans $\mathcal{T}$ tot een bepaalde macht N: $I \propto \mathcal{T}^N$. Dit heeft vergaande consequenties. De kans dat één elektron van het ene naar het volgende nanodeeltje 'hopt' wordt sterk bepaald door het molecuul dat zich tussen de deeltjes bevindt. Als dat molecuul een functioneel molecuul is (zoals een schakelaar), kan de kans worden beïnvloed door met licht op het netwerk te schijnen. Als de kans in dat geval bijvoorbeeld verandert van een zesde naar een half (dus gelijk aan de kans dat je bijvoorbeeld kop gooit), dan verandert de stroom niet met een factor drie, maar met 3^N. Voor een keten van vier nanodeeltjes ($N = 5$) is dit verschil een factor 243, veel groter! Je zou dus kunnen zeggen dat cotunnelen ervoor zorgt dat het netwerk gevoeliger wordt voor de moleculen die je tussen de nanodeeltjes stopt. We proberen dit experimenteel te testen in hoofdstuk zes, maar komen in hoofdstuk vijf te weten dat de huidige theorie van meervoudig cotunnelen niet afdoende is om de stroom te beschrijven.

De huidige theorie die cotunnelen beschrijft, neemt aan dat de kans dat een elektron van het ene naar het volgende nanodeeltje 'hopt' niet afhankelijk is van de energie van het elektron. Normaal gesproken is dit een prima aanname, maar afhankelijk van het molecuul tussen de nanodeeltjes, kan het zijn dat deze aanname niet meer klopt. Als de hoogste bezette moleculaire orbitaal of de laagste onbezette moleculaire orbitaal (HOMO of LUMO respectievelijk) dicht bij de Fermi-energie liggen (vergeleken met de energie die het kost om een elektron op een nanodeeltje te brengen), dan speelt de energieafhankelijkheid van de transmissiekans een rol. In hoofdstuk drie berekenen we het effect hiervan op de stroom door één enkel nanodeeltje. Dit doen we op twee manieren, de eerste in het geval dat transport door de moleculen resonant is. Dat wil zeggen dat het elektron door het molecuul heen 'stroomt', waarbij in ons geval één orbitaal of moleculair niveau alle stroom draagt. We voorspellen in dit geval dat bij hoge spanningen, de stroom groter wordt als het moleculaire niveau verder verwijderd is van de Fermi-energie van de contacten. Dit is juist tegenovergesteld aan wat we verwachten als cotunnelen geen rol speelt. Bij de tweede manier kijken we naar de situatie als transport door het molecuul niet resonant is, dat wil zeggen dat het elektron op het molecuul 'hopt', en er vervolgens aan de andere kant weer af 'hopt'. Dat betekent dus dat transport door het hele 'molecuul-nanodeeltje-molecuul'-systeem gaat door middel van meervoudig cotunnelen. Als de opladingsenergie van de moleculen groter is dan die van het nanodeeltje, voorspellen wij dat het gedrag van het systeem sterk versimpelt. In dit geval lijkt de transmissiekans niet meer afhankelijk van de energie van de elektronen, en reduceert onze voorspelling tot die van de huidige theorie (van Averin en Nazarov[Ch. 3, ref 16]). Dat wil zeggen dat een systeem met moleculen in dit geval niet meer te onderscheiden is van een systeem zonder.

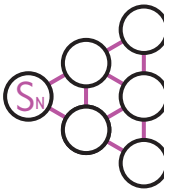

Om elektrontransport door hele netwerken van nanodeeltjes te beschrijven, moet je niet alleen rekening houden met cotunnelen, maar ook met meervoudig cotunnelen. De theorie

die meervoudig cotunnelen beschrijft, is echter een *ad hoc* uitbreiding van normaal cotunnelen. Het is dus slechts een benadering die niet altijd overeenkomt met wat er daadwerkelijk gebeurt. In hoofdstuk vijf beschrijf ik een nieuw model, afgeleid uit basisprincipes, die nauwkeurigere voorspellingen doet. Verder is dit model ook toepasbaar bij hoge spanningen (wanneer de elektrostatische energie eV groter is dan de opladingsenergie E_{C}). Dit model probeer ik te fitten aan gemeten data, maar dit lukt alleen als ik rekening houd met wanorde in het netwerk. Door aan te nemen dat de opladingsenergie voor elk nanodeeltje een beetje anders is, lukt het om het model aan de data te fitten. Belangrijker nog, het model voorspelt dat (meervoudig) cotunnelen eigenlijk helemaal geen merkbare bijdrage levert aan de stroom door het netwerk. Elektrontransport bestaat bijna volledig uit hoog-energetische elektronen die geen gebruik hoeven te maken van cotunnelen. Bij lage spanningen en temperaturen zorgen enkele percolerende paden door het netwerk voor de stroom. Bij hogere spanning en is het mogelijk voor meer paden om een bijdrage te leveren aan de stroom, en bij een nog hogere spanning kunnen alle mogelijke paden bijdragen. Dit is een erg belangrijke conclusie, aangezien hij volledig tegen de huidige consensus in gaat.

Deze conclusie heeft ook gevolgen voor de voorspelling die we een paar alinea's hiervoor deden, namelijk dat netwerken van nanodeeltjes gevoelig zijn voor de moleculen tussen de deeltjes. Aangezien cotunnelen geen significante bijdrage levert aan de stroom, is het natuurlijk maar de vraag of dit nog zo is. In hoofdstuk zes gebruik ik mijn nieuwe theorie om hier een voorspelling over te doen. Het veranderen van het molecuul tussen de nanodeeltjes verandert niet alleen de transmissiekans, maar ook de permittiviteit van het netwerk, en daarmee de opladingsenergie. Ik voorspel dat een kleine verandering in de opladingsenergie al grote gevolgen kan hebben voor de stroom door het netwerk, waarmee het netwerk nog steeds de eigenschappen van het molecuul kan versterken (zie Fig. 6.1). Om dit experimenteel te testen, gebruiken we een moleculaire schakelaar als brug tussen de nanodeeltjes en proberen deze te schakelen terwijl we de stroom door het netwerk meten. Hoewel het molecuul wel schakelt in oplossing, blijkt het niet mogelijk om te schakelen als het zich in het netwerk bevindt. Daarmee kunnen we helaas geen doorslaggevende conclusie trekken dat we netwerken kunnen gebruiken om de eigenschappen van de moleculaire bruggen te versterken.

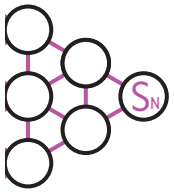

In het laatste hoofdstuk kijken we op een andere manier naar hoe elektronen door een nanodeeltjesnetwerk stromen. We gebruiken een lage-energie-elektronenmicroscoop of LEEM om op de sub-micrometerschaal te bepalen hoe de spanning over een netwerk valt. In de LEEM schieten we elektronen af op een netwerk, en remmen die vlak voor het netwerk af tot bijna stilstand. Door een extra spanning over het netwerk te zetten, worden de afgeschoten elektronen plaatselijk aangetrokken of afgestoten, afhankelijk van de spanning die daar staat. Als het elektron wordt afgestoten, komt het in de microscoop op de detector terecht, waardoor we een signaal krijgen. Als het juist wordt aangetrokken, dan komt het in contact met het netwerk, en wordt wellicht verstrooid, waardoor we het juist niet op de detector zien, en geen signaal krijgen. Door de elektronen harder en zachter op het netwerk

af te schieten, en te kijken bij welke energie ze precies worden geabsorbeerd, kunnen we achterhalen wat de plaatselijke spanning precies is. Dit zorgt niet alleen voor de mooie plaatjes die in hoofdstuk zeven te bewonderen zijn, het geeft ons ook informatie over de elektronische structuur in het netwerk. We zien bijvoorbeeld dat elektronen veel moeite hebben om langs grote gaten in het netwerk te komen, maar dat ze eigenlijk geen last hebben van kleinere gaten en imperfecties. Ook zien we dat de elektronen geen moeite hebben om vanuit de elektroden in het netwerk te komen.

Dit proefschrift beschrijft fundamenteel onderzoek naar elektrontransport door netwerken van nanodeeltjes. Het belangrijkste resultaat van dit onderzoek is dat dit transport beschreven kan worden als transport van de eerste orde, dat wil zeggen, zonder cotunnelen. Wanorde is hierbij de dominante factor. Ondanks de afwezigheid van (meervoudig) cotunnelen, voorspelt mijn model dat het alsnog mogelijk is om de effectiviteit van moleculaire schakelaars te versterken.

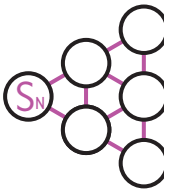

Dankwoord

Het onderzoek beschreven in dit proefschrift is een combinatie van bewust afwijken van het onderzoeksplan, en achteraf onbewust toch een antwoord geven op de originele onderzoeksvraag. Promoveren is een traject van hoge pieken en diepe dalen, dat ik niet had kunnen afleggen zonder de uitstekende intellectuele, wetenschappelijke en emotionele begeleiding van Sense Jan van der Molen. Ik wil hem graag ten zeerste bedanken voor de vrijheid die hij mij gaf om mijn eigen modellen te bedenken, maar ook voor het beperken van die vrijheid als mijn enthousiasme leidde tot tunnelvisie.

Experimenteel wetenschappelijk onderzoek is onmogelijk zonder technische ondersteuning. Hiervoor wil ik graag de volgende mensen bedanken: Ruud van Egmond voor de hulp met de installatie van de cryostaat en de opstelling eromheen, Bert Crama voor het bedraden en onderhouden van mijn insert en bijbehorende elektronica, Peter van Veldhuizen voor het ontwerpen van mijn chipcarrier en het regelen van de meetcomputers, Marcel Hesselberth voor de hulp met de lithograaf en de electronenmicroscoop. Ook wil ik de andere technici in onze vakgroepen bedanken: Douwe Scholma, Daan Boltje, Thomas Mechielsen en Funicolare Galli. Ik kon voor kleine vragen of klussen altijd terecht bij iedereen van het FMD en ELD, bedankt daarvoor! Verder wil ik Ellie van Rijsewijk-Salman en Charlotte Laurense-Griffioen bedanken voor de hulp bij het navigeren door de universitaire bureaucratie.

Ook wil ik graag Aisling Byrne en Tia Keyes in Dublin bedanken voor de Ramanmetingen die nodig waren voor hoofdstuk zes. De discussies met Dmitri Golubev zijn onmisbaar geweest bij het opstellen van mijn nieuwe model.

Tijdens mijn onderzoek heb ik ondersteuning gekregen van vijf studenten. Luigi Maduro, Remco Overdevest, Isabelle Jansen, Luka Vitomir en Yuri Bonanno: heel erg bedankt voor jullie bijdragen aan mijn onderzoek. Ik hoop dat jullie net zoveel van mij hebben geleerd als ik van jullie.

Ik heb de laatste vier jaar enorm genoten van de motiverende sfeer in onze onderzoeksgroep. Hüseyin Atesci, Edwin Devid, Daniël Geelen, Vera Janssen, Johannes Jobst, Tobias de Jong, Jaap Kautz, Aniket Thete, Alexander van der Torren, heel erg bedankt voor de nuttige en interessante discussies. Verder wil ik ook de leden van de andere onderzoeksgroepen van LION bedanken, jullie hebben een geweldige bijdrage aan de sfeer in dit instituut geleverd.

Als laatste wil ik graag mijn ouders bedanken. Zij hebben mij altijd gesteund tijdens mijn studie en promotie, en zonder hen had ik dit traject nooit af kunnen ronden.

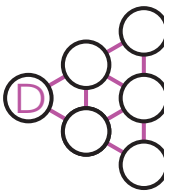

Curriculum Vitae

Sander Blok was born on the 28th of September in 1988 in Groningen. After completing his pre-university education at the Winkler Prins College in Veendam in 2007, he started studying chemistry at the Rijksuniversiteit Groningen. In 2011 he obtained his bachelor's degree with a research project on magnetism in nickel-chlorine based organic-inorganic hybrid materials. He was accepted into the Topmaster programme in Nanoscience at the same university. During his master's studies, he followed additional courses on (amongst others) cosmology and subatomic physics. He also spent time on extracurricular activities, such as organizing a study trip to Scotland with his study association; T.F.V. 'Professor Francken'. He got his degree in 2013, with a research project on pure spin injection in graphene from yttrium iron garnet.

After obtaining his degree, Sander was offered a PhD position at Leiden University, which he accepted and started in October of 2013. Under supervision of dr.ir. Sense Jan van der Molen at LION, he studied electron transport through networks of nanoparticles from an experimental perspective. During his first year, he expended his scopes and coined the idea of cotunneling with energy-dependent contact transmission, about which he published a theoretical article with a master's student and collaborators from the Technische Universiteit Delft. This paper laid the foundation for the development of a new theory, describing electron transport through networks of nanoparticles, explicitly including disorder and cotunneling. Combined with his experimental research, he concluded that higher order contributions to transport through nanoparticle networks is negligible. During his PhD, he supervised five students during their projects and also taught the LabVIEW programming course, for which he was awarded the title of teaching assistant of the year in 2017.

After his PhD, Sander will apply his knowledge on more technical problems as a first line support engineer at ASML.